Electronic Transport as Probe for the Ground State Properties in Heavy Fermion Materials and Heterostructures

Von der Fakultät für Physik und Geowissenschaften
der Technischen Universität Carolo–Wilhelmina
zu Braunschweig

zur Erlangung des Grades eines
Doktors der Naturwissenschaften
(Dr. rer. nat.)

genehmigte

Dissertation

von

Anna Otop

aus Wrocław (Polen)

1. Referent: Jun.–Prof. Dr. S. Süllow
2. Referent: Prof. J. Aarts

Eingereicht am: 17 November 2005

Mündliche Prüfung (Disputation) am: 7 März 2006

2006

VORVERÖFFENTLICHUNGEN DER DISSERTATION

Teilergebnisse aus dieser Arbeit wurden mit Genehmigung der Fakultät für Physik und Geowissenschaften, vertreten durch den Mentor der Arbeit, in folgenden Beiträgen vorab veröffentlicht:

PUBLIKATIONEN:

- A. Otop, S. Süllow, M.B.S. Hesselberth, and J. Aarts, *Proximity effects in $CeCu_6$/Nb bilayers*, Acta. Phys. Pol. B **34**, 1169 (2003).
- A. Otop, G.R. Boogaard, R.W.A. Hendrikx, M.B.S. Hesselberth, C. Ciuhu, A. Lodder, and J. Aarts, *Proximity effects in the superconductor/ heavy-fermion bilayer system Nb/$CeCu_6$*, Europhys. Lett. **64**, 91 (2003).
- A. Otop, F.J. Litterst, R.W.A. Hendrikx, J.A. Mydosh, and S. Süllow, *Magnetic irreversibility in single crystalline UPt_2Si_2*, J. Appl. Phys. **95**, 6702 (2004).
- A. Otop, F.J. Litterst, J.A. Mydosh, and S. Süllow, *Magnetoresistance of UCu_4Pd*, Physica B **359-361**, 1033 (2005).
- A. Otop, M.B. Maple, A. Weber, E.W. Scheidt, T.J. Gortenmulder, J.A. Mydosh, and S. Süllow, *Transport properties of moderately disordered UCu_4Pd*, Phys. Rev. B **72**, 024457 (2005).
- A. Otop, H.-H. Klauss, A. Bosse, R.W.A. Hendrikx, J.A. Mydosh, and S. Süllow, *Magnetic order studied via μSR in moderately disordered single crystalline UPt_2Si_2*, Physica B, in print (2006).
- S. Süllow, A. Otop, J. Klenke, R. Feyerherm, R.W.A. Hendrikx, and J.A. Mydosh, *Magnetic irreversibility in the antiferromagnetic state of UPt_2Si_2*, J. Appl. Phys., in print (2006).

TAGUNGSBEITRÄGE:

- A. Otop, S. Süllow, M.B.S. Hesselberth, and J. Aarts, *Proximity effects in* $CeCu_6/Nb$ *bilayers* (poster), International Conference on Strongly Correlated Electron Systems (SCES 2002), Krakow, Poland, July 10-13, 2002.
- A. Otop, S. Süllow, M.B.S. Hesselberth, R.W.A. Hendrikx, C. Ciuhu, A. Lodder, and J. Aarts, *Proximity Effect in* $CeCu_6/Nb$ *Bilayers* (talk), DPG-Frühjahrstagung 2003, Dresden, Germany, March 24-28, 2003.
- A. Otop, F.J. Litterst, T.J. Grotenmulder, J.A. Mydosh, R. Chau, M.B. Maple, A. Weber, E.-W. Scheidt, and S. Süllow, *Magnetoresistance of* UCu_4Pd (poster), International Conference on Strongly Correlated Electron Systems (SCES 2004), Karlsruhe, Germany, July 26-30, 2004.
- A. Otop, S. Süllow, R.W.A. Hendrikx, G.J. Nieuwenhuys, and J.A. Mydosh, *Electronic transport properties of single crystalline* UPt_2Si_2 (talk), DPG-Frühjahrstagung 2005, Berlin, Germany, March 4-5, 2005.
- A. Otop, H.-H. Klauss, A. Bosse, R.W.A. Hendrikx, J.A. Mydosh, and S. Süllow, *Magnetic order in moderately disordered single crystalline* UPt_2Si_2 (poster), International Conference on Strongly Correlated Electron Systems (SCES 2005), Wien, Austria, July 26-30, 2005.

Contents

Chapter 1

Introduction

Within the classical Sommerfeld picture, which is valid for many metallic systems, the Coulomb interactions between the electrons can be ignored, and the physical properties of such materials are well described under the assumption that the conduction electrons move freely and independently. However, for many new materials relevant to nowadays solid state physics research this classical picture is not applicable. Here, the interactions between the electrons are very strong and the correlations between these particles have to be considered. This strongly correlated behavior is very well exemplified in heavy fermion compounds [1–3], which show a wide range of "collective" and exotic phenomena such as:

- novel, unconventional superconductivity, e.g. UPt_3 [4],
- "hidden order", as observed for URu_2Si_2 [5],
- quantum phase transitions and non-Fermi liquid behavior (NFL) for example $CeCu_{5.9}Au_{0.1}$ [6–10].

These strongly correlated systems represent one of the major topics in the modern solid state physics, however a full understanding of these phenomena is lacking.

One of the main open issues is the interplay between crystallographic disorder and strong correlations. Notably, strong electronic correlations can enhance disorder effects [11]. This issue has been discussed in particular in context of non-Fermi liquid compounds. These *d*- or *f*- electron systems close to a magnetic instability display departures from the well established Fermi liquid behavior at low temperatures in their transport and thermodynamic properties. In several cases, crystallographic disorder seems to play not only a subsidiary role, but appears rather to generate the NFL behavior. Recently, in connection with this aspect much attention has been paid to the novel phase diagram for disordered systems close to a quantum critical point QCP [12]. For itinerant heavy fermions an absence of the "conventional" quantum phase transition has been postulated. Instead, for certain disorder configurations, a cluster glass phase is expected to occur.

Furthermore, the interpretation of the electronic transport properties in "moderately" disordered heavy fermion compounds appears to be problematic. For example, in case of the non-Fermi liquid system UCu_4Pd has been shown that the electrical resistivity is very sensitive to the annealing treatment of the sample, which changes the crystallographic disorder level in this compound [13]. In contrast, similar drastic changes have not been observed in the thermodynamic quantities like the specific heat or the magnetic susceptibility. Therefore, the question arises, if the departure of the electrical resistivity from a Fermi liquid scenario at low temperatures can be taken as a indication for a NFL state.

The reason that in the first place the resistivity of UCu_4Pd is considered as NFL hallmark reflects the common assumption made for heavy fermion, that the resistivity ρ probes the magnetic ground state. A recent study on moderately disordered URh_2Ge_2 [14], however, indicates that the electronic transport properties for this single crystalline sample should rather be described in terms of disorder induced localization effects. For this material the Hall effect and optical conductivity measurements confirm the metallic ground state. The electrical resistivity, however, is large (a few hundred $\mu\Omega$cm) and exhibits a negative temperature coefficient, $d\rho\ /\ dT < 0$. A representation of these data in terms of a reduced conductivity revealed a close similarity to the behavior of 3D amorphous metals. In analogy, the question arises if similar physical processes need to be considered in UCu_4Pd.

The disorder level of all these compounds is of the order of 10%, that is a breaking of translational invariance occurs for about every 10 unit cells. This type of crystallographic disorder is very hard to determine in crystallographic studies and is likely to go unnoticed. Therefore, there are only very few systems, for which moderate disorder has been established, with the consequence that this topic is neither well–studied nor well understood. Hence, a model system is required. Preferably, it has to be available as large single crystal to allow for a detailed, high-resolution study of the crystallographic structure (for example by neutron scattering). There should also be a bright elemental contrast in structural studies to detect moderate disorder levels. Furthermore, for single crystalline samples, the observed physical properties can certainly be considered to be intrinsic. Until now such a model system has been missing. Here, we propose a study of single crystalline (as grown and heat treated) UPt_2Si_2 as a material that fulfills all these requirements, and present the related investigations. As theoretical concepts describing the influence of moderate disorder on the physical properties of heavy fermions are incomplete this investigation attempts to provide a data basis for further theoretical work.

The study of unconventional superconductivity in heavy fermion systems attracted great interest over last two decades. The exotic pair mechanism (e.g. spin fluctuations) and the symmetry of the order parameter have been intensively discussed especially for superconducting Ce- or U-based compounds, e.g. UPt_3 [4], $CeCoIn_5$ [15] or $CePt_3Si$ [16, 17]. In connection with this topic the question about the ability of the heavy fermion ground state to sustain superconductivity appears to be particulary intriguing. The superconducting correlations can be induced into heavy fermions through proximity effect in superconductor/heavy fermion structures and provide important new insights into pair breaking mechanism in heavy fermions.

In superconductor/non superconducting material (S/N) multilayers structures, below T_c the Cooper pairs can diffuse over the interface into the N system via the proximity effect [18]. Then in the non–superconducting layers the Cooper pairs lose their coherence over a characteristic distance, which depends on the pair breaking mechanism in this material. Until now, mainly two classes of N-system have been investigated, *viz.*, metals and ferromagnets [19, 20]. Here we present a study on superconductor/heavy fermion metal layers. In this first investigation of the proximity effect in such a system we analyze the data on basis of the Takahashi–Tachiki model [21].

The outline of this thesis will be as follows: In **Chapter 2** we present a brief phenomenological review of heavy fermion physics and the NFL scenario. Further, a new phase diagram is proposed based on experimentally insights, in which we introduce a new and independent control parameter, *i.e.*, the level of disorder. As much emphasis in this work is laid upon the electronic transport properties, we introduce the basic concepts and discuss the influence of disorder. Further, the proximity effect is briefly described. The theoretical model applied to account for superconductor/metal systems is presented, which with some modification will be used for the present superconductor/heavy fermion case.

Chapter 3 is dedicated to UCu_4Pd. We review previous research results, especially with respect to crystallographic structure studies. For as–cast and differently heat treated samples, we establish the magnetic properties by means of a magnetic susceptibility study. We discuss the temperature scaling of the susceptibility with the different models commonly taken as NFL indicators. The transport properties electrical resistivity, Hall effect and magnetoresistivity are presented. We will show that the electrical resistivity is strongly sample dependent and drastically changes upon annealing, which is connected to changes of the actual disorder level in the material. The temperature dependence of the Hall constant is best described by the side jump scenario. Further, from Hall constant analysis, a metallic carrier density is derived. The magnetoresistivity is small suggesting that the resistivity is controlled mostly by nonmagnetic scattering. We discuss possible sources of the temperature and field dependence for the transport properties, in particular with respect to quantum criticality and electronic localization effects.

In **Chapter 4** we present the moderately mass enhanced system UPt_2Si_2. For an as-cast single crystal, random ion displacement on certain nonmagnetic (Pt/Si) sites from high symmetry positions has been found in neutron diffraction at low temperatures as source of the crystallographic disorder. We find that this moderate disorder considerably influences the thermodynamic properties of the system, such as the specific heat or magnetic susceptibility. The behavior observed in these experiments can be explained in a picture of antiferromagnetic clusters forming above an antiferromagnetic phase transition temperature, and which act as condensation cores for AFM domains upon lowering the temperature below T_N. This concept is supported by the results of magnetic structure measurements carried out by neutron diffraction and zero–field time–differential muon spin relaxation measurements. In connection with these results we discuss in detail the electronic transport properties electrical resistivity, magnetoresistivity and the temperature dependence of the Hall constant.

We present the results of annealed UPt_2Si_2 in **Chapter 5**. Although the structural study reveals only minor changes of the crystallographic disorder level, the annealed samples show considerable differences in the magnetic susceptibility and the transport properties. It highlights the effect that strongly correlated systems are very sensitive to even a small deviation of the crystallographic structure from the perfect lattice.

In **Chapter 6** we discuss the proximity effect between the superconductor Nb and the heavy fermion system system $CeCu_6$. We investigate the dependence of the critical temperature and the upper critical field on varying the Nb film thickness *via.* electronic transport measurements. The preparation of high quality thin film structures is a crucial point in this study. Therefore, we discuss in detail the preparation conditions and the characterization of the samples with respect to their stoichiometry and topography. We propose an analysis of the upper critical field and critical temperature data based on the Takahashi–Tachiki theory.

Bibliography

[1] P. Fulde, *Electron Correlations in Molecules and Solids*, Springer Ser. Solid-State Sci., Vol. 100 (Springer, Berlin, Heidelberg 1995) p. 349.

[2] N. Grewe and F. Steglich, in *Handbook of the Physics and Chemistry of the the Rare Earths*, *Vol. 14* edited by K.A. Gschneidner Jr., and L. Eyring, (Elsevier, Amsterdam 1991), p. 343.

[3] Z. Fisk, D.W. Hess, C.J. Pethick, D. Pines, J.L. Smith, J.D. Thompson, and J.O. Wills, Science **239**, 33 (1988).

[4] R. Joynt, and L. Taillefer, Rev. Mod. Phys. **74**, 235 (2002).

[5] P. Chandra, P. Coleman, J.A. Mydosh, and V. Tripathi, Nature **417**, 831 (2002).

[6] Q. Si, S. Rabello, K. Ingersent, and J.L. Smith, Nature **413**, 804 (2001).

[7] P. Coleman, C. Pepin, Q. Si, and R. Ramazashvili, J.Phys.: Condens. Matter **13**, R723 (2001).

[8] E. Miranda, V. Dobrosavljevic, and G. Kotliar, J.Phys.: Condens. Matter **8**, 9871 (1996).

[9] G.R. Stewart, Rev. Mod. Phys. **73**, 797 (2001).

[10] H. v. Löhneysen, J. Phys. Condens. Matter **8**, 9689 (1986).

[11] K.I. Wysokinski, Phys. Rev. B **60**, 16376 (1999).

[12] V. Dobrosavljevic, and E. Miranda, Phys. Rev. Lett. **94**, 187203 (2005).

[13] A. Weber, S. Körner, E.-W. Scheidt, S. Kehrein, and G.R. Stewart, Phys. Rev. B **63**, 205116 (2001).

[14] S. Süllow, I. Maksimov, A. Otop, F.J. Litterst, A. Perucchi, L. Degiorgi, and J.A. Mydosh, Phys. Rev. Lett. **93**, 266602 (2004).

[15] K. Izawa, H. Yamaguchi, Y. Matsuda, H. Shishido, R. Settai, and Y. Onuki, Phys. Rev. Lett. **87**, 057002 (2001).

[16] E. Bauer, G. Hilscher, H. Michor, Ch. Paul, E.-W. Scheidt, A. Gribanov, Yu. Seropegin, H. Noël, M. Sigrist, and P. Rogl, Phys. Rev. Lett. **92**, 027003 (2004).

[17] A. Amato, E. Bauer, and C. Baines, Phys. Rev. B **71**, 092501 (2005).

[18] P.G. de Gennes, Rev. Mod. Phys. **36**, 225 (1964).

[19] V.M. Krasnov, A.E. Kovalev, V.A. Oboznov, and N.F. Pedersen, Phys. Rev. B **54**, 15448 (1996).

[20] J. Aarts, J.M.E. Geers, E. Brück, A.A. Golubov, and R. Coehoorn, Phys. Rev. B **56**, 2779 (1997).

[21] S. Takahashi, and M. Tachiki, Phys. Rev. B **33**, 4620 (1986).

CHAPTER 2

Basic ideas

This chapter gives an short introduction to basic, relevant to this thesis aspects of heavy fermion physics upon the reviews by Fulde [1], Grewe and Steglich [2], Fisk [3], Bauer [4], and Miranda and Dobrosavljevic [5]. Further, we briefly discus the theory of the proximity effect on superconductor/normal material multilayers.

2.1 Heavy Fermions

At low temperatures and below a characteristic temperature T^*, heavy fermion compounds develop a strongly correlated state with a huge effective mass m^* of the electrons. m^* may be as large as several hundred times the free electron mass, hence the label "heavy fermions". Mainly, heavy fermion materials contain rare earth constituents like lanthanides Ce, Yb or actinides e.g. U or Np. Prominent examples are: $CeCu_6$, $CeCu_2Si_2$, and $CeAl_3$ [6, 7].

Traditionally, the description of heavy fermion compounds involves the recognition that there are two qualitatively different regimes:

- at $T > T^*$, the system behaves like one with weakly interacting magnetic moments and resembles dilute Kondo systems;
- in contrast, at $T < T^*$ the so-called coherent state is formed.

The hallmarks of non-magnetically ordered heavy fermion compounds in the coherent state are:

- a free electron like temperature dependence of the specific heat c_p with $c_p = \gamma T$ and the Sommerfeld coefficient γ as large as ~ 1 J mole^{-1} K^{-2},
- a Pauli paramagnetic susceptibility χ_p, which is enhanced in a similar way as γ,

- an electrical resistivity ρ following a Fermi liquid dependence $\rho(T) = \rho_0 + AT^2$ and
- a Sommerfeld-Wilson ratio $R = \pi k_B^2 \chi_p / (3\mu_{eff}^2 \gamma)$ of the order unity (μ_{eff} = effective magnetic moment of the quasiparticles).

Since both, χ_p and γ, are proportional to the density of state at the Fermi level, the large values of these parameters are attributed to the large m^*. Therefore, the properties of the heavy fermion compounds below T^* are well described within Fermi Liquid theory, as a one-to-one correspondence can be drawn between the quasiparticles and free electrons.

Microscopically, the mass enhancement mirrors the interplay of localized f electron states, placed just below the Fermi energy and delocalized conduction electrons. This gives rise to resonant scattering of conduction electrons off the localized states, resulting in an enhancement of the density of states DOS at the Fermi level referred to as Abrikosov–Suhl–resonance. Furthermore, for heavy fermion system, the interaction between the localized states plays a very important role, as a number of systems order magnetically or become superconducting. It has been shown that the superconducting and magnetically ordered (hidden order) phases are formed within the heavy quasiparticle liquid ($CePd_2Si_2$, UPt_3, URu_2Si_2).

The ground state of f–electron systems is predicted by considering the ratio between the binding energy of an unperturbed f^n state, E_0, and the hybridization between the local f states with the delocalized conduction electrons, Γ. Three different regimes can be distinguished:

- $\Gamma \ll E_0$: The hybridization of the f levels with the conduction electrons can be neglected. The magnetic properties are given by a classical Heisenberg–like exchange and by taking into account crystal field splitting. In most cases, the ground state is long range magnetically ordered.
- $\Gamma < E_0$: The f states are still stable, with a nearly integer valence. This case is known as the Kondo regime.
- $\Gamma \geq E_0$: Strong mixing of local and delocalized states occurs. The f states are unstable, and in consequence the ground state of the system is nonmagnetic (mixed valent systems).

Heavy fermion behavior is observed for $\Gamma < E_0$, where Kondo centers are placed on a regular lattice. In such a Kondo lattice the scattering can become coherent at low temperatures ($T < T^*$), and the physical properties are described by Fermi liquid theory.

On the other hand, at low temperatures, the Rudermann-Kittel-Kasuya-Yosida (RKKY) interaction will cause antiferromagnetic exchange between the f-moments, here provided by the conduction electrons. This interaction tends to promote magnetic order. Doniach [8,9] proposed a phenomenological description based on the assumption that the magnetic ground state of heavy fermion system is the result of a competition between Kondo scattering and RKKY interactions (Fig. 2.1). The energy associated with Kondo interactions is given by

$$k_B T_K \propto \frac{1}{N(E_F)} exp(-\frac{1}{JN(E_F)}), \tag{2.1}$$

and for the RKKY exchange

$$k_B T_{RKKY} \propto J^2 N(E_F), \tag{2.2}$$

with E_F - Fermi energy, $N(E_F)$ - density of states at the Fermi level, J - hybridization between the localized and conduction electrons. Thus, in the Doniach picture the magnetic behavior of a system is controlled by the hybridization strength J and the density of states DOS at the Fermi level *N(*E_F*)*. J can be tuned by pressure, or chemical pressure through isoelectronic alloying [8, 10]. If *N(*E_F*)* is constant, in a pressure experiment we expect:

- for $T_K < T_{RKKY}$, the magnetic transition temperature T_N close to the magnetic instability to be continuously suppressed to zero as function of J, with $T_N \propto (J_c - J)^x$.
- at $T_K = T_{RKKY}$ and the characteristic hybridization strength of $J = J_c$, the magnetic phase transition is suppressed to $T = 0$. The thermodynamic properties at such a quantum critical point QCP are determined by collective modes which are driven by fluctuations of the order parameter. In consequence, non–Fermi liquid NFL behavior appears, *i.e.*, temperature dependencies of the magnetic ground state properties is not consistent with Fermi liquid theory.

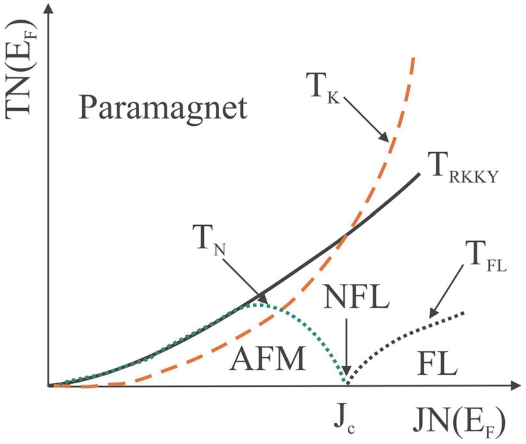

Figure 2.1: The Doniach phase diagram of the one dimensional Kondo-lattice. For the details see text [8].

- for $T_K > T_{RKKY}$ and $J > J_c$, below a characteristic temperature $T_{FL} \propto (J - J_c)^y$ Fermi liquid (FL) behavior is recovered.

The exponents x and y, in models put forth so far [11,12], depend on spatial dimensionality and type of magnetic coupling. At present, however, there is no full consensus about the adequacy of these models and the underlying physics [13].

2.1.1 Non Fermi liquid

Departures from Fermi liquid behavior are observed not only for compounds close to the quantum critical instability in a Doniach-like phase diagram (e.g. $CeCu_{5.9}Au_{0.1}$ [14]) but also for several materials which seems to be far away from a QCP (e.g. $UCu_{5-x}Pt_x$ [15]). The characteristics of these novel non–Fermi–liquid phases are a logarithmic or power-law temperature dependence of the specific heat and the magnetic susceptibility, as well as the non–quadratic electrical resistivity at low temperatures [16]. Different theoretical models have been proposed to account for NFL behavior, with the most relevant of them being:

- proximity to a second order phase transition or quantum critical point [17,18],
- the multichannel Kondo effect, where the f–electon impurity spins are overscreend by the conducting electrons [19,20],
- a disorder driven distribution of Kondo temperatures (Kondo disorder model). The Kondo scattering on each f–electron impurity site sets a different temperature scale, which leads to a broad range of effective Kondo temperatures [21],
- competition between Ruderman–Kittel–Kasuya–Yosida (RKKY) and Kondo interaction causing in a disordered system a formation of magnetic clusters in a non magnetic Fermi liquid (Griffith's phase model) [22,23].

2.1.2 Disorder effects in heavy fermion compounds

Experimentally, the relevance of disorder effects for the understanding of heavy fermion normal state properties has been investigated for various families of compounds. Here, in particular, studies have been performed on pseudo-binary systems of the 1:1, 1:2 or 1:3 [24–28] stoichiometry, or ternary heavy fermion intermetallics like those of composition 2:1:3 [29–32], the U(Cu,Pd)$_5$ system [21,33–38], or U- and Ce-122 compounds [10,39–44]. The goal of such material studies is the search for quantum critical behavior close to a magnetic instability, which might be accessed by tuning a magnetic transition temperature to zero through alloying. The presence of crystallographic disorder complicates matters as it introduces a new, independent, and often uncontrolled parameter.

Recently, the Doniach picture has been extended in order to incorporate disorder effects [45,46]. This way, with the disorder modelled assuming a distribution $P(J_{ij})$ of locally and randomly varying hybridization values J_{ij}, it is demonstrated that the disorder can give rise to spin glass phases, which compete with the other ground states of the Doniach model [8].

In experiments such as alloying studies, aside from chemical pressure effects, the distributions $P(J_{ij})$ are also varied. Therefore, through alloying, two independent control parameters are modified at the same time: (*i.*) the exerted chemical pressure gives rise to a variation of the average hybridization strength J; (*ii.*) the local level of random site exchange, and thus $P(J_{ij})$, is affected. Qualitatively, $P(J_{ij})$ can be parameterized as a distribution of local hybridization values within a range ΔJ around the average value J, *i.e.*, the local hybridization lying in the interval $J \pm \Delta J$. With this terminology, in an alloying study the magnetic ground state properties of a series of materials are a function of the two independent control parameters J and ΔJ, with J as a measure for the external pressure and ΔJ for the level of disorder.

The presence of two control parameters J and ΔJ requires an extension of the "generic magnetic phase diagram" of heavy fermions by incorporating a third dimension, crystallographic disorder, with ΔJ as parameter characterizing the disorder level. A detailed and quantitative discussion of this "three dimensional magnetic phase diagram of disordered heavy fermions" is impossible at present [45, 46], nor is it the scope of this work. A qualitative discussion, however, illustrates various important issues of heavy fermion physics. Therefore, in Fig. 2.2(a) we sketch the generic magnetic phase diagram under incorporation of the parameter disorder ΔJ.

If we consider a crystallographically perfectly ordered heavy fermion material, which orders antiferromagnetically (AFM) below a transition temperature T_N, in Fig. 2.2(a) this material would be positioned on the AFM phase transition line for a disorder level $\Delta J = 0$. By increasing the hybridization strength J, for instance by means of a pressure experiment on a Ce compound, we traverse the "generic magnetic phase diagram of ordered heavy fermions". Following Ref [12], for the three-dimensional case a suppression of the antiferromagnetic transition temperature $T_N \propto (J_C - J)^{2/3}$ is predicted. FL behavior is recovered below $T_{FL} \propto J - J_c$ (area "I"), while at the magnetic instability, for $T_N = 0$, NFL behavior occurs in the area "II".

In contrast, again with the starting point of the perfectly ordered material, if we increase the level of disorder, it will cause a suppression of the magnetic transition temperature. While there are not as detailed predictions on the disorder dependence of T_N as for the hybridization dependence, qualitatively the suppression has been demonstrated both on theoretical as experimental grounds [47, 48]. For the low moment magnets and strongly

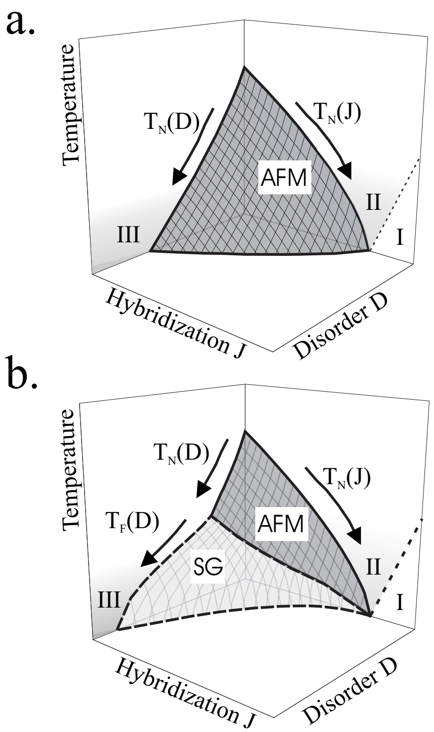

Figure 2.2: Schematic phase diagrams of heavy–fermion compounds as function of the independent control parameters hybridization J and disorder $\Delta J = D$; for details see text.

correlated electron systems considered here, because of the inherent instability of the magnetic ground state, a complete suppression of the AFM through disorder will be possible. (This is in contrast to large moment magnets and weakly correlated metals, where a complete suppression of the magnetic transition temperatures through disorder appears to be difficult; see Ref. [48]). Experimentally, this is indicated by observations on $CeAl_3$ or $CePd_2Al_3$ [49, 50], where the presence or absence of magnetic order in single or polycrystals has been linked to crystallographic disorder on the Al sites.

In consequence, sufficiently close to the magnetic instability (for sufficiently strong correlations) disorder induced suppression of AFM order will occur, leading to a situation as sketched in Fig. 2.2(a). For $T_N = 0$, NFL behavior is predicted to occur, although now extended over some range in disorder (area III) because of rare magnetic configurations [22].

Our phenomenological sketch illustrates two aspects relevant to heavy fermion materials and other strongly correlated electron materials. The first issue is about how to connect the NFL areas II and III. If there is a continuous and smooth transition from II to III, it would imply that NFL characteristics of a heavy fermion material even in the presence of weak disorder could be disorder modified, compared to the perfectly ordered case. Specifically, if an experiment is chosen on an antiferromagnetic, weakly disordered heavy fermion, which only varies the global hybridization strength J, upon suppression of T_N its J dependence might deviate from the ordered case, and NFL behavior would occur over a wider range in J even at zero temperature.

Secondly, in alloying experiments both parameters of the phase diagram in Fig. 2.2(a), hybridization J as disorder ΔJ, are modified simultaneously. Correspondingly, in a doping study starting with a crystallographically ordered, antiferromagnetic heavy fermion system and finishing at a paramagnetic, crystallographically ordered Fermi liquid, a complicated trajectory through the three-dimensional phase diagram is traversed. Then, the associated alloying phase diagram will not match an experiment varying J only.

The underlying assumption of the sketched phase diagram in Fig. 2.2(a) is that upon increasing the disorder level the principal type of magnetic order remains the same. This assumption is not always true for real materials. If disorder is associated by competing interactions, it can give rise to new magnetic states, for instance spin glass phases. Experimentally, this has been demonstrated for many systems [10, 24–26, 29–31, 34, 40, 42, 43], with theoretical support in the Refs. [45, 46].

Specifically, for URh_2Ge_2 it has been shown that by varying the level of crystallographic disorder a transition from an antiferromagnetic to a spin glass ground state can be facilitated [10]. Further, in the alloying series $U(Cu,Pd)_5$ and $(Y,U)Pd_3$ spin glass ground states are suppressed to zero temperature, and are associated by NFL characteristics [28, 34]. In consequence, if glassy states occur in a given class of compounds, for the schematic phase diagram qualitatively we expect a behavior as sketched in Fig. 2.2(b). Here, for zero disorder upon variation of J the situation is the same as for the purely antiferromagnetic case (Fig. 2.2(a)). However, if for an antiferromagnetic material the level of disorder is increased from zero, it initially will cause a suppression of T_N. Beyond a material specific disorder level a transition into a spin glass ground state below the freezing temperature T_f will occur. Increasing the disorder level further causes a suppression of T_f, and the subsequent occurrence of NFL behavior adjacent to the spin glass phase.

In addition to the issues discussed for the purely antiferromagnetic case in Fig. 2.2(a), with the presence of the spin glass phase additional topics emerge. In particular, it is an open question how spin glass and antiferromagnetic phase compete close to the magnetic instability on the zero-disorder axis. The scenario sketched in Fig. 2.2(b), with the spin glass phase reaching out to zero disorder, is based on the hypothesis that for an arbitrarily weak magnet an arbitrarily small level of disorder should be sufficient to destroy the AFM state.

For real materials, the situations encountered experimentally might be far more complicated than those that can be derived from the sketches in Fig. 2.2. We have not considered features like Fermi surface nesting or hidden order phenomena [51–53], nor disorder induced effects like AFM states with anomalously short correlations lengths [32, 54]. Still, from our sketches the relevance of disorder effects for the understanding and interpretation of experimental data is evident.

2.1.3 Transport phenomena

For the heavy fermion systems, usually it is assumed that the magnetic ground state is probed not only in thermodynamic but also in the transport properties. However, as has been shown in a recent study on URh_2Ge_2 [39], for such moderately disordered compounds, we have to consider disorder induced localization effects. The basic idea is that especially the electrical resistivity in a strongly correlated compound is very sensitive to even a small level of lattice disorder.

In case of a perfectly ordered material, the total relaxation time of the electrons participating in the electrical current is a sum over relaxation times associated to different scattering processes, assuming that they are independent from each other (Matthiessen's rule)

$$\frac{1}{\tau} = \sum \frac{1}{\tau_i}. \tag{2.3}$$

Then, the electrical resistivity is given as

$$\rho = \sum \rho_i = \rho_0 + \rho_{ph} + \rho_{mag}, \tag{2.4}$$

where ρ_0 results from temperature independent scattering on nonmagnetic impurities, ρ_{ph}–scattering from phonons, and ρ_{mag} is a measure for magnetic scattering contributions.

For heavy fermions, usually the magnetic scattering dominates the electronic transport properties. An adequate description of ρ_{mag} has to take into account the Kondo scattering of the conducting electrons with the localized f electron, correlation effects at low temperatures and the crystal field potential. Several approaches have been made to describe ρ_{mag}, which however often are restricted to limited temperature ranges. The Kondo model (s-f model), for example, is used to account for the transport properties at $T > T_K$. According to the calculations within this model ρ_{mag} is given by

$$\rho_m = \rho_c \left(1 + \frac{ln(T/T_K)}{[ln^2(T_K/T) + \pi^2 S(S+1)]} \right), \tag{2.5}$$

with $\rho_c = mc/ne^2\pi N(E_F)$, c the impurity concentration, T_K – Kondo temperature, S – total spin.

For low temperatures ($T < T^*$) and metallic heavy fermions, a Fermi liquid behavior is observed, with $\rho_{mag} = AT^2$, as a result of a coherent Bloch wave states. The coefficient A reflects the heavy mass of the quasiparticles. $\rho(T)$ for the onset of coherence has been described in different approaches by solving Anderson Hamiltonian (Kondo lattice model) [55–57].

In the traditional picture of metallic electrical resistivity, the Bloch waves lose the phase coherence by scattering on a random potential over the length scale comparable with the mean free path l. The wave function, however, remains extended throughout the sample. However, as Anderson pointed out in his initial calculations [58], for a sufficiently strongly randomized potential the electronic wave functions will be profoundly affected and can become localized [58–60]. The envelope of such a wave function decays exponentially from some point in space,

$$|\psi(\overline{r})| \sim exp\left(\frac{|\overline{r}-\overline{r}_0|}{\xi}\right), \tag{2.6}$$

where ξ is the localization length. In case of very strong disorder, the eigenstate would be a bound state by deep fluctuation of the random potential. The combination of such localized states will not lead to an extended state, as they are in general very different in energy. Anderson has labelled a degenerate electron gas with localization in such a random field a "Fermi glass".

At very low temperatures (for $T \rightarrowtail 0$), the conductivity of such a localized system approaches zero. If the temperature increases the conductivity rises due to thermal activation. The most elemental models yield conductivities with exponential temperature dependence:

$$\sigma = \sigma_0 exp\left(-\frac{E_c - E_F}{k_B T}\right) \tag{2.7}$$

E_c – characteristic for the system mobility edge energy, E_F – Fermi energy, σ_0 is proportional to the product of diffusion constant and relaxation time.

More advanced models take into account additional processes like e.g. thermally activated hopping etc. Essential to this localization approach is the non-validity of the Matthiessen's rule. Instead of considering electronic transport along the series of resistors ρ_0, ρ_{ph} and ρ_{mag}, now the conductivity through different non-interacting channels is decisive. This alternative view of electronic transport is expressed in the Kawabato–formula [59]

$$\sigma = \sigma_B exp\left(1 - \frac{C}{(lk_B)^2}(1-\frac{l}{L_i})\right) \tag{2.8}$$

σ_B is the Boltzmann conductivity, l – mean free path, C – constant, the inelastic diffusion length L_i corresponds to processes (electron–electron or electron–phonon) responsible for delocalization out of the local random potential. If in addition electronic correlations and spin orbit coupling is taken into account, the T dependence of the conductivity is predicted [62, 63] to behave as

$$\Delta\sigma(T) = \frac{e^2}{2\pi^2\hbar}\left(3\sqrt{b+c^2T^2} - cT - 3\sqrt{b} + d\sqrt{T}\right), \tag{2.9}$$

with $b = 1/D\tau_{so}$, $c = \sqrt{1/4D\beta}$, $\beta = \tau_i T^2$, $d = 0.7367\sqrt{k/D\hbar}$ (diffusion coefficient D, spin-orbit τ_{so} and inelastic τ_i scattering times).

It should be emphasized that the latter view of electronic transport in the localized limit treats the electrons as particles diffusing through the material, in contrast to the ballistic behavior in the metallic state. This difference in the character, diffusive *vs.* ballistic transport, will be central issue to be discussed for the moderately disordered heavy fermion compounds investigated here.

2.2 Proximity effect

The proximity effect describes the spatial modulation of the Cooper pair density at the interface between a superconductor and a non–superconducting system (S/N), for example a metal. Evidently, the density of Cooper pairs in the superconductor is reduced in the immediate vicinity of the non-superconducting system. Conversely, a non-zero Cooper pair density appears in the normal system close to the interface that is, the superconductivity "leaks" into this material (Fig. 2.3) [64]. The Cooper pairs, or rather the electrons deriving from a Cooper pair, diffuse into the normal material and can maintain their coherence over distances up to a few hundred nanometer. Further, since some of the electrons will be scattered at the S/N boundary, it leads to a discontinuity of the Cooper pair density at the interface.

The spatial variation of the Cooper pair density on the S/N interface is, for homogeneous superconductors in the dirty limit (*i.e.* if electron motion has diffusive character), dependent on

- the electron diffusion constants D_S and D_N for the S and N systems respectively,
- the transparency of the interface for electrons and Cooper pairs,

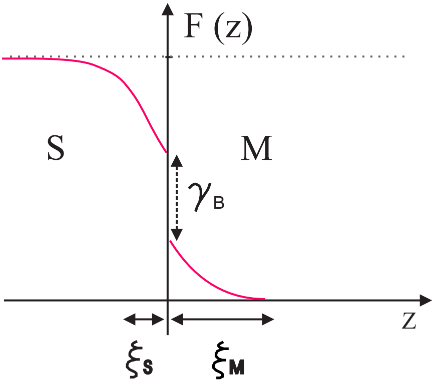

Figure 2.3: A schematic representation of the Cooper pair density F(z) at the superconductor (S) / metal (M) boundary; ξ_S: coherence length in the superconductor, ξ_M: coherence length in the normal metal, γ_B: interface transparency parameter, for details see text.

- the pair breaking mechanisms in the non–superconducting system.

Let us first consider the case when the non-superconductor is a metallic material like Cu or Au. The Cooper pairs in this system are destroyed by thermal fluctuations. Then, the superconducting correlation length in the normal metal is given by:

$$\xi_M = \sqrt{(\hbar D_N)/(2\pi k_B T)}, \tag{2.10}$$

yielding large values at low temperatures.

If the non–superconducting material is a ferromagnet, the pair breaking is caused by the exchange interaction E_{ex}, which is proportional to the magnetic moment of the host ion. The temperature independent part of the coherence length follows to:

$$\xi_F = \sqrt{(\hbar D_F)/(2\pi E_{ex})} \tag{2.11}$$

When $E_{ex} \gg k_B T$, the penetration depth of the Cooper pairs into the ferromagnet is very small (a few nanometers). The presence of Cooper pairs in the N system can be detected in the thermodynamic properties of

S/N multilayers such as the critical temperature T_c or the upper critical field H_{c2}. In order to quantitatively analyze the proximity effect of dirty superconductor/non–superconductor multilayers, Ciuhu and Lodder proposed model calculations based on the Takahashi–Tachiki theory [65, 66], which successfully takes into account the interface transparency [67,68]. In a strict sense, they rather used a boundary resistance parameter R_B instead of an interface transparency parameter γ_B, which is related to the former through the resistivity ρ_N and the coherence length ξ_N of the normal layer:

$$\gamma_B = \frac{R_B}{\rho_N \xi_N} \tag{2.12}$$

In effect, it simplifies matters, as it allows to carry out calculations by considering only three independent parameters D_S, D_N and R_B. With this formalism the Gor'kov equations for the pair potential $\Delta(\mathbf{r})$ are solved, with the space dependent coupling V($\mathbf{r}$):

$$\Delta(\mathbf{r}) = V(\mathbf{r}) kT \Sigma_\omega \int d^3\mathbf{r}' Q(\mathbf{r}, \mathbf{r}\text{'}) \Delta(\mathbf{r}\text{'}) \tag{2.13}$$

with ω the so–called Matsubara frequencies. In the dirty limit, Takahashi and Tachiki have shown that Q_ω obeys the equation (in the Green's function formalism):

$$[2|\omega| - \hbar D(\mathbf{r})(\nabla - \frac{2ie}{\hbar c}\mathbf{A}(\mathbf{r}))^2] Q(\mathbf{r}, \mathbf{r}\text{'}) = 2\pi N(\mathbf{r}) \delta(\mathbf{r} - \mathbf{r}\text{'}) \tag{2.14}$$

$\mathbf{A}(\mathbf{r})$ is the vector potential of an externally applied magnetic field, $\mathbf{H} = \nabla \times \mathbf{A(r)}$. $V(\mathbf{r})$, $N(\mathbf{r})$ and $D(\mathbf{r})$ represent the BCS coupling constant, the electronic density of states at the Fermi energy, and the diffusion coefficient, respectively. These parameters are assumed to be constant for each layer of the S/N multilayer. At the interface, the boundary conditions are [69, 70]:

$$D(\mathbf{r}) \frac{\partial}{\partial \mathbf{z}} F(\mathbf{r})|_{\mathbf{r}=r^+} = D(\mathbf{r}) \frac{\partial}{\partial \mathbf{z}} F(\mathbf{r})|_{\mathbf{r}=r^-} = \frac{1}{e^2 R_B} (\frac{F(\mathbf{r}^+)}{N(\mathbf{r})} - \frac{F(\mathbf{r}^-)}{N(\mathbf{r}^-)}) \tag{2.15}$$

The pair amplitude F($\mathbf{r}$) is defined by $\Delta(\mathbf{r}) = V(\mathbf{r})F(\mathbf{r})$. The boundary resistance R_B characterizes the barrier the electrons experience at the interface. In other words, R_B represents the reduction of the Cooper pair migration into the non–superconducting system due to a mismatch of the

Fermi levels, lattice structure and lattice constant of the materials at the interface. This, in consequence, reduces the leakage of Cooper pairs in the N–layer. The differences in the coherence length of the superconducting correlations induced in a normal metal or a ferromagnet serve to show what kind of information we want to extract from the heavy fermion system by a proximity effect experiment. A priory it is not known what can be expected for the coherence length or for the boundary resistances, *c.q.* how these quantities are determined by the properties of the HF system. This will be addressed in Chapter 6, where measurements on a superconducting / heavy fermion system are presented. The above formalism will then be used for a quantitative discussion of the proximity effect in a superconductor / heavy fermion system which is presented in Chapter 6. A full discussion of the model is given in Ref. [67, 68].

Bibliography

[1] P. Fulde, *Electron Correlations in Molecules and Solids*, Springer Ser. Solid-State Sci., Vol. 100 (Springer, Berlin, Heidelberg 1995) p. 349.

[2] N. Grewe, and F. Steglich, in *Handbook on the Physics and Chemistry of the Rare Earths, Vol. 14* edited by K.A. Gschneidner Jr., and L. Eyring, (Elsevier, Amsterdam 1991), p. 343.

[3] Z. Fisk, D.W. Hess, C.J. Pethick, D. Pines, J.L. Smith, J.D. Thompson, and J.O. Wills, Science **239**, 33 (1988).

[4] E. Bauer, Adv. Phys., **40**, 417 (1991).

[5] E. Miranda, and V. Dobrosavljevic, Rep. Prog. Phys. **68**, 2337 (2005).

[6] G.R. Stewart, Z. Fisk, and M.S. Wire, Phys. Rev. B **30**, 482 (1984).

[7] A. Amato, D. Jaccard, J. Flouquet, F. Lapierre, J.L. Tholence, R.A. Fisher, S.E. Lacy, J.A. Olsen, and N.E. Phillips, J. Low. Temp. Phys. **68**, 371 (1987).

[8] S. Doniach, in *Valence Instabilities and Related Narrow Band Phenomena*, edited by R.D. Parks (Plenum, New York, 1993), p. 435.

[9] S. Doniach, Physica B **91**, 231 (1977).

[10] S. Süllow, G.J. Nieuwenhuys, A.A. Menovsky, J.A. Mydosh, S.A.M. Mentink, T.E. Mason, and W.J.L. Buyers, Phys. Rev. Lett. **78**, 354 (1997).

[11] J.A. Hertz, Phys. Rev. B **14**, 1165 (1976).

[12] A.J. Millis, Phys. Rev. B **48**, 7183 (1993).

[13] Q. Si, S. Rabello, K. Ingersent, and J.L. Smith, Nature **413**, 804 (2001).

[14] H. v. Löhneysen, J. Phys. Condens. Matter **8**, 9689 (1986).

[15] R. Chau, and M.B. Maple, J. Phys.: Condens. Matter **8**, 9939 (1996).

[16] G. Stewart, Rev. Mod. Phys. **73**, 797 (2001).

[17] D.R. Grempel, and Q. Si, Phys. Rev. Lett. **91**, 026401 (2003).

[18] L. Zhu, M. Garst, A. Rosch, and Q. Si, Phys. Rev. Lett. **91**, 066404 (2003).

[19] P. Nozieres and A. Blandin, J. Phys. (Paris) **41**, 193 (1980).

[20] A.W.W. Ludwig, and I. Affleck, Phys. Rev. Lett. **67**, 3160 (1991).

[21] O.O. Bernal, D.E. MacLaughlin, H.G. Lukefahr, and B. Andraka, Phys. Rev. Lett. **75**, 2023 (1995).

[22] A.H. Castro Neto, G. Castilla, and B.A. Jones, Phys. Rev. Lett. **81**, 3531 (1998).

[23] A.H. Castro Neto, and B.A. Jones, Phys. Rev. B **62**, 14975 (2000).

[24] J. Garcia Soldevilla, J.C. Gómez Sal, J.A. Blanco, J.I. Espeso, and J. Rodriguez Fernández, Phys. Rev. B **61**, 6821 (2000).

[25] L. Shlyk and J. Stepien-Damm, J. Magn. Magn. Mater. **195**, 37 (1999).

[26] F.G. Gandra, D.P. Rojas, L. Shlyk, L.P. Cardoso, and A.N. Medina, J. Magn. Magn. Mat. **226-230**, 1312 (2001).

[27] S. Pechev, T. Roisnel, B. Chevalier, B. Darriel, and J. Etourneau, Solid State Sci. **2**, 773 (2000).

[28] D.A. Gajewski, R. Chau, and M.B. Maple, Phys. Rev. B **62**, 5496 (2000).

[29] D.X. Li, Y. Shiokawa, Y. Homma, A. Uesawa, A. Dönni, T. Suzuki, Y. Haga, E. Yamamoto, T. Honma, and Y. Onuki, Phys. Rev. B **57**, 7434 (1998).

[30] T. Nishioka, Y. Tabata, T. Taniguchi, and Y. Miyako, J. Phys. Soc. Jpn. **69**, 1012 (2000).

[31] D. Huo, J. Sakurai, T. Kuwai, Y. Isikawa, and Q. Lu, Phys. Rev. B **64**, 224405 (2001).

[32] V.H. Tran, F. Steglich, and G. André, Phys. Rev. B **65**, 134401 (2002).

[33] D.E. MacLaughlin, O.O. Bernal, R.H. Heffner, G.J. Nieuwenhuys, M.S. Rose, J.E. Sonier, B. Andraka, R. Chau, and M.B. Maple, Phys. Rev. Lett. **87**, 066402 (2001).

[34] R. Vollmer, T. Pietrus, H. von Löhneysen, R. Chau, and M.B. Maple, Phys. Rev. B **61**, 1218 (2000).

[35] M.C. Aronson, R. Osborn, R. Chau, M.B. Maple, B.D. Rainford, and A.P. Murani, Phys. Rev. Lett. **87**, 197205 (2001).

[36] C.H. Booth, D.E. MacLaughlin, R.H. Heffner, R. Chau, M.B. Maple, and G.H. Kwei, Phys. Rev. Lett. **81**, 3960 (1998).

[37] E.D. Bauer, C.H. Booth, G.H. Kwei, R. Chau, and M.B. Maple, Phys. Rev. B **65**, 245114 (2002).

[38] C.H. Booth, E.W. Scheidt, U. Killer, A. Weber, and S. Kehrein, Phys. Rev. B **66**, 140402(R) (2002).

[39] S. Süllow, I. Maksimov, A. Otop, F.J. Litterst, A. Perucchi, L. Degiorgi, and J.A. Mydosh, Phys. Rev. Lett. **93**, 266602 (2004).

[40] S. Süllow, S.A.M. Metnik, T.E. Mason, R. Feyerherm, G.J. Niewenhuys, A.A. Menovsky and J.A. Mydosh, Phys. Rev. B **61**, 8878 (2000).

[41] T. Graf, J.D. Thompson, M.F. Hundley, R. Movshovich, Z. Fisk, D. Mandrus, R.A. Fisher, and N.E. Phillips, Phys. Rev. Lett. **78**, 3769 (1997).

[42] G.M. Kalvius, K. Kojima, M. Larkin, G.M. Luke, J. Merrin, B. Nachumi, Y.J. Uemura, A. Brückel, K. Neumaier, K. Andres, C. Paulsen, G. Nakamoto, and T. Takabatake, Physica B **281-282**, 66 (2000).

[43] C. Tien, J.J. Lu, and L.Y. Jang, Phys. Rev. B **65**, 214416 (2002).

[44] S. Süllow, M.C. Aronson, B.D. Rainford, and P. Haen, Phys. Rev. Lett. **82**, 2963 (1999).

[45] A. Theumann, B. Coqblin, S.G. Magalhaes, and A.A. Schmidt, Phys. Rev. B **63**, 054409 (2001).

[46] M. Kiselev, K. Kikoin, and R. Oppermann, Phys. Rev. B **65**, 184410 (2002).

[47] R.B. Griffiths, Phys. Rev. Lett. **23**, 17 (1969).

[48] G.F. Zhou, and H. Bakker, Phys. Rev. Lett. **72**, 2290 (1994).

[49] G. Lapertot, R. Calemczuk, C. Marcenat, J.Y. Henry, J.X. Boucherle, J. Flouquet, J. Hammann, R. Cibin, J. Cors, D. Jaccard, and J. Sierro, Physica B **186-188**, 454 (1993).

[50] S.A.M. Mentink, G.J. Nieuwenhuys, A.A. Menovsky, J.A. Mydosh, H. Tou, and Y. Kitaoka, Phys. Rev. B **49**, 15759 (1994).

[51] H. Gu, J. Tang, A. Matsushita, T. Taniguchi, Y. Tabata, and Y. Miyako, Phys. Rev. B **65**, 024403 (2002).

[52] K. Matsuda, Y. Kohori, T. Kohara, K. Kuwahara, and H. Amitsuka, Phys. Rev. Lett. **87**, 087203 (2001).

[53] M. Jaime, K.H. Kim, G. Jorge, S. McCall, and J.A. Mydosh, Phys. Rev. Lett. **89**, 287201 (2002).

[54] I. Maksimov, F.J. Litterst, H. Rechenberg, M.A.C. de Melo, R. Feyerherm, R.W.A. Hendrikx, T.J. Gortenmulder, J.A. Mydosh, and S. Süllow, Phys. Rev. B **67**, 104405 (2003).

[55] A. Yoshimori, and H. Kasai, J. Magn. Magn. Mater. **31-34**, 475 (1983).

[56] P. Coleman, Phys. Rev. B **29**, 3035 (1983).

[57] D.L. Cox, and N. Grewe, Z. Phys. B. **71**, 321 (1988).

[58] P.W. Anderson, Phys. Rev. **109**, 1492 (1958).

[59] N.F. Mott, *Metal-Insulator Transitions*, (Taylor&Francis, London, New York, Philadelphia 1997) p. 35.

[60] P.A. Lee, and T.V. Ramakrishnan, Rev. Mod. Phys. **57**, 287 (1985).

[61] A. Shulte, and G. Fritsch, J. Phys. F **16**, L55 (1986).

[62] B.J. Hickey, D. Greig, and M.A. Howson, Phys. Rev. B **36**, 3074 (1987).

[63] H.H. Boghosian, and M.A. Howson, Phys. Rev. B **41**, 7397 (1990).

[64] P.G. de Gennes, Rev. Mod. Phys. **36**, 225 (1964).

[65] S. Takahashi, and M. Tachiki, Phys. Rev. B **33**, 4620 (1986).

[66] S. Takahashi, and M. Tachiki, Phys. Rev. B **34**, 3162 (1986).

[67] C. Ciuhu, and A. Lodder, Phys. Rev. B **64**, 224526 (2001).

[68] C. Ciuhu, Ph.D. Thesis, (2003), unpublished.

[69] A.A. Golubov, and M.Y. Kupriyanov, Sov. Phys. JETP **69**, 805 (1989).

[70] M.G. Khushainov, JETP Lett. **53**, 579 (1991).

Chapter 3

Physical properties of UCu_4Pd

3.1 Introduction

Non-Fermi liquid (NFL) behavior has first been observed in the pseudobinary heavy fermion alloy $U_{0.2}Y_{0.8}Pd_3$ [1]. Consequently, in the search for NFL behaviour primary alloyed materials have been intensively studied. Andraka and Stewart [2] discovered the first NFL systems with no dilution on the magnetically active f-atom site. These compounds are derived from UCu_5 by doping Pd atoms on the Cu site. UCu_5 is a Kondo lattice antiferromagnet with a Néel temperature of 15 K and a Kondo temperature of 80 K [3, 4]. Upon substitution of Cu by Pd the antiferromagnetism in $UCu_{5-x}Pd_x$ is suppressed, and for x∼2 spin glass behavior appears. In the intermediate range $0.8 < x < 2$, in which no magnetic order is observed, two compounds have been found to exhibit NFL like behavior: $UCu_{3.5}Pd_{1.5}$ and UCu_4Pd. As has been shown by Andraka and Stewart [2], UCu_4Pd shows unusual physical properties below 10 K:

- the electronic specific heat is described by a power law function of temperature $C/T = \Delta T^{-\delta}$, with $\Delta = 450$ mJ/K^2, $\delta = 0.32$;
- the low–field magnetic susceptibility (100 G) follows a power law $\chi \sim T^{-\delta}$;
- the resistivity is found to be linear in T, $\rho = \rho_0(1 - T/T_0)$, with $\rho_0 = 375$ $\mu\Omega$cm, and $T_0 = 60$ K as a characteristic scaling temperature.

These results served as a starting point for further experimental studies on this material and the discussion of the microscopic sources for the NFL behavior in UCu_4Pd. The temperature scaling of quantities like the specific heat, magnetic susceptibility or electrical resistivity plays a crucial role in this discussion, since it has been used to verify the predictions of various theoretical and phenomenological models proposed to account for NFL behavior. However, so far, no theoretical description has emerged which fully accounts for the experimentally observed properties of this system. The low temperature data of UCu_4Pd in part coincide with predictions for different theoretical approaches, but a complete explanation within one model is not possible so far.

For example, later work on UCu_4Pd by Chau and Maple [5] revealed that the susceptibility and electrical resistivity below 10 K can also be parameterized as $\chi(T) = \chi_0 \ln(T/T_0)$, $\chi_0 = 8.7$ memu/moleU, $T_0 = 11$ K, and $\rho(T) = \rho_0(1-T/T_0)$, $\rho_0 = 258\ \mu\Omega$cm, $T_0 = 63$ K. As yet, the pronounced difference between the scaling temperatures T_0 derived from the magnetic susceptibility and the resistivity is not accounted for. Here, very remarkable is the much lower value of ρ_0, as compared to the results of Andraka and Stewart [2], suggesting that the resistivity is strongly sample dependent. Moreover, the magnetic susceptibility is described as a logarithmic function of temperature, unlike the power law dependence reported in Ref [2]. This illustrates the difficulty in distinguishing between different types of scaling functions in such limited temperature ranges, a problem which is inherent to NFL physics.

The physical properties of UCu_4Pd and their temperature scaling in the high temperatures range (from 20 to 300 K) have been discussed by Aronson *et al.* [6]. In particulary these authors carried out inelastic neutron scattering experiments to determine the energy and temperature dependence of the magnetic part of the scattering intensity S. The magnetic response of the system and the corresponding dynamic susceptibility χ'' have been compared to the static susceptibility χ and electrical resistivity ρ. For the incident neutron energies between 2 and 25 meV and temperatures 10 to 300 K it has been shown that

- the magnetic part of the scattering intensity S is temperature independent. In comparison, for a Fermi liquid the temperature is always an important scaling parameter;
- S is not modulated by the wave vector Q, indicating absence of spatial correlations in the system, at least in this energy range;
- χ'' is a function of excitation energy ω, scaled by temperature T, which is the hallmark for NFL excitations: $\chi'' T^{-1/3} \sim \omega/T$;

- the scaling properties of the dynamic susceptibility are consistent with the observed temperature dependence of the static susceptibility $\chi \backsim T^{-1/3}$;
- the electrical resistivity is described by a scaling $\rho \backsim T^{1/3}$.

The question remained if critical spatial spin correlations are accessible at lower energies and temperatures. In later work Aronson *et al.* [7] have demonstrated that for energies ω between 0.2 and 2 meV and the temperature range from 1.6 to 250 K the spatial correlations extend over length scales comparable to the unit cell, and that they show very little temperature dependence (S is wave vector dependent). In addition, these measurements supplied evidence for magnetic frustration in $\mathrm{UCu_4Pd}$. Aronson *et al.* consider three factors limiting the growth of magnetic correlations in $\mathrm{UCu_4Pd}$: composition or structural disorder, magnetic frustration, and the proximity to the Fermi liquid state at the $T = 0, x = 1$ critical point.

Despite the fact that alloying very often introduces disorder in intermetallic compound, $\mathrm{UCu_4Pd}$ has long been treated as an ordered compound, in which Pd and Cu atoms are occupying separate and inequivalent crystallographic sites, as for instance is the case in the $\mathrm{UPt_{5-x}Au_x}$ system with the same crystal structure. However, Booth *el al.* [8] have shown by means of a X–ray absorption fine-structure study that the material is in fact disordered, with $\sim$ 25% Cu/Pd random site exchange [8]. Moreover, indications for the relaxation of disorder have also been found in muon spin resonance μSR measurement. The frequency shift distribution of μSR relaxation data has been considered by MacLaughlin*et al.* [9] as indication for a substantial inhomogeneity of the local magnetic susceptibility in as–cast $\mathrm{UCu_4Pd}$. Finally, Weber *et al.* [10] carried out detailed X–ray, specific heat and electrical resistivity measurements on as–cast and different heat treated $\mathrm{UCu_4Pd}$ samples, in order to analyze the relevance of disorder for the NFL behavior in this system. The X–ray powder diffraction measurements revealed a strong evidence for increasing crystallographic order in the system upon annealing. However, the annealing has a markedly different effect on the behavior of the specific heat and the electrical resistivity. On the one hand, for annealed material, the annealing expands the range of NFL behavior in the specific heat. On the other hand, instead of a NFL-like

$\rho = \rho_0 - AT$ scaling at low temperatures, the electrical resistivity shows a T^2–like dependence. This work, as well as the study of Booth *el al.* [8] demonstrates that the actual level of disorder

- depends on the metallurgical treatment of the material,
- can be reduced through annealing,
- and strongly influences the physical properties of UCu_4Pd, and especially the transport properties.

Furthermore, the resistivity ρ of as–cast UCu_4Pd [2,5,10] closely resembles the behavior observed for the moderately disordered heavy fermion compound URh_2Ge_2. Recent studies on the transport properties of the latter material have shown that here the electronic transport should rather be attributed to disorder induced localization effects than to magnetic scattering [11,12].

Altogether, as central question arises if the resistivity in moderately disordered UCu_4Pd truly probes the magnetic ground state properties of the system, as it has been assumed so far, or if it reflects disorder induced localization in a strongly correlated electron material. In the present study we intend to investigate this issue in detail.

In the following section 3.2 the crystallographic structure of the compound and the structural disorder will be discussed. In section 3.3 the metallurgical analysis of the samples will be presented, with a focus on the results of electron probe microanalysis (EPMA). This method allows to determine the presence even of small amounts of secondary phases in a material, which is particulary important for pseudo–binary compounds. Our study of the physical properties consists of measurements carried out on as–cast and thermally treated polycrystalline UCu_4Pd samples. We investigated in detail the magnetization, magnetic susceptibility and the electric resistivity of the samples for temperatures 2 to 300 K. In our discussion we compare the data with previously published results (section 3.4 and 3.5). As yet, the mechanism that triggers the transition from a quasi-insulating to a metallic like state in the resistivity of UCu_4Pd upon annealing is not understood and will be discussed here. Moreover, annealing induced modifications of the band structure, like a closing of a pseudogap, had not been considered so far. To address this issue we estimated the carrier density from Hall effect measurement (section 3.6). Finally the magnetotransport as tool to distinguish between magnetic and nonmagnetic scattering components has not been investigated in detail previously. Therefore, we carried out magnetoresistance measurements in magnetic fields up to 5.5 T and temperatures from 2 to 300 K (section 3.7).

3.2 Crystallographic structure

UCu_5 crystallizes in the cubic $AuBe_5$ structure. The basic cubic structure of $AuBe_5$ is maintained in the $UCu_{5-x}Pd_x$ system up to a Pd concentration of $x \sim 2.3$, while above this value a mixture of cubic and hexagonal phases is observed. For $4 < x < 5$ a hexagonal or cubic phase is expected, depending on the preparation conditions [5].

Upon substitution of Pd atoms for the Cu ions the lattice constant of $UCu_{5-x}Pd_x$ initially grows linearly, as expected from Vegards law. For $x \geq 1$ the lattice constant increases much faster with growing Pd concentration, but from $1 \leq x \leq 2$ is still described by a linear function [2,10]. This change of slope at $x \sim 1$ is possibly associated to the existence of two inequivalent Cu sites. Under the assumption that for $x = 1$ Pd ions fully occupy one distinct crystallographic site [2], the crystal structure of UCu_4Pd appears as depicted in Fig. 3.1.

In the cubic $UCu_{5-x}Pd_x$ structure, U atoms are placed on the fcc sites denoted as *4a*. Cu and Pd each occupy one of two crystallographically inequivalent sites; labelled *4c* and *16e*. *4c* has cubic symmetry, while *16e* has a trigonal one. Considering the local symmetry, *4a* and *4c* sites are very similar. Each has twelve Cu/Pd *16e* neighbors, and four *4a* (for U sites) or *4c* (for *4c* Cu/Pd sites) neighbors. One unit cell contains four U *4a* sites, four Cu/Pd *4c* sites and sixteen Cu/Pd *16e* sites [8, 13].

If UCu_4Pd possesses a perfectly ordered structure, the Pd atoms occupy the *4c* and Cu the *16e* places. Initially, neutron diffraction experiments on UCu_4Pd seemed to confirm this type of chemical order [14]. However, subsequently, Booth *et al.* [8] have argued that the contrast between the coherent scattering lengths is too low (U: 8.4 fm, Pd: 5.9 fm, Cu: 7.7 fm), and hence that up to 16% Cu occupancy on *4c* sites (instead of Pd) will

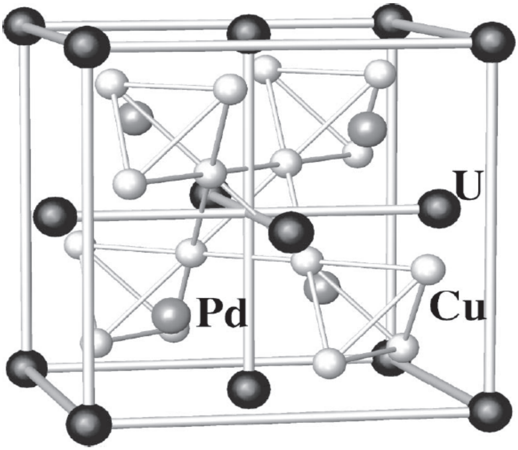

Figure 3.1: The crystal structure of UCu_4Pd.

not be detected in a neutron diffraction measurements. Therefore, they proposed to use in a study of chemical ordering a local probe which is sensitive to the near neighbor bond–length distribution. This can be realized by X–ray absorption fine–structure experiments (XAFS). The method utilizes the interference effect between the outgoing photoelectron waves, produced when an X–ray is absorbed by an atom, and the fraction of this wave that is backscattered from neighboring atoms. In XAFS the absorbing atoms are selected by scanning over the X–ray energy range. This technique provides information about the distances to and the number of neighboring atom from the point of view of the chosen atoms species. XAFS does not make use of the long range translation symmetry, and thus allows to identify the local deviations of atomic positions from their nominal sites (through defects or local distortions), as opposed to traditional diffraction techniques. The XAFS data are analyzed using a least–squares fitting procedure in which the data is fitted to a sum of XAFS atom–par standards, determined by the number of neighbors and positions of the backscattering atoms. The XAFS function $\chi(k)$ is defined as the quotient of atom absorption coefficient $\mu(k)$ and the embedded-atom absorption coefficient $\mu_0(k)$, both dependent on the photoelectron wave vector k [8, 15]:

$$\chi(k) = \frac{\mu(k)}{\mu_0(k)} - 1. \tag{3.1}$$

Booth *et al.* [8, 13] carried out XAFS experiments on an as–cast UCu_4Pd sample using the U L_{III} edge, the Pd K edge and the Cu K edge. The Pd K-edge data are particulary important for the accurate determination of the local structure in UCu_4Pd. As the local symmetry of *4c* and *16e* crystallographic sites are very different, XAFS allows for a precise determination of the Pd amount embedded in local environments characteristic for these sites. The Fourier transform of the $k^3\chi(K)$ of this edge is shown in Fig. 3.2. The main peak in this transform is primarily due to the Pd–Cu pairs, the small shoulder on the right side represents the signal from Pd–U pairs. An optimal fit of the data is obtained if Pd/Cu site exchange is taken into account, with a disorder level of 24 ±3% Pd occupancy on nominal Cu sites, and vice versa.

3.3 Metallurgy of UCu_4Pd

The samples of as–cast and annealed UCu_4Pd have been prepared at the Kamerlingh Onnes Laboratory (Leiden University) by R.W.A. Hendrikx and will be labelled as **L**. For comparison, we include data taken on samples prepared by the San Diego **S** and Augsburg **A** groups [5, 10]. The samples were prepared under similar conditions, by arc–melting the constituents in stoichiometric ratio in a high–purity argon atmosphere on a water–cooled copper crucible. In order to improve homogeneity, the samples were re–melted and flipped over after each melting process several times. Subsequently, three samples have been annealed under various conditions. Altogether, the samples investigated in this paper are as–cast: $\mathbf{S}_{as}$, $\mathbf{A}_{as}$ and $\mathbf{L}_{as}$; annealed in an evacuated quartz glass tube at 750°C for 7 days: $\mathbf{A}_{1ann}$; at 900 °C for 7 days: $\mathbf{L}_{ann}$; and at 750°C for 14 days: $\mathbf{A}_{2ann}$. Homogeneity of the samples **S** and **A** has been tested by X–ray diffraction, where no impurity phases could be detected (for details see Refs. [5, 10]). As well, for the samples **L** secondary phases are not detected in X–ray diffraction. However, electron probe micro analysis EPMA carried out on $\mathbf{L}_{as}$ and $\mathbf{L}_{ann}$ reveals

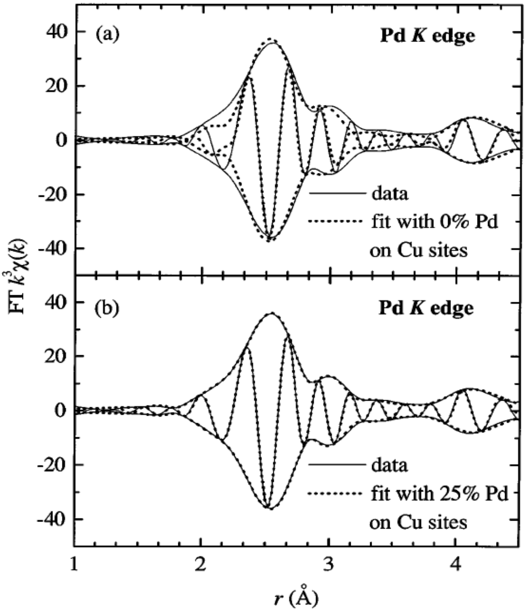

Figure 3.2: Fourier transform of $k^3\chi(k)$ from the Pd K edge for as–cast UCu$_4$Pd. The solid lines represent the data taken at $T = 3.3$ K. The dotted lines correspond to fits assuming (a) a perfectly ordered structure, with Pd and Cu each occupying two inequivalent crystallographic sites and (b) 25% Pd/Cu site exchange [8].

the presence of small inclusions of secondary phases. As a typical example an electron–backscattering photograph of $\mathbf{L}_{ann}$ is displayed in Fig. 3.3. The black spots and white crystals represent areas with a composition deviating from the nominal 1:4:1. In the backscattering mode regions with a relatively higher concentration of a heavy element appear lighter. Therefore, the black spots are U depleted, while the white crystal is rich in uranium. In Table 3.1 we summarize the measured composition and volume amount for the samples **L**. The size of the black inclusions is similar to the sample volume probed by the EPMA electron beam (diameter ~ 1 μm; see Fig. 3.3) [16]. Hence, in the analysis part of the surrounding matrix will con-

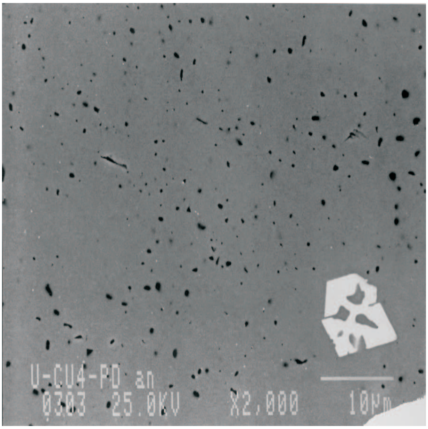

Figure 3.3: Electron–backscattering photograph of the annealed sample UCu$_4$Pd, $\mathbf{L}_{ann}$. Note the 10 μm scale given at the lower right.

tribute to the measured signal in a way that the U and Pd compositions are overestimated. In consequence, the black spots (2nd phase) likely are inclusions of pure copper. The white crystal (3rd phase) we believe to be a uranium oxide, which is very stable and, since the light element oxygen is difficult to be measured in EPMA in the presence of heavy elements, would appear as uranium rich area.

Sample	Matrix Vol. %	2nd Vol. %	3rd Vol. %
$\mathbf{L}_{as}$	1:4.10(12):1.09(3) 94	0.12:1:0.14 5	1:0.11:0.01 1
$\mathbf{L}_{ann}$	1:3.94(12):1.05(3) 96	0.04:1:0.06 3	1:0.06:0.01 1

Table 3.1: The result of the electron probe micro analysis of the samples UCu$_4$Pd, $\mathbf{L}_{as}$ and $\mathbf{L}_{ann}$. Compositions of matrix, 2nd and 3rd phase are given as U:Cu:Pd; for details see text.

3.4 Magnetic properties of UCu_4Pd

The $UCu_{5-x}Pd_x$ system possesses a rich magnetic phase diagram. Here in Fig. 3.4, we present a summary of the phase diagrams proposed in the Ref. [2, 5, 17, 18] and derived from the specific heat, magnetic susceptibility and high field magnetization measurements. Upon substitution of Pd for Cu in $UCu_{5-x}Pd_x$ the antiferromagnetic transition temperature T_N is gradually suppressed from 15 K for UCu_5 to 2 K for $UCu_{4.2}Pd_{0.8}$. The temperature scaling of the physical properties of UCu_4Pd, $UCu_{3.75}Pd_{1.25}$ and $UCu_{3.5}Pd_{1.5}$ hints at the existence of two NFL regions. The NFL–I region, which has been interpreted as a Griffiths phase [5, 17], is replaced above a characteristic temperature T^* by NFL–II. Furthermore, a spin glass like behavior has been observed for UCu_4Pd and $UCu_{3.5}Pd_{1.5}$ at very low temperatures, with the freezing temperature T_f of 0.25 K and 0.10 K, respectively. For $UCu_{3.75}Pd_{1.25}$, however, there is no indication of any kind of magnetic ordering down to a lowest measured temperature of 0.03 K. For the compounds with a Pd concentration above $x = 2$, the paramagnetic behavior is present down the spin glass freezing temperature T_f. Moreover, the magnetic phase diagram as depicted in Fig. 3.4 shows that the NFL-I phase is quickly suppressed for all $x \neq 1$. This makes UCu_4Pd particulary suitable for a study of the sources of NFL behavior in the system $UCu_{5-x}Pd_x$. Although the focal point of our study consists in extensive transport measurements, we also carried out a detailed study of the magnetization (**L** samples) and the magnetic susceptibility (**A** and **L** samples), in order to characterize the magnetic ground state of our sample UCu_4Pd. The magnetization and the dc susceptibility measurements were performed in a commercial Superconducting Quantum Interference Device (SQUID) magnetometer. We analyze the data in connection with the different temperature scaling procedures proposed for this NFL system. Especially, the extended susceptibility study, which has been carried out for five different samples in the temperature range from 2 to 300 K allows a critical discussion of the applicability of scaling approaches and the reliability of there predictions.

The magnetization for the samples $\mathbf{L}_{as}$ and $\mathbf{L}_{ann}$ as a function of the magnetic field $B \leq 5.5$ T is displayed in Figs. 3.5 and 3.6, respectively. The isotherms were taken in the temperature range 3 to 25 K and show a linear

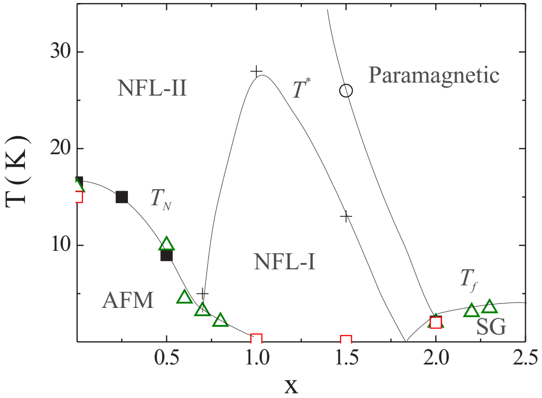

Figure 3.4: Magnetic phase diagram of UCu$_{5-x}$Pd$_x$. The different symbols represent the measurements carried out by: Andraka and Stewart [2] (filled squares), Chau *et al.* [5] (open triangles) and [17] (open circle and crosses), Vollmer *et al.* [18] (open squares).

dependence for both as–cast and annealed sample, with the magnetization values slightly increasing towards low temperatures. Previous magnetization measurements on UCu$_4$Pd indicated deviations from a linear behavior [17, 18] in this magnetic field range at lowest temperatures. However, this non–linearity might be caused by the presence of isolated paramagnetic impurities features, and is not considered here as an intrinsic feature to UCu$_4$Pd. The dc magnetic susceptibility measurement ($\chi \equiv M/H$) has been performed in a low magnetic field of $B = 0.001$ T for both **L** samples and $B = 0.01$ T for the **A** samples (Figs. 3.7 and 3.8). The overall temperature dependence of the magnetic susceptibility is very similar to that previously published for as–cast UCu$_4$Pd [5, 6, 13]. The magnetic susceptibility of the annealed samples at low temperature is smaller than of the as–cast samples, but shows no additional features.

At high temperatures the magnetic susceptibility can be described with

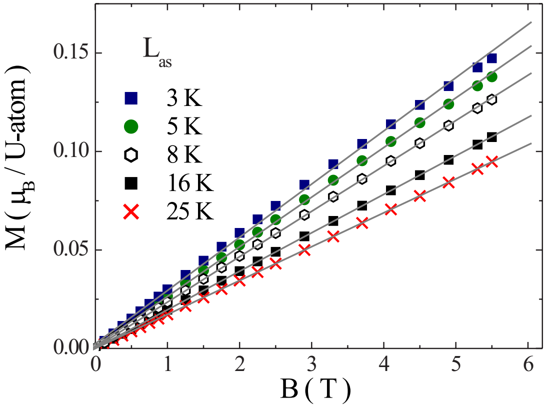

Figure 3.5: Magnetization M *vs.* applied magnetic field of $\mathbf{L}_{as}$. Lines represent linear fits to the data.

a Curie–Weiss law:

$$\chi = \frac{C}{T - \Theta_{CW}} \tag{3.2}$$

where $C = \frac{N_A \mu_{eff}^2}{3k_B}$, Θ_{CW} is the Curie–Weiss temperature, and μ_{eff} as effective moment in Bohr magnetons. In case of $\mathbf{L}_{as}$, a linear fit to χ^{-1} yields a value of $\mu_{eff} = 3.78\ \mu_B$ and a very low $\Theta_{CW} = -213$ K for temperatures from 300 to 200 K. In the temperature range from 200 to 80 K χ^{-1} is also a linear function of temperature, but with a clearly different slope. A Curie–Weiss fit yields a μ_{eff} of $\sim\ 3.46\mu_B$ and $\Theta_{CW} \sim -140$ K. For $\mathbf{L}_{ann}$ the analysis results in $\mu_{eff} = 3.13\ \mu_B$; $\Theta_{CW} = -132$ K and $\mu_{eff} = 3.20\ \mu_B$; $\Theta_{CW} = -140$ K for the temperature ranges 300 to 200 K and 200 to 80 K, respectively. It seems to suggest that the presence of two temperature ranges in the T scaling of χ^{-1} is related to the actual level of disorder, as for the annealed sample these linear fits for this two temperature regime lead to very similar results.

However, as can be gathered from Fig. 3.9 this assumption is not confirmed by the measurements on the **A** samples. As–cast $\mathbf{A}_{as}$ and annealed $\mathbf{A}_{2ann}$ show a very similar χ^{-1} *vs.* T dependence, with a linear scaling over

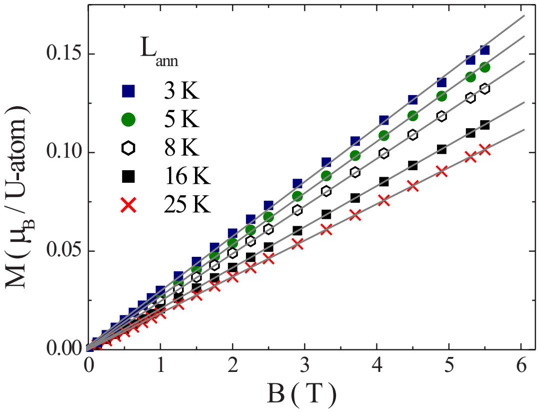

Figure 3.6: Magnetization *M* *vs.* applied magnetic field of $\mathbf{L}_{ann}$. Lines represent linear fits to the data.

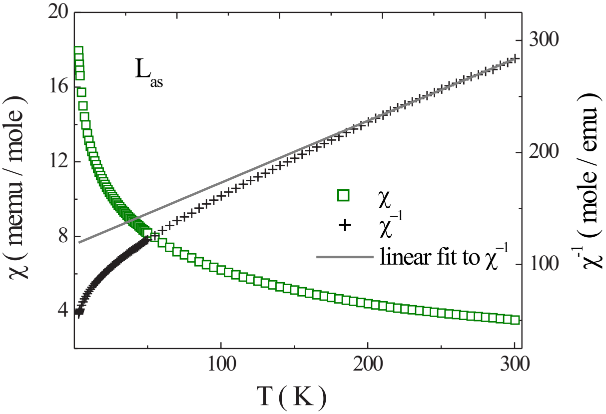

Figure 3.7: Magnetic susceptibility of $\mathbf{L}_{as}$ plotted *vs.* temperature. The solid line indicates a Curie–Weiss fit to the data, see Table 3.2.

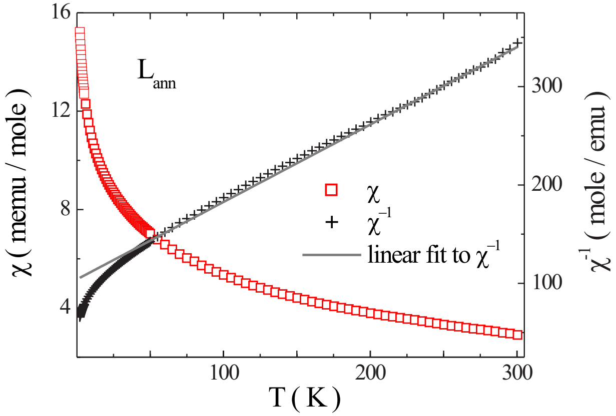

Figure 3.8: Magnetic susceptibility of $\mathbf{L}_{ann}$ plotted *vs.* temperature. The solid line indicates a Curie–Weiss fit to the data, see Table 3.2.

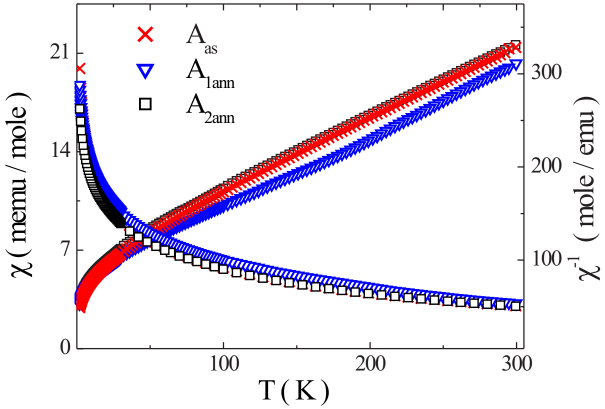

Figure 3.9: The susceptibility χ and the inverse susceptibility χ^{-1} of the **A** samples plotted *vs.* temperature.

Sample	fitting range (K)	μ_{eff} (μ_B)	Θ_{CW} (K)
$\mathbf{L}_{as}$	200-300	3.78	-213
$\mathbf{L}_{as}$	80-200	3.46	-140
$\mathbf{L}_{ann}$	200-300	3.13	-132
$\mathbf{L}_{ann}$	80-200	3.20	-140
$\mathbf{A}_{as}$	80-300	3.21	-126
$\mathbf{A}_{1ann}$	200-300	3.12	-79
$\mathbf{A}_{1ann}$	80-200	3.39	-128
$\mathbf{A}_{2ann}$	80-300	3.19	-125

Table 3.2: Magnetic properties of UCu$_4$Pd. The values of the effective moment μ_{eff} and the Curie–Weiss temperature are extracted from Curie–Weis fits to the high–temperature magnetic susceptibility.

the temperature range of 300 to 80 K. The annealed $\mathbf{A}_{1ann}$ sample, however, shows a change of slope in the linear scaling of χ^{-1} *vs.* T at 200 K, as it has been observed for the **L** samples. We summarize the results of the Curie–Weiss fits in Table 3.2.

Effective moments of $\mu_{eff} = 3.00 - 3.44\ \mu_B$ and low Curie-Weiss temperatures $\Theta_{CW} \sim -60$ to -260 K have also been observed for UCu$_{5-x}$Pd$_x$ with Pd concentration $x = 0 - 2.2$ at T > 200 K [2,13] or for $100\ K \geq T \leq 400$ K [19], respectively. The values of the effective moments are, with the exception of $\mathbf{L}_{as}$, in the temperature range 300 to 200 K, lower than expected for uranium ions: $5f^1$ ($\mu_{eff} = 3.54\ \mu_B$) $5f^2$ ($\mu_{eff} = 3.58\ \mu_B$), $5f^3$ ($\mu_{eff} = 3.62\ \mu_B$) or $5f^4$ ($\mu_{eff} = 3.68\ \mu_B$). Possibly, this might indicate the presence of crystalline electric fields and/or the Kondo effect [13] modifying the temperature dependence of the magnetic susceptibility.

For high temperatures Aronson *et al.* [6] proposed a NFL scaling of the static magnetic susceptibility as:

$$\chi = \chi_0 + \alpha T^{-1/3}, \tag{3.3}$$

which has been considered as a hallmark of the NFL behavior. The magnetic susceptibility of $\mathbf{L}_{as}$, $\mathbf{A}_{as}$ and $\mathbf{A}_{2ann}$ can be plotted as a function of $T^{-1/3}$ in the temperature ranges 120–300 K, 80–300 K and 80–300 K respectively (Figs. 3.10 and 3.11). The fit parameters are similar for all samples, with

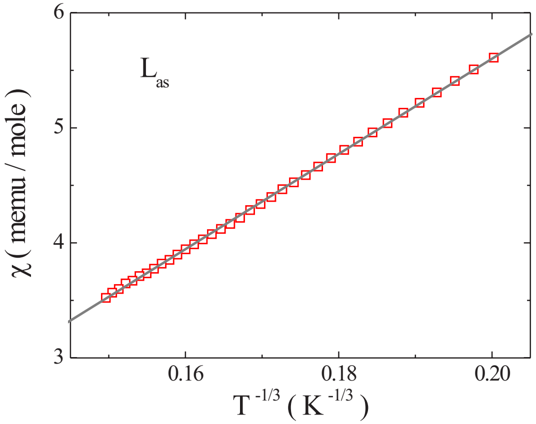

Figure 3.10: The temperature dependence of the magnetic susceptibility of $\mathbf{L}_{as}$, $\chi \sim T^{-1/3}$ for 120 K$< T <$300 K. The solid line is a fit to the data, for details see text.

$\chi_0 \sim -3$ (memu/mole) and $\alpha \sim 4$ ($K^{1/3}$memu/mole). For $\mathbf{L}_{ann}$ and $\mathbf{A}_{1ann}$, the $T^{-1/3}$ scaling dose not apply. Instead, χ follows a dependence

$$\chi = \chi_0 \times \ln\left(\frac{T}{T_0}\right) \tag{3.4}$$

for a wide temperature range $\sim$ 4 K to 300 K, with the fit parameter: $\chi_0 = -2.4$ memu/mole; $T_0 = 1021$ K for $\mathbf{L}_{ann}$ and $\chi_0 = -2.9$ memu/mole; $T_0 = 920$ K for $\mathbf{A}_{1ann}$, respectively (see Fig. 3.12). Deviations from this fit are observed below 4 K, where the magnetic susceptibility diverges even faster upon lowering temperature. In case of $\mathbf{L}_{as}$ and $\mathbf{A}_{2ann}$ the ln scaling is only possible below 12 K (Eq. 3.4). In contrast, the susceptibility of $\mathbf{A}_{as}$ is not a $\ln(T)$ function in any temperature range (see Fig. 3.13). The parameters of the fit functions are given in Table 3.3. The logarithmic temperature dependence of the magnetic susceptibility is also taken as a one of the essential signatures of NFL behavior, indicating that the Kondo disorder model may apply.

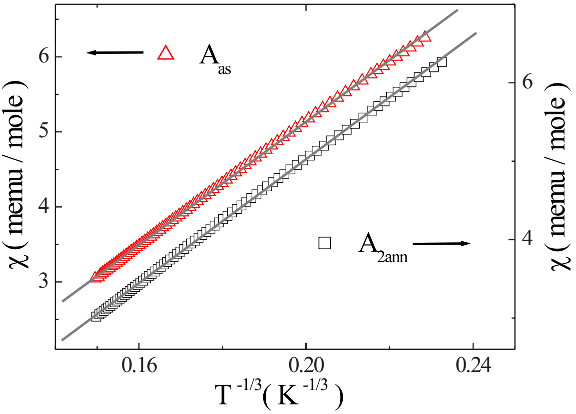

Figure 3.11: The temperature dependence of the magnetic susceptibility of $\mathbf{A}_{as}$ and $\mathbf{A}_{2ann}$, $\chi \sim T^{-1/3}$ for 80 K< T <300 K. The solid lines are fits to the data, for details see text.

In previous studies on UCu$_4$Pd mainly the magnetic susceptibility of the as–cast samples has been investigated. For these samples only the low temperature data of the magnetic susceptibility can be fitted as a logarithmic function of temperature. For example, Ref. [5] reported values of χ_0 = 8.7 memu/mole and T_0 = 11 K for as–cast sample and at temperatures below 10 K. However, we suspect that the fit in Ref. [5] is to some degree intrinsic inconsistent, as the fit formula Eq. 3.4 is declared to be used, which would rather lead to the negative χ_0 values (as χ increases with decreasing T). Bauer *et al.* [13] proposed a different fit expression to the $\chi(T)$ data:

$$\chi = \chi_0^* - c \times \ln(T) \tag{3.5}$$

with $\chi_0^* = 20$ memu/mole and $c = 3.3$ lnK memu/mole for as–cast UCu$_4$Pd. We prefer the notation in which the ln of a quantity is always considered to be dimensionless. The fit parameters of the Eqs. 3.5 and 3.4 are related to each other as following: $c = -\chi_0$, $\chi_0^* = -\chi_0 \times \ln(T_0)$, using the normalization on ln(1K). The $c = -\chi_0$ values of $\mathbf{L}_{as}$ and as–cast sample by Bauer *et al.* [13]

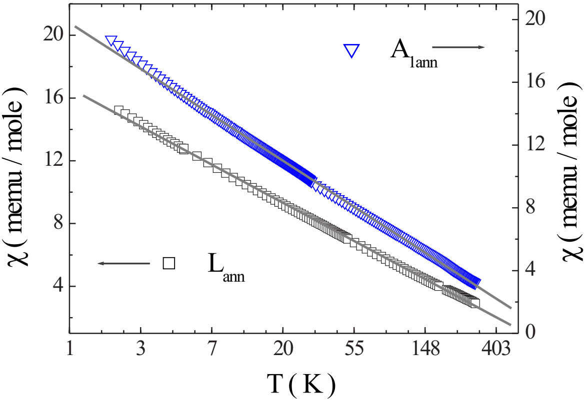

Figure 3.12: Magnetic susceptibility of $\mathbf{L}_{ann}$ and $\mathbf{A}_{1ann}$ on a logarithmic temperature scale, the solid lines are fits to the data, for details see text.

are very similar in opposite to T_0 (Table 3.3).

In case the Griffiths–McCoy singularity lies at the origin of NFL behavior at the low temperatures, as it has been discussed in the Chapter 2, a power law behavior is expected to occur above a the crossover temperature T^* in physical quantities such as magnetic susceptibility or specific heat. Below T^*, magnetic susceptibility and specific heat diverge stronger than a power law, and do not scale together. This model is of particular interest, because if the interactions between clusters are taken into account, it is possible that the system undergoes a spin-glass transition at low temperatures [20], and as it has been observed experimentally [21, 22]). Hence, we plotted the magnetic susceptibility in the low temperature range as a function:

$$\chi = A \times T^{-\eta} \tag{3.6}$$

Instead of A, χ_0 was used in the Ref. [2] as proportionality constant, which we consider misleading as it does not posses the unit of the magnetic susceptibility. The results are listed in Table 3.4. The fit parameters of different as–cast samples match remarkably well. For the annealed samples we have noticed very similar values η, but some discrepancies in the A values.

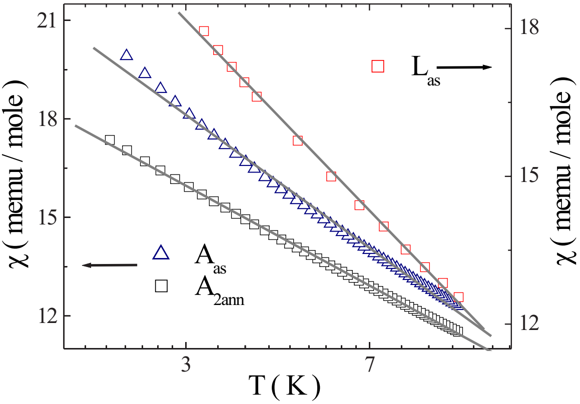

Figure 3.13: Magnetic susceptibility of $\mathbf{L}_{as}$, $\mathbf{A}_{as}$, and $\mathbf{A}_{2ann}$ on a logarithmic temperature scale, the solid lines are fits to the data, for the detail see text.

Summarizing, it appears to be very difficult to unambiguously determine the scaling giving the best description to the susceptibility data. The choice of the best fit to the data is complicated because of the narrow, low temperature range, where logarithmic and exponential functions match the measurements equally well. Therefore, it is essential in the discussion of the theoretical and the applicability of NFL models to consider scaling functions of others physical properties such as specific heat or electrical resistivity, in order to identify one model, able to describe all the unusual properties of the system.

Sample	scaling range (K)	χ_0 (memu/mole)	T_0 (K)
$\mathbf{L}_{as}$	2 - 12	-3.9	294
$\mathbf{L}_{ann}$	2 - 300	-2.4	1012
$\mathbf{A}_{as}$	-	-	-
$\mathbf{A}_{1ann}$	2 - 300	-2.9	920
$\mathbf{A}_{2ann}$	2 - 12	-3.0	565
Ref. [5]*	2 - 10	8.7	11
Ref. [13] **	2 - 12	-3.3	428

Table 3.3: Fit parameter of the magnetic susceptibility according to the fit function: $\chi = \chi_0^* - c\times\ln(T)$. The magnetic susceptibility of $\mathbf{A}_{as}$ cannot be described as a logarithmic function of T. ** values are calculated from the values c and χ_0^* given in Ref. [13].

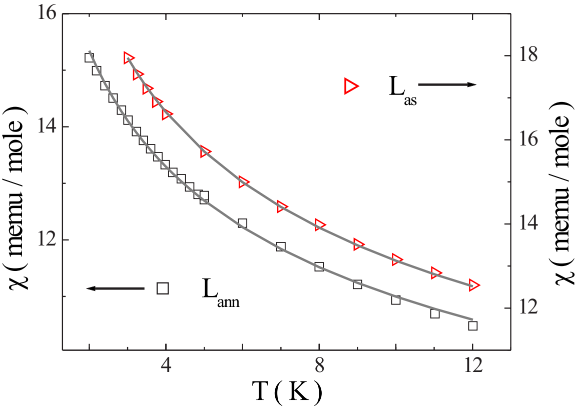

Figure 3.14: Magnetic susceptibility of $\mathbf{L}_{as}$, $\mathbf{L}_{ann}$ in the low temperature range. The lines represent fits $\chi = A \times T^{-\eta}$, for the details see text.

Sample	η	A (K^{η}memu/mole)
$\mathbf{L}_{as}$	0.26	23.9
$\mathbf{L}_{ann}$	0.21	17.8
$\mathbf{A}_{as}$	0.26	23.8
$\mathbf{A}_{1ann}$	0.21	21.4
$\mathbf{A}_{2ann}$	0.22	19.9
Ref. [13]	0.26	-
Ref. [19]*	0.27	-

Table 3.4: Fit parameters to the magnetic susceptibility for $\chi = A \times T^{-\eta}$ below 12 K (with the exception of *, where scaling range: 2-20 K). In case of the data from Ref. [13] and Ref. [19] the as–cast sample has been measured, A values have not been reported.

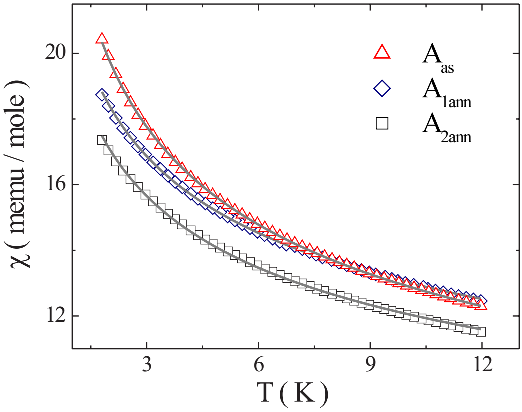

Figure 3.15: Magnetic susceptibility of the samples **A** in the low temperature range. The solid lines are the fits to the data with $\chi = A \times T^{-\eta}$; the parameters **A** and η are listed in Table 3.4.

Sample	$\rho_0(\mu\Omega\text{cm})$	T_0(K)	T_1(K)
$\mathbf{S}_{as}$	429	74	14
$\mathbf{L}_{as}$	304	68	12
$\mathbf{A}_{as}$	412	55	8
Ref. [5]	258	64	10

Table 3.5: The parameters resulting from a fit of the low temperature resistivity $\rho(T) = \rho_0(1 - T/T_0)$ of as–cast UCu_4Pd; for details see text.

3.5 Resistivity

The transport measurements have been performed using a common four probe technique at temperatures 2 to 300 K (0.03 to 300 K for $\mathbf{A}_{as}$, $\mathbf{A}_{2ann}$) in a conventional He_4 and He_3 cryostat. For as–cast material $\mathbf{S}_{as}$, $\mathbf{A}_{as}$ and $\mathbf{L}_{as}$ we observe the archetypal behavior of moderately disordered uranium heavy fermion compounds, with a negative $d\rho/dT$ and large absolute ρ values. Notably, while for as–cast material ρ values vary by about 100 $\mu\Omega$cm, the normalized resistivity exhibits a very similar behavior for the three samples. This sample–to–sample variation of ρ indicates that structural disorder affects the transport behavior.

At low temperatures, as it has been stated previously [2], the resistivity is linear in temperature (Figs. 3.16 and 3.17). Following Ref. [5] we fit the resistivity as $\rho(T) = \rho_0(1 - T/T_0)$. The resulting fit parameters are summarized in Tab. 3.5. Here, T_1 denotes the temperature up to which the data are fitted. Again, we find significant differences between the samples, which indicates the presence of disorder.

Annealing the material qualitatively and quantitatively changes the resistive behavior [10]. Comparing $\mathbf{L}_{ann}$, $\mathbf{A}_{1ann}$ and $\mathbf{A}_{2ann}$ we find pronounced sample–to–sample variations. It implies that for annealed material disorder still affects the resistive behavior. Conversely, concerning the overall temperature dependence the annealed samples show a more metallic behavior than the as–cast ones. In particular, for the samples $\mathbf{A}_{1ann}$ and $\mathbf{A}_{2ann}$ a metallic, *i.e.*, positive $d\rho/dT$ occurs for intermediate temperatures, with ρ at lowest T saturating in a single–impurity Kondo like fashion. For $\mathbf{L}_{ann}$, while the absolute value surprisingly is larger than that of the as–cast sample $\mathbf{L}_{as}$, the resistivity ratio $\rho_{2\text{K}}/\rho_{300\text{K}}$ is smaller, that is more metallic, and

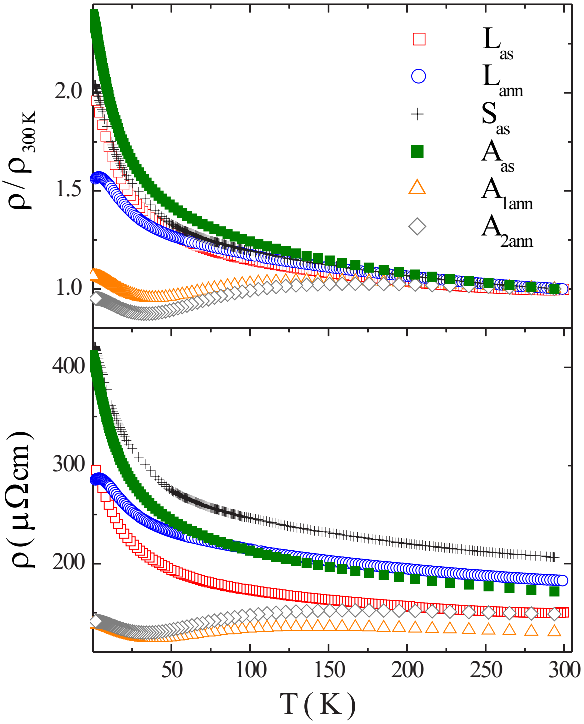

Figure 3.16: The resistivity of as–cast and annealed samples UCu_4Pd as a function of temperature, plotted as normalized data and in absolute units.

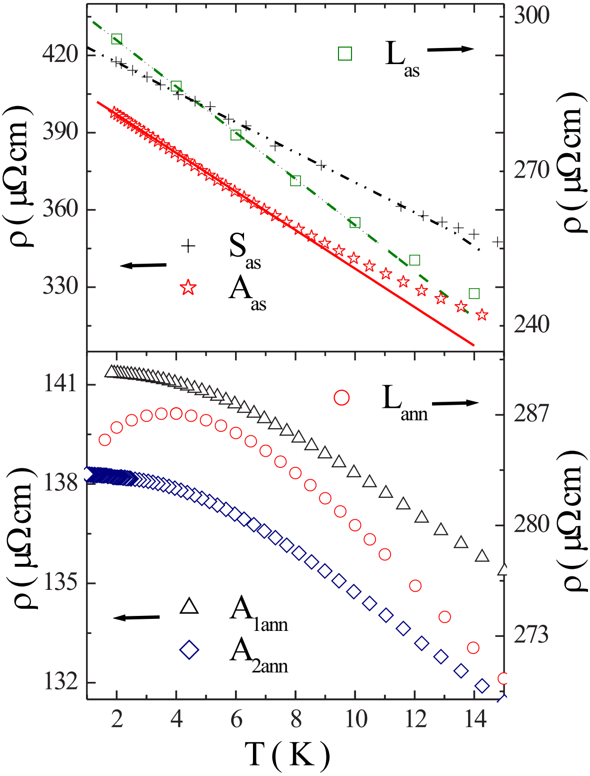

Figure 3.17: The low temperature resistivity of as–cast and annealed samples UCu_4Pd as a function of temperature.

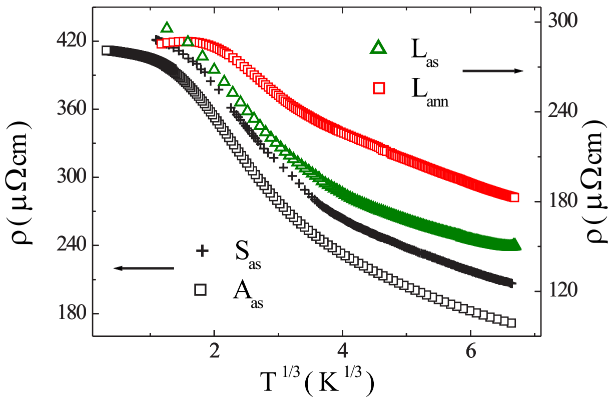

Figure 3.18: The resistivity of as–cast and annealed samples UCu_4Pd as a function of $T^{1/3}$.

at lowest temperatures we observe a shallow maximum at ~ 4 K in ρ.

Since for the annealed sample $\mathbf{L}_{ann}$ we find no anomaly in the T dependence of the susceptibility (see Fig. 3.16) in the temperature range of the resistive maximum, we conclude that the maximum does not correspond to a magnetic phase transition. Instead, it could stem either from regions in our material, in which disorder has been minimized to a degree that a coherent state can be formed, or from a grain boundary phase. We note that for a grain boundary phase there is no metallurgical evidence, as in the EPMA backscattering photo we do not see it. Rather, the topological distribution of secondary phases in the annealed sample is similar to the as–cast one, in which no resistive anomaly was observed.

The high temperature scaling behavior of the physical quantities reported by Aronson *et al.* [6], which we found to apply quite well to the high temperatures magnetic susceptibility of $\mathbf{L}_{as}$, $\mathbf{A}_{as}$, $\mathbf{A}_{2ann}$, the temperature dependence of the electrical resistivity:

$$\rho \sim T^{1/3} \tag{3.7}$$

In Figs. 3.18 and 3.19 we present the electrical resistivity for the as–cast

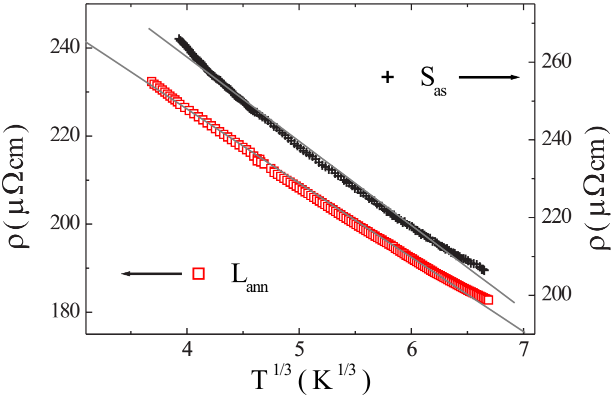

Figure 3.19: The resistivity of as–cast and annealed samples UCu_4Pd as a function of $T^{1/3}$; for details see text.

and $\mathbf{L}_{ann}$ samples plotted *vs.* $T^{1/3}$. For none of the samples we could clearly establish the $T^{1/3}$ scaling. The resistivity of the $\mathbf{S}_{as}$ has been previously reported to be moderately well described with the expression 3.7 [6], this feature can be roughly made out in the temperature range $\sim$ 60 K to 300 K. However, a careful examination of the data in this temperature range indicates that ρ is not described by a $T^{1/3}$ function (see Fig. 3.19). The temperature dependence of the electrical resistivity of $\mathbf{L}_{ann}$ shows the highest similarity to the fit function 3.7, although they are not perfectly described by the function. This is very surprising, as the NFL scaling proposed by in Ref [6] do not apply to the magnetic susceptibility data of $\mathbf{L}_{ann}$. We have not considered the $\mathbf{A}_{1ann}$ and $\mathbf{L}_{2ann}$ samples, since for these samples in the high temperature range a positive $d\rho/dT$ has been observed, as it has been shown in Fig. 3.16. This behavior is in direct contradiction to the fit function 3.7 given above.

3.6 Hall effect

To establish the carrier density for UCu_4Pd we have carried out Hall effect measurements on $\mathbf{L}_{as}$ and $\mathbf{L}_{ann}$. In the Figs. 3.20 and 3.21 we plot the temperature dependence of the Hall constant R_H for both samples. Overall, the temperature dependencies of R_H for $\mathbf{L}_{as}$ and $\mathbf{L}_{ann}$ are very similar. However, they are unlike what is expected for archetypical heavy fermion metals [23,24]. Commonly, for heavy fermions a maximum in the T dependence of the Hall constant, assigning the transition into the low temperature coherent state below the coherence temperature T_{coh}, is observed. In UCu_4Pd there is no such maximum, reflecting the absence of coherent scattering in this disordered compound.

The strong T dependence of R_H indicates that it is dominated by anomalous contributions. As usual, for the analysis of the Hall effect data we assume a temperature independent carrier density and a spherical Fermi surface. To extract the carrier density we parameterize the Hall constant as

$$R_H = R_0 + R_A. \tag{3.8}$$

Here, R_0 denotes the normal contribution to the Hall effect and measures the carrier density n. The second term, R_A, represents the anomalous contribution to the Hall effect, with R_A a model dependent factor.

In one of the first Hall effect studied on heavy fermions Schoenes and Franse [25] postulated for the anomalous contribution an empirical ansatz: $R_A \sim \chi$. In an theoretical approach, Fert and Levy [24] proposed the skew scattering. According this model, the scattered carriers are deflected from their original trajectories by a constant spontaneous angle α, as result of spin–orbit scattering. The skew scattering scenario predicts that $R_A \propto \chi\rho_{mag}$, with ρ_{mag} as the magnetic scattering component of the resistivity. For heavy fermion materials, at high temperatures ρ_{mag} is essentially constant, and it goes to zero for $T \rightarrow 0$. Hence, the product $\chi\rho_{mag}$ will exhibit a pronounced maximum at T_{coh}. Alternatively, the coherence maximum in R_H has been explained on basis of the periodic Anderson model [23] as a transition from a regime $T \ll T_{coh}$ with $R_A \propto \rho^2$ to one at $T \gg T_{coh}$, $R_A = \chi$, with ρ now the total resistivity. Finally, for disordered materials the side jump effect has been identified in Hall effect measurements [26], giving

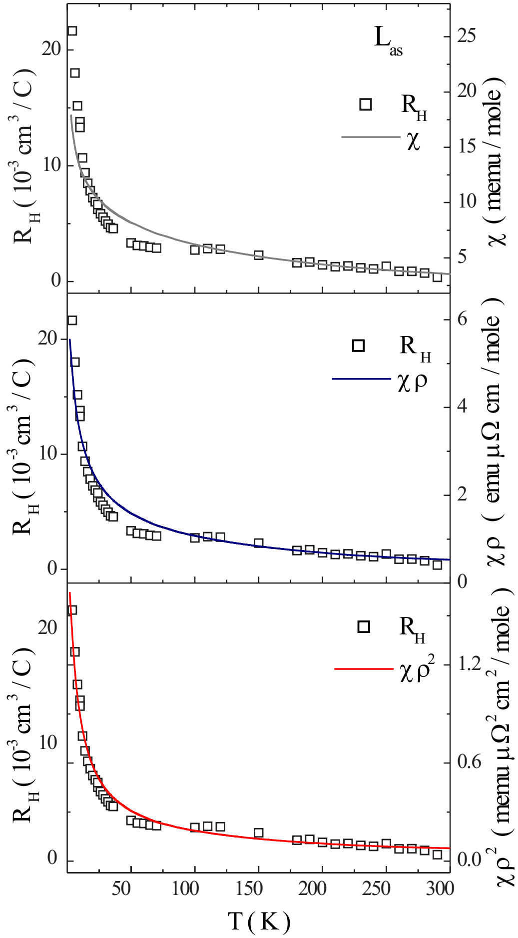

Figure 3.20: The Hall constant of UCu$_4$Pd, $\mathbf{L}_{as}$, as a function of temperature. We include the temperature dependence of the susceptibility χ and of the products $\chi\rho$, $\chi\rho^2$; for details see text.

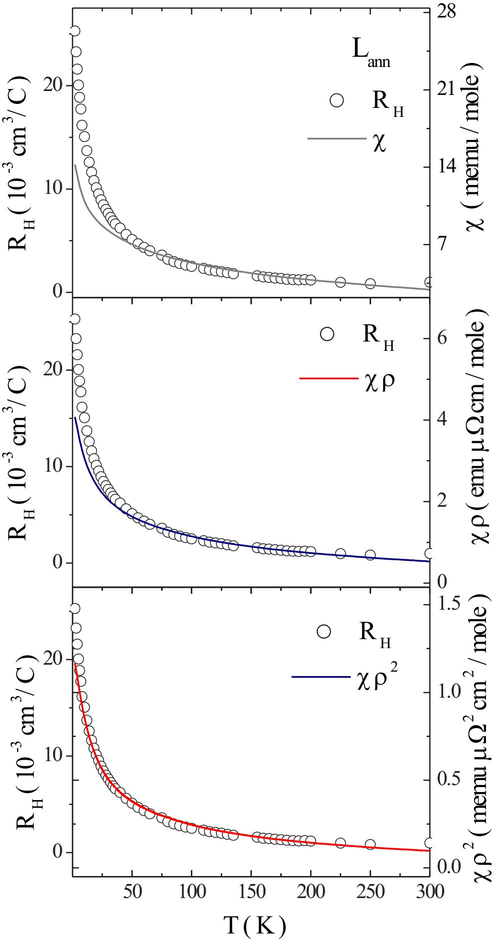

Figure 3.21: The Hall constant of UCu_4Pd, $\mathbf{L}_{ann}$, as a function of temperature. We include the temperature dependence of the susceptibility χ and of the products $\chi\rho$, $\chi\rho^2$; for details see text.

rise to a T dependence $R_A \propto \chi\rho^2$. The side jump mechanism is quantum mechanical in nature and results in a constant lateral displacement Δy of the charge trajectory at the point of scattering. To assess which of these models most adequately describes our data we include the susceptibility χ and the products $\chi\rho$, $\chi\rho^2$ in the Figs. 3.20 and 3.21. All in all, from our comparison we find that at high temperatures our Hall effect data are reproduced by all three scenarios. This simply reflects the comparatively weak T dependence of ρ. Then, by extracting the normal Hall effect contribution $R_0 = (ne)^{-1}$, for both samples we obtain a carrier density n of about 1 to 2 electrons per unit, irrespective of the assumptions made for the anomalous contribution. This carrier density is metallic and disproves the possibility for a gap in the density of states. Furthermore, the annealing induced qualitative changes of the resistivity cannot be associated to the carrier density.

For the overall T dependence of R_H we observe that the matching is best for the product $\chi\rho^2$, the side jump effect scenario. It might indicate a disorder dominated Hall effect, since usually the side jump effect is observed in disordered materials like metallic glasses [27].

In contrast, strictly speaking, for the skew scattering scenario we should have plotted $\chi\rho_{mag}$. However, for the anomalous resistivities of as–cast and annealed $\mathrm{UCu_4Pd}$ a correction for phonon contributions - as it is usually performed - will be an *ad hoc* procedure. Therefore, we use the total resistivity, thereby assuming that it approximates ρ_{mag}. This way, we implicate a magnetic resistive component unlike that used in Ref. [24], as ρ_{mag} for $T \rightarrow 0$ does not approach zero. To our knowledge, aside from hand waving arguments presented in context with Kondo disorder scenarios [20, 28, 29], there is no well-founded model that would explain such a highly anomalous magnetic resistive component. This inconsistency would imply that the skew scattering scenario, as set out by Fert and Levy [24], does not account for the anomalous Hall contribution observed for $\mathrm{UCu_4Pd}$.

3.7 Magnetoresistivity

To test the magnetic resistive component we have carried out magnetoresistivity measurements on $\mathbf{L}_{as}$ and $\mathbf{L}_{ann}$ in magnetic fields up to 5.5 T and 4 T, respectively. The magnetic field was applied perpendicular to the current

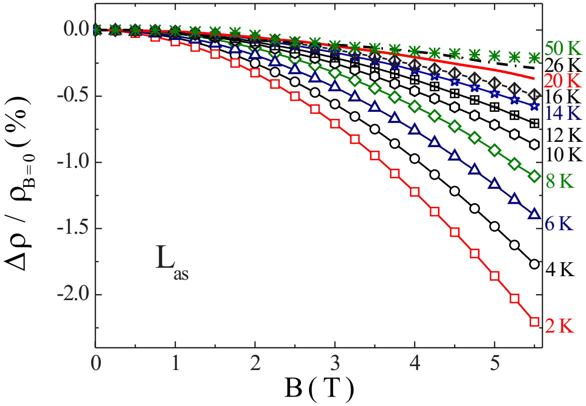

Figure 3.22: The magnetoresistivity of the as–cast sample UCu$_4$Pd, $\mathbf{L}_{as}$.

direction. If the low temperature resistivity of UCu$_4$Pd is mostly magnetic in nature, in a simplified picture, it must be spin disorder scattering. This should be substantially reduced in magnetic fields of a few T. Correspondingly, in Figs. 3.22 and 3.23 we plot the normalized magnetoresistivity, defined as

$$\frac{\Delta\rho}{\rho_{B=0}} = \frac{(\rho(B) - \rho_{B=0})}{\rho_{B=0}} \tag{3.9}$$

as function of magnetic field, at various temperatures for the as–cast and annealed samples $\mathbf{L}_{as}$ and $\mathbf{L}_{ann}$. For $\mathbf{L}_{as}$ we observe negative and comparatively small values of the normalized magnetoresistivity, which decreases from $\sim$ 2.3% at 2 K to 0.2% at 50 K, in a magnetic field of 5.5 T. The magnetoresistivity of the annealed sample is even smaller and does not exceed |0.3%| at 4 T. Furthermore, $\Delta\rho/\rho$ changes sign from positive to negative at around 3 K. To quantitatively compare the magnetoresistivities of $\mathbf{L}_{as}$ and $\mathbf{L}_{ann}$, in Fig. 3.24 we plot the values $\Delta\rho/\rho$ determined in an external field of 4 T.

Additionally, as has been shown in Fig. 3.25 the field dependence of the

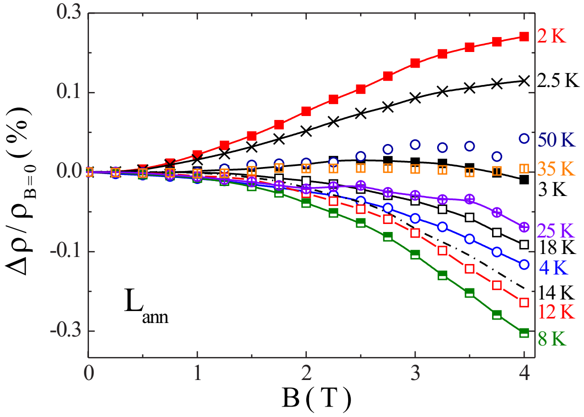

Figure 3.23: The magnetoresistivity of the annealed sample UCu$_4$Pd, $\mathbf{L}_{ann}$.

magnetoresistivity for $\mathbf{L}_{as}$ is up to 30 K well described by

$$\frac{\Delta\rho}{\rho} = \alpha B^2. \tag{3.10}$$

With this parametrization we can determine the temperature dependence of the magnetoresistive coefficient α, as presented in Fig. 3.26. For a comparison, we also include the magnetic susceptibility χ in this Figure. The temperature dependence of α and χ are closely correlated, *i.e.*, (α-α_0) $\sim \chi$. This indicates that spin disorder scattering is the dominant process controlling the field dependence of $\Delta\rho/\rho$ for $\mathbf{L}_{as}$. For $\mathbf{L}_{ann}$, however, the behavior is more complex. While above $\sim$ 15 K the T dependence of $\Delta\rho/\rho$ coincides with that of $\mathbf{L}_{as}$, at low temperatures the magnetoresistivity changes sign. In the resistivity this feature is associated to the shallow maximum at around 4 K (see Fig. 3.16). Since the maximum likely does not represent a bulk phenomenon, we believe that the change of sign of the magnetoresistivity for $\mathbf{L}_{ann}$ as well does not constitute bulk behavior. The overall small magnetoresistivity suggests that the large values of the resistivity mainly do not arise from magnetic scattering. It thus represents additional evidence

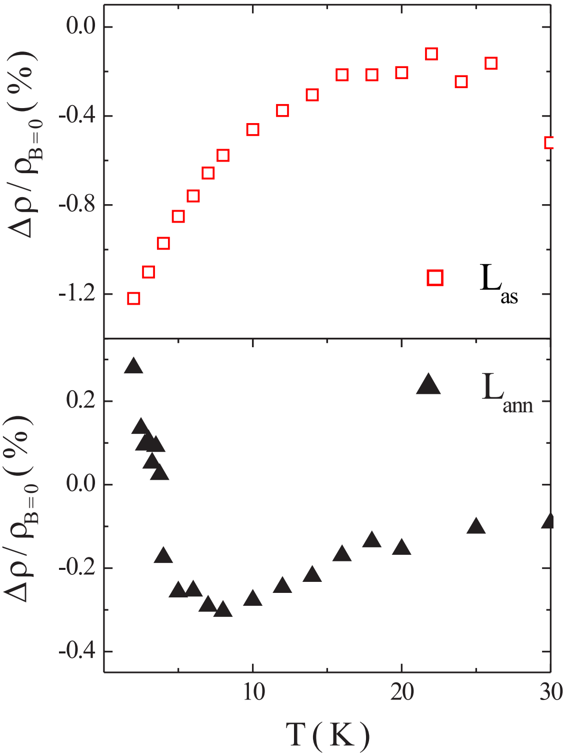

Figure 3.24: The temperature dependence of the magnetoresistivity $\Delta\rho/\rho$ for the as–cast and annealed samples $\mathbf{L}_{as}$ and $\mathbf{L}_{ann}$, determined in an external field of 4 T, for details see text.

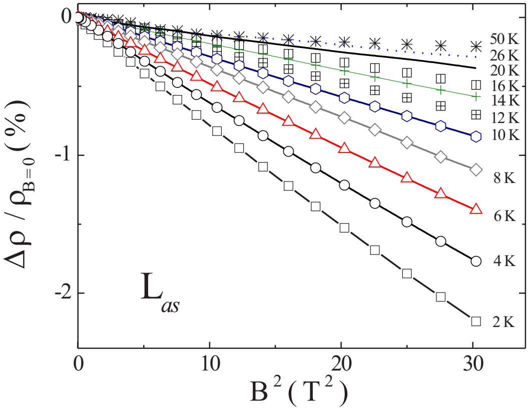

Figure 3.25: The magnetoresistivity of the as–cast sample UCu$_4$Pd, **L**$_{as}$ *vs.* the square of the magnetic field, B^2, with field perpendicular to the current direction.

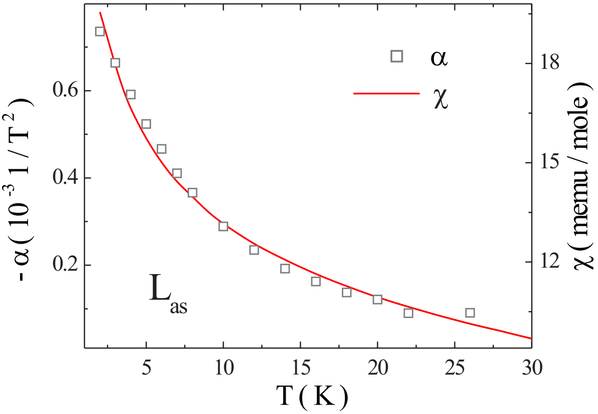

Figure 3.26: The temperature dependence of the magnetoresistive coefficient α. For comparison we include the magnetic susceptibility χ; for details text.

against an interpretation of the anomalous Hall contribution in terms of skew scattering theory [24].

3.8 Discussion

With our data we have established the metallicity of both as–cast and annealed UCu_4Pd. Then, the negative $d\rho/dT$ for the as–cast material must be the result from disorder–induced localization effects. Further, the electronic transport properties of UCu_4Pd closely resemble those of the moderately disordered heavy fermion compound URh_2Ge_2, which again are reminiscent of metallic glasses [12]. For the latter compound the metallic glass like behavior has been quantified by applying the corresponding localization theory to describe the T dependence of the conductivity σ.

Following the procedure set out in Ref. [12], we plot the reduced conductivity $\Delta\sigma = \sigma - \sigma(T = 0)$ as a function of T (Fig. 3.27). By using different scales for $\Delta\sigma$ for the three samples $\mathbf{S}_{as}$, $\mathbf{A}_{as}$ and $\mathbf{L}_{as}$, aside from some minor mismatch at highest T between ($\mathbf{S}_{as}$; $\mathbf{A}_{as}$) and $\mathbf{L}_{as}$, we can superimpose the conductivity data over the complete temperature range. It illustrates the close similarity of the T dependence of the electronic transport properties for the different as–cast samples UCu_4Pd.

To quantify the resemblance to metallic glasses we describe our data in terms of localization theory [12, 30, 31]. For weak electronic correlations (in UCu_4Pd at sufficiently high T) the T dependence of σ is attributed to the superposition of incipient localization, destroyed by inelastic scattering with phonons and electrons, and electronic interaction effects. It is given by [32, 33]

$$\Delta\sigma(T) = \frac{e^2}{2\pi^2\hbar}\left(3\sqrt{b + c^2T^2} - cT - 3\sqrt{b} + d\sqrt{T}\right), \qquad (3.11)$$

with fit parameters $b = 1/D\tau_{so}$, $c = \sqrt{1/4D\beta}$, $\beta = \tau_i T^2$, $d = 0.7367\sqrt{k/D\hbar}$ (diffusion coefficient D, spin-orbit τ_{so} and inelastic τ_i scattering times). Above 50 K the T dependence of $\Delta\sigma$ can be described by Eq. 3.11, validating our statement on the close resemblance to the behavior of amorphous metals. In Fig. 3.27 we include the result of a parameterization of the data for sample $\mathbf{A}_{as}$ as a solid line. The plotted curve has been calculated using

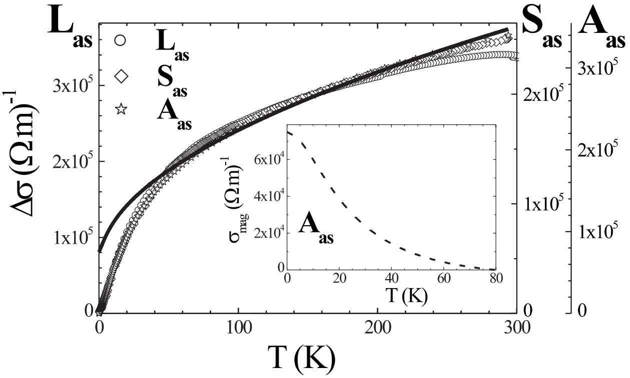

Figure 3.27: The temperature dependence of the reduced conductivity $\Delta\sigma$ for as–cast UCu_4Pd. The solid line depicts the result of a parameterization of the data. In the inset we plot the difference between the parameterization and the experimental data for the sample $\mathbf{A}_{as}$; for details see text.

parameters of $D \sim 6 \times 10^{-8}$ m^2/s; $\tau_{so} \sim 2 \times 10^{-9}$ s; $\beta \sim 2 \times 10^{-7}$ sK^2. Because, by reason of parameter interdependencies, we cannot extract a unique set of fit parameters. Overall, the essential features of the data for the three samples can be reproduced using parameters $D \sim 10^{-7} - 10^{-8}$ m^2/s; $\tau_{so} \sim 10^{-9} - 10^{-10}$ s and $\beta \sim 10^{-7} - 10^{-9}$ sK^2, which are similar in order of magnitude to those obtained for URh_2Ge_2 with $D \sim 10^{-6} - 10^{-7}$ m^2/s; $\tau_{so} \sim 10^{-11}$ s and $\beta \sim 10^{-9}$ sK^2 [12].

While there are still open questions as to the applicability of classical localization theory to the transport properties of a moderately disordered uranium heavy fermion compound, our analysis indicates that in result the behavior of our compound at high enough temperatures is metallic glass like. In particular, with Matthiessen's rule not being valid, it implicates that the transport properties of moderately disordered uranium heavy fermion compounds should be considered in terms of transport through different conductivity channels.

If we proceed in the spirit of localization theory, we can attribute the difference between our parameterization and the experimental data at low temperatures to a conductivity channel which contains a magnetic component. The idea is that at high temperatures this channel fully conducts, but at low temperatures its conductivity is reduced because of magnetic scattering. The reduction of the conductivity of this channel we can determine from $\sigma_{mag} = \Delta\sigma - \sigma_{exp}$, with the data for the sample $\mathbf{A}_{as}$ plotted in the inset of Fig. 3.27. With the uncertainty about the fitting parameters in $\Delta\sigma$ our procedure will only serve to obtain an estimate for the relevance of different transport mechanisms. The value of σ_{mag} at low temperatures, 7×10^4 $(\Omega\text{m})^{-1}$ corresponds to about 30% of the total conductivity of this sample at low temperatures. This is a much more realistic estimate of size of the magnetic contribution to the electronic transport than assuming that the total resistivity reflects magnetic scattering. Moreover, it should be such a "magnetic conductivity channel" which captures the NFL characteristics rather than the T dependence of ρ at low temperatures [34]. Unfortunately, at present there are no theories available which would allow a more detailed analysis here.

Finally, the pronounced sample dependence of the electronic transport properties ought to be addressed. We have demonstrated that aside from differences in absolute values of the conductivity the T dependence for the as–cast samples is essentially the same. This could be explained by assuming that the effective path of the electrical current is different from sample to sample. It would imply that the current in as–cast samples UCu_4Pd follows a percolative path provided by the better ordered regions in the sample. Along this path transport is diffusive and exhibits the characteristic negative $d\rho/dT$ of moderately disordered uranium heavy fermions. If by annealing in some part of this percolative path the disorder is reduced to a degree that transport starts to become ballistic, the superposition of ballistic and diffusive transport will yield a temperature dependence of ρ similar to what is observed experimentally. Here, in order to test such a scenario a local probe experiment of the electronic transport, like scanning tunnelling microscopy or point contact spectroscopy might be useful.

3.9 Summary

In conclusion, we have presented a study of the magnetic and electronic transport properties on as–cast and annealed samples of the moderately disordered uranium heavy fermion UCu_4Pd. We show that an unambiguous choice for a certain temperature scaling model of the magnetic susceptibility, which are attributed to different NFL models, is very problematic.

In our study of the electronic transport properties of UCu_4Pd, we have established the metallicity of the material for both as–cast and annealed material. The data analysis indicates that the electronic transport properties are dominated by disorder-induced localization effects, while there is only a minor magnetic scattering component. This means that the resistivity does not probe the magnetic ground state. The observation casts doubt on claims for NFL behavior detected in the resistivity of this and related compounds.

Bibliography

[1] C.L. Seaman, M.B. Maple, B.W. Lee, S. Ghamaty, M.S. Torikachvili, J.-S. Kang, L.Z. Liu, J.W. Allen, and D.L. Cox, Phys. Rev. Lett. **67**, 2882 (1991).

[2] B. Andraka, and G.R. Stewart, Phys. Rev. B **47**, 3208 (1993).

[3] H.R. Ott, H. Rudiger, E. Felder, Z. Fisk, and B. Batlogg, Phys. Rev. Lett. **55**, 1595 (1985).

[4] U. Walter, M. Loewenhaupt, E. Holland-Moritz, and W. Schablitz, Phys. Rev. B **36**, 1981 (1987).

[5] R. Chau, and M.B. Maple, J. Phys.: Condens. Matter **8**, 9939 (1996).

[6] M.C. Aronson, M.B. Maple, R. Chau, A. Georges, A.M. Tsvelik, and R. Osborn J. Phys.: Condens. Matter **8**, 9815 (1996).

[7] M.C. Aronson, R. Osborn, R. Chau, M.B. Maple, B.D. Rainford, and A.P. Murani, Phys. Rev. Lett. **87**, 197205 (2001).

[8] C.H. Booth, D.E. MacLaughlin, R.H. Heffner, R. Chau, M.B. Maple, and G.H. Kwei, Phys. Rev. Lett. **81**, 3960 (1998).

[9] D.E. MacLaughlin, R.H. Heffner, G.J. Nieuwenhuys, G.M. Luke, Y. Fudamoto, Y.J. Uemura, R. Chau, M.B. Maple, and B. Andraka, Phys. Rev. B **58**, R11849 (1998).

[10] A. Weber, S. Körner, E.-W. Scheidt, S. Kehrein, and G.R. Stewart, Phys. Rev. B **63**, 205116 (2001).

[11] S. Süllow, M.B. Maple, R. Chau, D. Tomuta, G.J. Nieuwenhuys, A.A. Menovsky, and J.A. Mydosh, J. Magn. Magn. Mat. **226-230**, 35 (2001).

[12] S. Süllow, I. Maksimov, A. Otop, F.J. Litterst, A. Perucchi, L. Degiorgi, and J.A. Mydosh, Phys. Rev. Lett. **93**, 266602 (2004).

[13] E.D. Bauer, C.H. Booth, G.H. Kwei, R. Chau, and M.B. Maple, Phys. Rev. B **65**, 245114 (2002).

[14] R. Chau, M.B. Maple, and R.A. Robinson, Phys. Rev. B **58**, 139 (1998).

[15] G.G. Li, F. Bridges, and C.H. Booth, Phys. Rev. B **52**, 6332 (1995).

[16] S. Süllow, T.J. Gortenmulder, G.J. Nieuwenhuys, A.A. Menovsky, and J.A. Mydosh, J. Alloys Comp. **215**, 223 (1994).

[17] R. Chau, M.C. Aronson, E.J. Freeman, and M.B. Maple, J.Phys.: Condens. Matter **12**, 4495 (2000).

[18] G. Vollmer, T. Pietrus, H. v. Löhneysen, R. Chau, and M.B. Maple, Phys. Rev. B **63**, 1218 (2000).

[19] A.M. Strydom, P. de V du Plessis, and R. Troc, J. Phys.: Condens. Matter **11**, 9691 (1999).

[20] A.H. Castro Neto, and B.A. Jones, Phys. Rev. B **62**, 14975 (2000).

[21] E.W. Scheidt, T. Schreiner, K. Heuser, and S. Koerner, Phys. Rev. B **58**, 10104 (1998).

[22] R. Vollmer, S. Mock, T. Pietrus, H. v. Löhneysen, R. Chau, and M.B. Maple, Physica B **230-232**, 603 (1997).

[23] H. Kontani, and K. Yamada, J. Phys. Soc. Jpn. **63**, 2627 (1994).

[24] A. Fert, and P.M. Levy, Phys. Rev. B **36**, 1907 (1987).

[25] J. Schoenes, and J.J.M. Franse, Phys. Rev. B **33**, 5138 (1986).

[26] L. Berger, Phys. Rev. B **11**, 4559 (1970).

[27] F.M. Mayeya, and M.A. Howson, Phys. Rev. B **49**, 3167 (1994).

[28] E. Miranda, V. Dobrosavljevic, and G. Kotliar, Phys. Rev. Lett. **78**, 290 (1997).

[29] E. Miranda, and V. Dobrosavljevic, Phys. Rev. Lett. **86**, 264 (2001).

[30] P.A. Lee, and T.V. Ramakrishnan, Rev. Mod. Phys. **57**, 287 (1985).

[31] B.L. Altshuler and A.G. Aronov, in *Electron-Electron Interaction in Disordered Systems*, edited by A.L. Efros and M. Pollak (Elsevier, New York, 1985), p. 1.

[32] B.J. Hickey, D. Greig, and M.A. Howson, J. Phys. F: Met. Phys. **16** (1986) L13;

[33] H.H. Boghosian, and M.A. Howson, Phys. Rev. B **41**, 7397 (1990).

[34] G. Stewart, Rev. Mod. Phys. **73**, 797 (2001).

CHAPTER 4

Physical properties of as-cast UPt_2Si_2

4.1 Introduction

UPt_2Si_2 belongs to the class of UT_2M_2 compounds, with T representing a transition metal and M elements of the periodic table groups III or IV (most commonly Si or Ge). The UT_2M_2 class of systems exhibits a wide range of exotic properties at low temperatures, such as:

- ferromagnetic ordering, e.g., in UCu_2Si_2 [1],
- antiferromagnetic ordering like in UCo_2Ge_2, UNi_2Ge_2, UCo_2Si_2, UPd_2Si_2, URu_2Si_2. For some of the compounds a ferromagnetic canting has been reported, e.g., for UPd_2Si_2 [1–3]. Particular attention has been paid to URu_2Si_2, for which at low temperatures antiferromagnetism was reported to coexist with some sort of "hidden order" phase and superconductivity [3–6].
- Pauli paramagnetism, e.g., in: URe_2Si_2, UOs_2Si_2 [3].

With this variance of ground state properties the UT_2M_2 compounds have been subject of very intensive studies for more than two decades now.

UT_2M_2 materials usually crystallize in one of two tetragonal structures: either the $CaBe_2Ge_2$ (*P4/nmm*) or $ThCr_2Si_2$ (*I4/mmm*) lattice (Fig. 4.1). Both are derivatives of the $BaAl_4$ structure and consist of layers Ca/Be/Ge or Th/Cr/Si, which are stacked along the *c* axis. The main difference between the two structures is the stacking sequence of the layers, which are

Ca - Be - Ge - Be - Ca - Ge - Be - Ge - Ca for $CaBe_2Ge_2$ or

Th - Si - Cr - Si - Th - Si - Cr - Si - Th for $ThCr_2Si_2$.

As a consequence of this stacking, the $CaBe_2Ge_2$ structure possesses a lower symmetry of the unit cell than the $ThCr_2Si_2$ lattice. Still, the $CaBe_2Ge_2$ and $ThCr_2Si_2$ structures are closely related, which can lead to structural

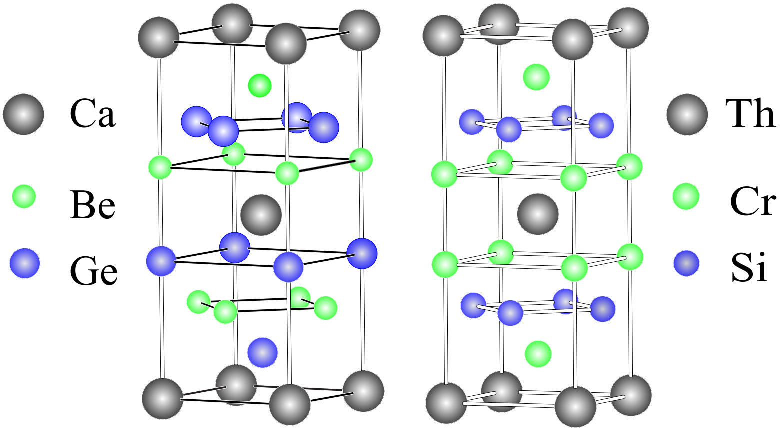

Figure 4.1: The tetragonal structure of $CaBe_2Ge_2$ (left) and $ThCr_2Si_2$ (right).

instabilities and, as has been observed for UCo_2Ge_2, even to a structural transition between this two structures [2]. Moreover, this type of a structural instability may result in crystallographic disorder. For instance, a recent study of URh_2Ge_2 supplied evidence for the presence of disorder on the nonmagnetic ligand sites. The moderate bond length disorder has been established in as–grown single crystals by the X–ray absorbtion fine-structure experiments [7]. It is assumed that this type of disorder is the result of $\sim\ 5-10\%$ Rh/Ge random sites exchange [8]. The disorder in as–grown single crystals generates a spin glass ground state below $T_f\ \sim 9$ K, and even controls the electronic transport properties [9]. The glassy electronic behavior in this crystalline compound reflects the enhancement of disorder effects as a consequence of the strong electronic correlations [10].

Generally, such “moderate” levels of disorder, *i.e.*, crystallographic randomness on the level of $\sim\ 10\%$, are very hard to determine experimentally. Hence, often the presence of disorder has gone unnoticed and its relevance for the physics has rarely been considered. Therefore, in order to study the influence of the crystallographic disorder on the physical properties of heavy fermion compounds, a model system is required. UPt_2Si_2 appears to be a

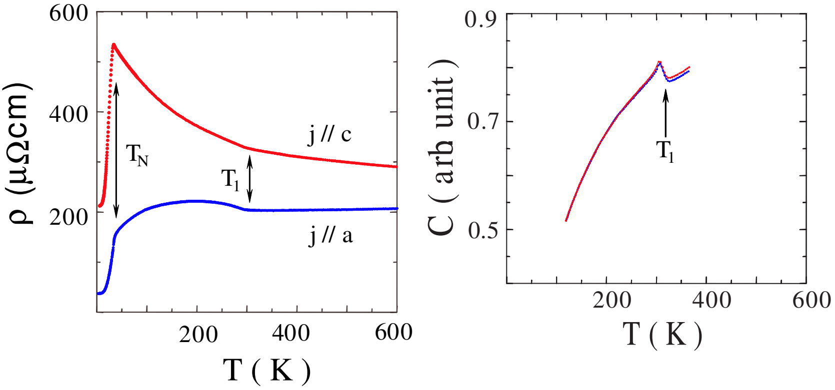

Figure 4.2: The temperature dependence of the electrical resistivity (left) ρ and specific heat C (right) of single crystalline annealed UPt_2Si_2 (after Amitsuka [14]).

suitable candidate. For this compound large single crystals can be grown. Furthermore, due to pronounced differences in the scattering cross sections of U, Pt and Si (U: 8.908 barn; Pt: 11.71 barn; Si: 2.167 barn) a detailed structural study by means of neutron scattering can be performed. The bright elemental contrast leads to a high resolution with respect to disorder effects.

UPt_2Si_2 crystallizes in the $CaBe_2Ge_2$ structure [11–13]. According to dc magnetic susceptibility measurements carried out by different groups on polycrystalline samples, an antiferromagnetic phase transition occurs at 37 K [12] or 36 K [3]. Steeman *et al.* [13], in a study on single crystalline UPt_2Si_2, have reported a value of $T_N = 35$ K, as derived from neutron diffraction, specific heat and resistivity measurements. Further, they observed a very unusual behavior in the electrical resistivity concerning the anisotropy between a and c axis. While at room temperature the c axis resistivity is only a factor two larger than along the a axis, in the residual resistivity there is a difference by a factor of 30.

Additionally, in a more recent study, Amitsuka [14] has reported the presence of an anomaly in the specific heat and electrical resistivity at $T_1 \sim 305$ K (Fig. 4.2). Similar anomalies have previously been observed as a result of a monoclinic or triclinic lattice deformation of the $CaBe_2Ge_2$ structure [15, 16]. This would suggest the presence of a first order structural phase transition in UPt_2Si_2 at T_1, although at this point there is no direct evidence for this scenario from structural studies.

In a system like UPt_2Si_2, with a melting point T_M well above 1000 K, a first order phase transition at a comparatively low temperature can possibly lead to frozen–in disorder. In consequence, as we are dealing with a heavy mass system, this will strongly influence the physical properties of the compound. As this has not been considered in previous investigations, we carried out a single crystal neutron diffraction analysis in order to study the crystallographic structure and the possible presence of disorder in as–cast UPt_2Si_2. As we discuss in the following section, the measurements supply evidence for static strain disorder on certain ligand sites in the compound. To assess the consequences of the crystallographic disorder for the physics of UPt_2Si_2 we extensively studied the magnetic and transport properties by means of specific heat, magnetic susceptibility, neutron diffraction, μSR, electrical resistivity, magnetoresistivity, and Hall effect measurements.

4.2 Metallurgy and the crystallographic study of as–cast UPt_2Si_2

For our study a single crystal UPt_2Si_2 has been grown by R.W.A. Hendrikx (Kamerlingh Onnes Laboratory, Leiden University) using a tri-arc Czochralski technique in high purity argon atmosphere [17]. The starting materials were U: 3N, Pt: 4N, and Si: 5N. The Laue–X–ray diffraction confirms the single crystallinity and proper orientation of the sample. Electron-micro probe analysis established the crystal to be single phase and of the correct 1:2:2 stoichiometry. Bars for the transport and thermodynamic measurements have been cut via spark erosion along the tetragonal a and c axes. The main part of the crystal ($5 \times 5 \times 5$ mm) has been used for the neutron scattering experiments.

Single crystal neutron diffraction studies have been performed at the Berlin Neutron Scattering Center (BENSC) of the Hahn–Meitner Institute. With our detailed neutron scattering study we utilize the very bright elemental contrast between U, Pt and Si. This way, in a structural investiga-

	x	y	z	U_{11}	U_{22}	U_{33}
U	1/4	1/4	0.7484(2)	0.45(4)	0.45(4)	0.08(4)
Pt(1)	1/4	1/4	0.3785(2)	0.10(3)	0.10(3)	0.28(4)
Pt(2)	3/4	1/4	0	1.86(5)	1.86(5)	0.14(4)
Si(1)	3/4	1/4	1/2	0.10(6)	0.10(6)	0.18(7)
Si(2)	1/4	1/4	0.1330(3)	0.94(8)	0.94(8)	0.29(8)
lattice parameters: $a = 4.1857$ Å; $c = 9.6301$ Å $R_{Bragg} = 6.6\%$						

Table 4.1: The result of a refinement for the single crystal neutron diffraction data on as–cast UPt$_2$Si$_2$ with the CaBe$_2$Ge$_2$ lattice (space group $P4/nmm$). Experiments have been carried out at 50 K.

tion we have a very much higher sensitivity to ligand disorder than by using X–ray diffraction.

In order to determine the crystallographic structure of our crystal we have carried out single crystal neutron scattering experiments at the E5 spectrometer at 50 K. For the refinement of the data we have left all parameters, including the site occupation, free. In full agreement with previous reports [11–13] we find that the system crystallizes in the CaBe$_2$Ge$_2$ lattice (space group $P4/nmm$). With respect to the site occupation, from our analysis we find as the best refinement solution a fully ordered lattice, *i.e.*, there is no evidence for random site exchange in this material within experimental error (±3%).

In Tab. 4.1 we summarize the result for a full refinement of our data. The established values of the lattice parameters match well the results reported for polycrystalline [11] and single crystalline [13] samples (see Tab. 4.2 and Tab. 4.3, respectively). However, among these values a considerable variation can be distinguish for the Si(2) site.

Furthermore, as has been shown in Tab. 4.1, the values for the displacement parameters U_{11} and U_{22} for the Pt(2) and Si(2) sites are extraordinarily large, if compared to the other sites in this lattice. For further illustration of this finding, in Fig. 4.3 we plot the crystallographic structure of UPt$_2$Si$_2$ in an ellipsoidal representation, with the ellipsoidal axes representing the values U_{ii}. Note that we do not plot the unit cell, but instead a cell shifted such that an uranium ion is positioned at the origin.

	x	y	z
U	1/4	1/4	0.755
Pt(1)	1/4	1/4	0.3809
Pt(2)	3/4	1/4	0
Si(1)	3/4	1/4	1/2
Si(2)	1/4	1/4	0.1405
lattice parameters: $a = 4.192$ Å; $c = 9.687$ Å			
$R_{Bragg} = 3.8\%$			

Table 4.2: The result of a crystal structure refinement parameter determine by neutron diffraction measurements for polycrystalline UPt_2Si_2 with the $CaBe_2Ge_2$ lattice (space group $P4/nmm$). Experiments have been carried out at 300 K, from Ref. [11].

	x	y	z
U	1/4	1/4	0.7477(5)
Pt(1)	1/4	1/4	0.3769(4)
Pt(2)	3/4	1/4	0
Si(1)	3/4	1/4	1/2
Si(2)	1/4	1/4	0.1270(12)
lattice parameters: $a = 4.1999(1)$ Å; $c = 9.6456(4)$ Å			
$R_{Bragg} = 5.62\%$			

Table 4.3: The result of a crystal structure refinement parameter determine by neutron diffraction measurements for polycrystalline UPt_2Si_2 with the $CaBe_2Ge_2$ lattice (space group $P4/nmm$). Experiments have been carried out at 4.2 K, from Ref. [13].

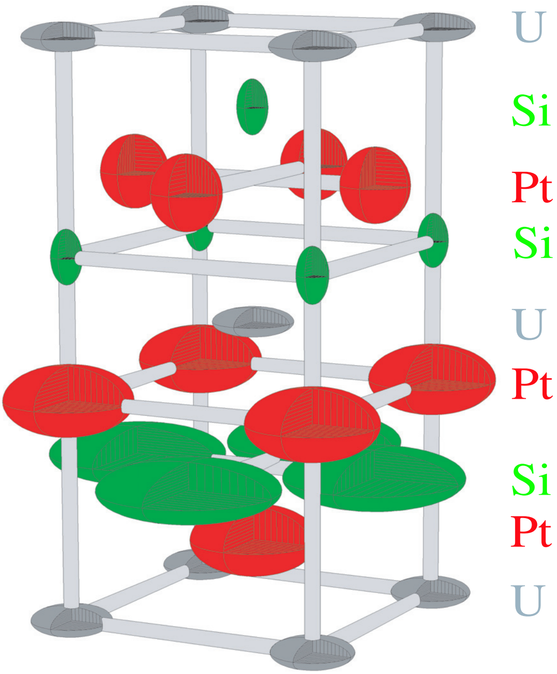

Figure 4.3: The crystallographic structure of UPt_2Si_2 in ellipsoidal representation. The cell has been shifted such that an uranium ion is positioned at the origin.

Since our experiments have been performed at a low temperature of 50 K, the large displacement parameters cannot be thermally induced. Instead, they reflect a static and random displacement of the Pt(2) and Si(2) ions within the tetragonal $a-b$ plane. Furthermore, the significant variation of the z value for Si(2) in the different studies, as discussed above, might mirror the sample to sample dependence present in the case of such a random displacement. Thus, we have established the presence of, for heavy fermion related materials, a new type of disorder in our compound, that is static strain disorder on the ligand sites.

4.3 Magnetic properties of as–cast UPt_2Si_2

The magnetic properties of single crystalline UPt_2Si_2 have previously been studied by susceptibility and neutron diffraction measurements [5, 13, 18]. The magnetic susceptibility χ shows a pronounced anisotropy. A Curie–Weiss fit to χ data in the temperature range from 200 to 300 K yields to an effective magnetic moment μ_{eff} of 2.87 μ_B/mole (3.39 μ_B/mole) and a Curie–Weiss temperature of -31 K (-98 K) for $B//a$ ($B//c$) [5]. At low temperatures an antiferromagnetic phase transition has been observed at $T_N = 35$ K.

Nieuwenhuys [18] proposed a description for the temperature dependence of the magnetic susceptibility based on a crystalline electric field model and within molecular field approximation. The molecular field approximation was used to account for the antiferromagnetic ordering at low temperatures. In this approach as a starting point served the model of singlet–singlet induced magnetic ordering by Wang and Cooper for rare–earth compounds [19]. The combination of ground state and first excited state is realized in case of uranium compounds for 4+ valency and $^3H_4$ spin-orbit ground state. Amoretti *et al.* [20,21] have shown that this model applies to uranium compounds, e.g., the magnetic properties of UX_2 (where X = P, As, Sb or Bi). Nieuwenhuys extended the model to five crystal fields levels with the ground state at 0 and excited states at: $\Delta_1 = 39$ K (singlet), $\Delta_2 = 56$ K (doublet) and $\Delta_3 = 84$ K (singlet). At $T = 0$, in the fully ordered state, the energy splitting between the ground state and the first excited state increases to 100 K. These calculations adequately describe the anisotropy and the absolute magnitude of the magnetic susceptibility of UPt_2Si_2. Only, the transition temperature value is slightly to high, which however is often observed in application of the molecular field approximation [19]. Furthermore, inelastic neutron scattering [22] verified the presence of crystal field excitations, and confirm the energy level scheme proposed in Ref. [18].

4.3.1 Specific heat and magnetization

As a starting point of this investigations on a single crystalline, as–cast UPt_2Si_2 compound served the specific heat study in a standard adiabatic heat–pulse technique. The measurements have been performed in zero magnetic field between 10 and 50 K. In Fig. 4.4 we plot the specific heat c_p and electronic specific heat coefficient c_p/T of UPt$_2$Si$_2$ as a function of temperature. Clearly, the antiferromagnetic transition is discernible slightly above 30 K. Closer inspection of the data reveals that the antiferromagnetic transition is comparatively broad. In order to determine more accurately the transition temperature we need to derive that part of the specific heat associated to the ordering transition as well as contributions from short range order. By assuming that the specific heat above the transition is entirely due to phonons and by parameterizing the data using Debye– and Einstein–contributions, with the first calculated *via* the full Debye-integral, we extract the relevant magnetic specific heat contribution $c_{p,mag}$. Taking into account the electronic contribution to the specific heat $\gamma = 32$ mJ/(mole K^2), with a Debye-mode for U ($\Theta_{D1} = 122$ K), for Pt ($\Theta_{D2} = 218$ K) and using an Einstein-contribution for Si ($\Theta_E = 491$ K), we can parameterize the specific heat not associated to (short or long range) magnetic ordering. With this procedure we neglect crystal field contributions to the specific heat, which however are not relevant for the determination of $c_{p,mag}$. By subtracting the parameterized nonmagnetic contribution to c_p from the data we obtain $c_{p,mag}$ depicted in Fig. 4.5.

Now, we can more accurately determine width and position of the antiferromagnetic phase transition. We estimate the transition temperature either from a linear extrapolation scheme for $c_{p,mag}(T)$ or from an entropy balance construction for $c_{p,mag}/T$ (Fig. 4.5) to $T_N = 32.9$ or 32.1 K, respectively, with the transition width of ~ 3 K (ranging from 31 to 34 K). This is a fairly broad temperature regime where we might expect to see short range correlation effects in local probe techniques.

Furthermore, we characterized as–cast UPt$_2$Si$_2$ with respect to its magnetic (ground state) properties by means of the susceptibility/magnetization measurements along the c and a axes. The overall behavior closely resembles that reported in the Ref. [5,18] (Fig. 4.6), with a pronounced anisotropy between both axes, and a cusp-like maximum corresponding to the antiferromagnetic phase transition. However, closer examination of the data reveals various new features.

As is shown in Fig. 4.7, the temperature dependence of the magnetic sus-

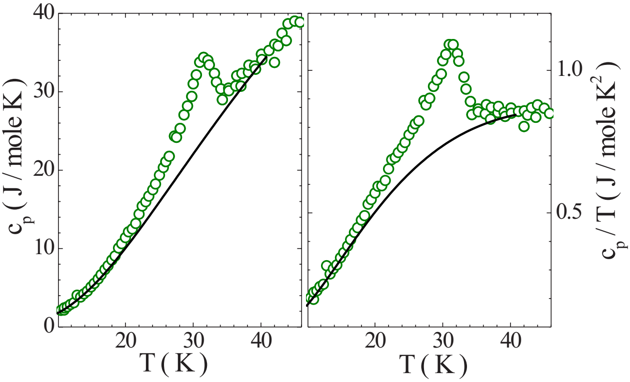

Figure 4.4: The temperature dependence of specific heat c$_p$ (left) and c$_p$/T (right) of UPt$_2$Si$_2$. The solid line represents the sum of lattice and electronic contributions to the specific heat.

ceptibility above T_N can not be described by a Curie–Weiss law in the high temperature range ($\sim$ 40–400 K). For both axes substantial deviations from a linear χ^{-1} dependence of T appear above 250 K. A proper description of χ^{-1} requires two linear fits with different fit parameters: for the temperature range from T_N to $\sim$ 250 K and above 250 K. We link this unusual behavior at high temperatures to the reported phase transition at 305 K (established for a different crystal) [14]. From a Curie–Weiss fit below 250 K,

$$\chi = \frac{C}{T - \Theta_{CW}} \tag{4.1}$$

with $C = N_A \mu_{eff}^2 / 3k_B$, Θ_{CW}: Curie–Weiss temperature, and μ_{eff}: effective moment in Bohr magnetons, for the measurement parallel the a (c) axis we determine μ_{eff} to 4.17 μ_B (3.09 μ_B) and Θ_{CW} to -116 K (-35 K). The values of the effective moment are higher than reported in previous studies and are not consistent with the values expected for the different uranium states. Especially, the results for the a axis are very unusual, as the estimated magnetic moment is much too large to be due to U ions only. Sim-

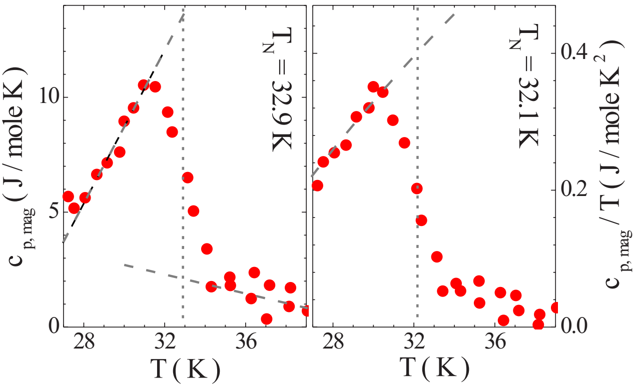

Figure 4.5: The magnetic part of the specific heat, $c_{p,mag}$ (left), and the magnetic electronic specific heat coefficient, $c_{p,mag}/T$ (right), of UPt$_2$Si$_2$ as a function of temperature. Dashed and dotted lines illustrate the constructions used to determine the antiferromagnetic transition temperatures.

ilarly, unexpectedly large effective magnetic moments have been found for UCo$_2$Ge$_2$ [2,23,24], UCo$_2$Si$_2$ [23] and UPd$_2$Al$_3$ [25]. In case of UCo$_2$Ge$_2$ the effective magnetic moment determined from the susceptibility data ranges from $\mu_{eff} = 4.0\mu_B$ [2] to $\mu_{eff} = 4.5\mu_B$ [23]. Here, these high values have been attributed to a superposition of U and Co paramagnetic moments [23] as well as the temperature independent Pauli paramagnetic contribution χ_P [2,23,24]. Because Pt usually is not associated with a localized magnetic moment, only Pauli contributions to the magnetic susceptibility will be considered in case of UPt$_2$Si$_2$. χ_p, in terms of the independent electron approximation, is given by

$$\chi_p = \mu_B^2 g(\varepsilon_F) \tag{4.2}$$

with $g(\varepsilon_F)$ as the density of levels at the Fermi energy [26]. In order to derive the Curie contribution, the temperature independent Pauli susceptibility of the conduction electrons is subtracted from the total susceptibility. Hence,

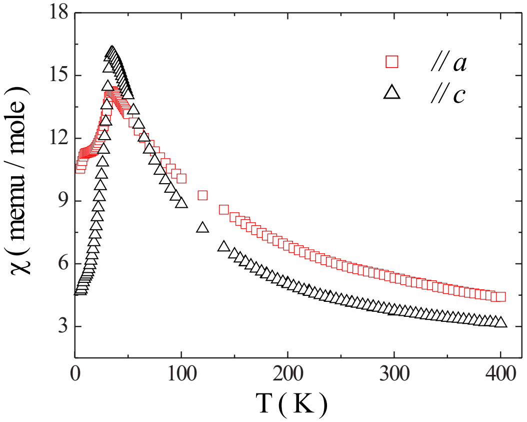

Figure 4.6: Temperature dependence of the magnetic susceptibility measured along both main crystallographic axes for as–cast single–crystalline UPt$_2$Si$_2$.

the Pauli susceptibility is determined via the electronic specific heat of the electron gas, which is defined as [26]

$$c_v = 1/3\pi^2 k_B^2 T g(\varepsilon_F). \tag{4.3}$$

This leads to

$$\chi_p = \mu_B^2 3\gamma/(\pi^2 k_B^2), \tag{4.4}$$

where $\gamma = c_v/T = 32$ mJ/(mole K^2) [13], yielding a Pauli susceptibility $\chi_p = 0.44$ memu/mole.

The $(\chi(T)$ - $\chi_p)^{-1}$ dependence for the a axis in the temperature range from 40 to 400 K is now well described by a linear function in T. The fit parameters are $C = 2.00$ mole/(emu K) and $\Theta_{CW} = -109$ K. The effective magnetic moment is derived to 4.00 μ_B, which still exceed the values for the uranium ion.

In contrast, subtraction the χ_p contribution from the susceptibility data of the c axis does not yield a dependence $(\chi(T)$ - $\chi_p)^{-1}$ linear in T over the full temperature range. Instead, a Curie–like behavior is observed in two temperature ranges, that is from T_N to 250 K and from 250 to 400 K. From

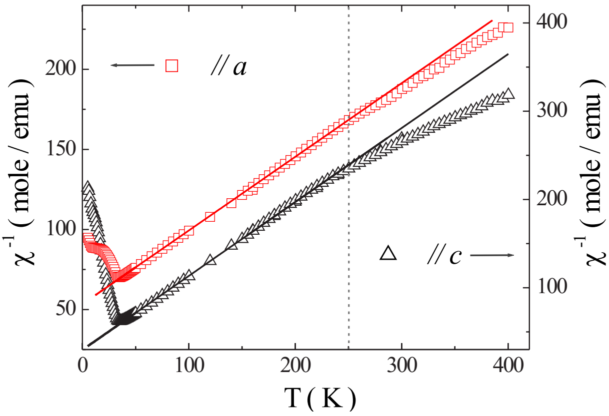

Figure 4.7: The inverse magnetic susceptibility χ *vs.* T for as–cast single–crystalline UPt$_2$Si$_2$. The solid lines denote Curie–Weiss fits with parameters given in the text.

the Curie–fit of the data below 250 K, we obtain $C = 1.04$ mole/(emu K), $\Theta_{CW} = -25$ K and $\mu_{eff} = 2.88\mu_B$. Above 250 K, the data are best described by a fit with $C = 1.41$ mole/(emu K), $\Theta_{CW} = -121$ K and $\mu_{eff} = 3.37\mu_B$. These results would imply that the phase transition significantly influences the magnetic susceptibility only along the c axis by changing the slope of $\chi^{-1}(T)$ at $T \sim 250$ K.

In conclusion, there is no clear explanation neither for the sample–to–sample dependence of the susceptibility, nor for the effective moment along the a axis being unusually large. Possibly, we might speculate that it indicates spin fluctuation affecting the susceptibility.

Another puzzling aspect is the very low value of the Curie–Weiss temperature for the a axis. Within mean field theory, we would expect that $|\Theta_{CW}| \sim T_N$. However, for the a axis $|\Theta_{CW}|$ is about four times larger than T_N. Usually, this would be taken as indication for magnetic frustration playing a role in the system.

At low temperatures an antiferromagnetic phase transition is discernible

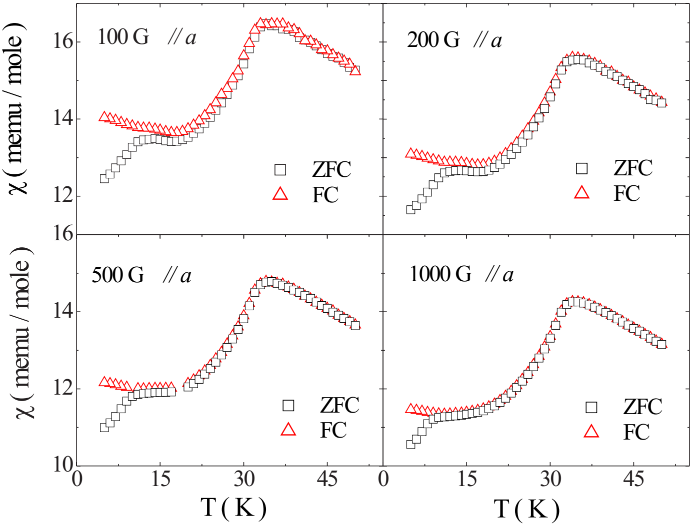

Figure 4.8: Magnetic susceptibility in a zero–field cooled and a field cooled experiment, with the magnetic field applied along the a axis.

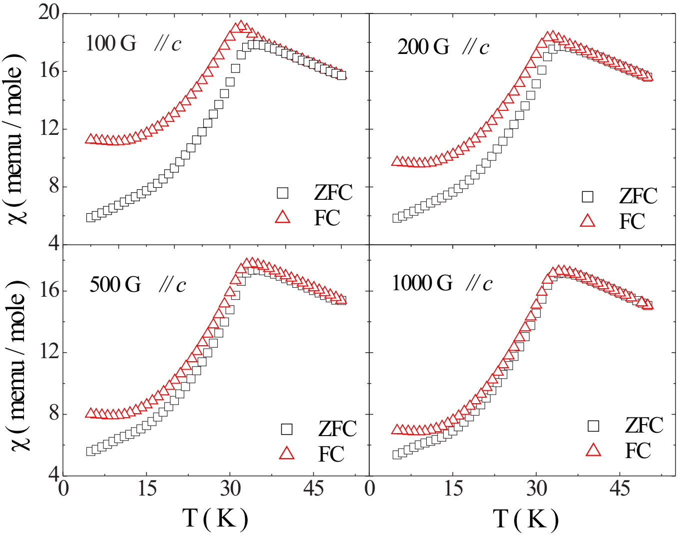

Figure 4.9: Magnetic susceptibility in a zero–field cooled and a field cooled experiment, with the magnetic field applied along the c axis.

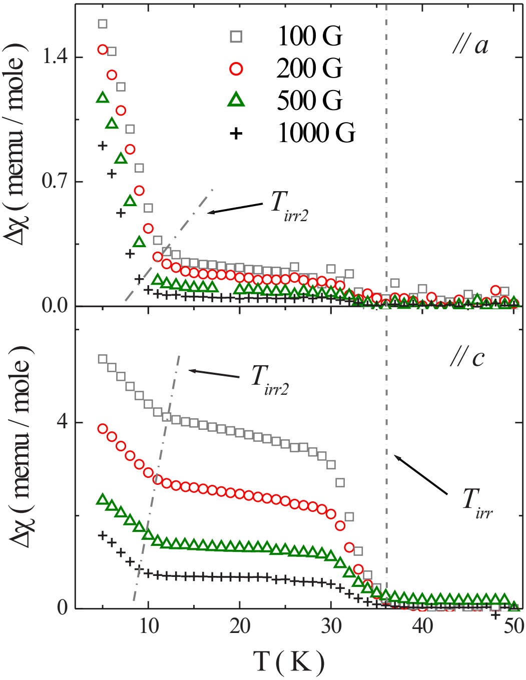

Figure 4.10: The difference in the magnetic susceptibility measured in field cooled (FC) and zero-field cooled (ZFC) experiments $\Delta\chi$ for both crystallographic directions and various magnetic fields.

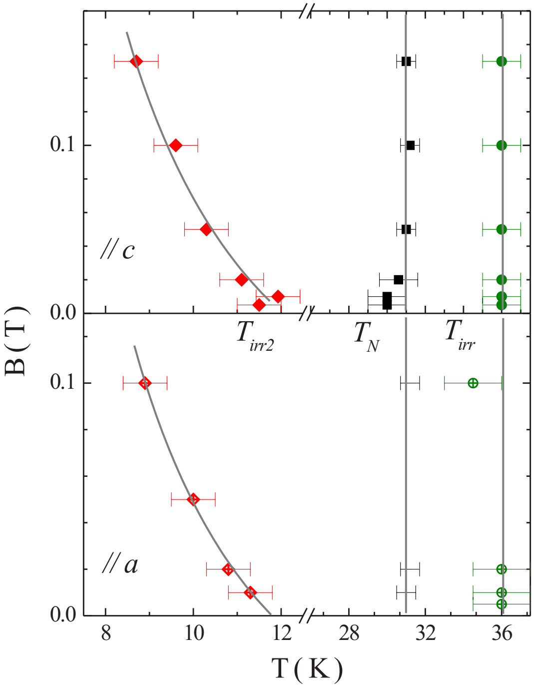

Figure 4.11: The magnetic phase diagram (T_{irr}, T_N, T_{irr2}) for the magnetic field applied along the a and c axis of as–cast UPt$_2$Si$_2$, as derived from the magnetic susceptibility. The lines are guides to the eye. For details see text.

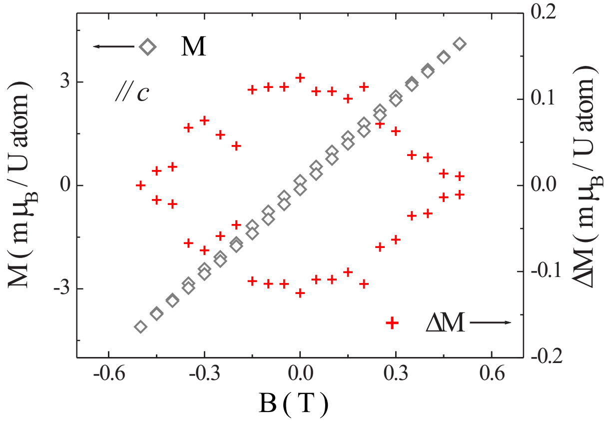

Figure 4.12: The magnetization loop M and the difference ΔM between the field down– and up–sweep at 5 K of as-cast UPt$_2$Si$_2$ for B // c axis.

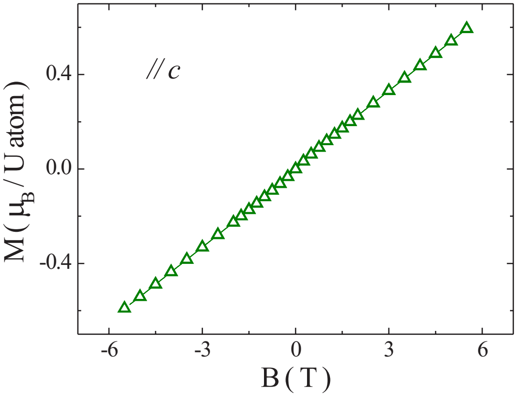

Figure 4.13: The magnetization values of as–cast UPt$_2$Si$_2$ measured along the c axis at 10 K in field down– and up–sweep, for B // c axis.

in UPt$_2$Si$_2$ for both crystallographic directions (Fig. 4.6). The transition temperature, which we derived from $d(\chi T)/dT$ = max is determined to $T_N = 31$ K. This value is significantly lower than that reported in Refs. [5,13], indicating a larger level of the crystallographic disorder of the present as–cast crystal, compared to the samples previously studied.

A detailed examination of the susceptibility below 50 K reveals the presence of magnetic hysteresis in of as–cast UPt$_2$Si$_2$. To study this behavior in detail, we performed measurements in zero–field cooled (ZFC) and field cooled (FC) mode, for magnetic fields ranging from 100 to 1000 G and applied along to two main crystallographic axes (Fig. 4.8 and 4.9). The observed magnetothermal irreversibility behavior is highly unusual. Along the a axis a small secondary maximum appears below T_N, at $T_{irr2} \sim 11.5$ K in the ZFC measurement in 100 G. The irreversibility temperature $T_{irr} = 36$ K, defined as the temperature below which a difference between the FC and ZFC susceptibility data appears, is even higher than T_N, and followed by a weak hysteresis down to T_{irr2}. In Fig. 4.10 we depicted $\Delta\chi = \chi_{FC} - \chi_{ZFC}$ as a function of temperature to quantify the irreversibility. Below T_{irr2}, $\Delta\chi$ grow very fast upon lowering the temperature.

Overall, the measurements along the c axis show very similar features. After the initial onset of irreversibility at $T_{irr} = 36$ K, $\Delta\chi$ grows linear with decreasing temperature down to $T_{irr2} \sim 11.5$ K in 100 G, where a change of slope occurs. However, no secondary maximum appears at T_{irr2} in the ZFC magnetic susceptibility (Fig. 4.9). In addition, in the temperature range $\sim$10 to 30 K, the magnitude of $\Delta\chi$ for the c axis is up to a factor 10 larger than along the a axis (Fig. 4.10).

Up to 0.15 T for both crystallographic axis, T_{irr} and T_N show no field dependence, as it is expected for a conventional antiferromagnet, with the energy scale set by an ordering temperature $\sim$ 30 K, an ordered moment of $\sim 2\ \mu_B$ and a critical field $\sim$ 40 T [27]. In contrast, T_{irr2} is shifted to lower temperatures with increasing magnetic fields, even in these comparatively small magnetic fields. In Fig. 4.11 we summarize the field dependence of T_N, T_{irr}, T_{irr2}, as obtained from the magnetic susceptibility.

The existence of a strong FC/ZFC hysteresis, for temperatures exceeding T_N, indicates the presence of small, well ordered regions in the crystals, in which antiferromagnetic (AFM) clusters form a cluster glass state. In an FC experiment and for the c axis, these clusters will be predominantly aligned along the field direction, while in a ZFC run they will point into random directions. Upon lowering the temperature below T_N, the AFM clusters will act as condensation cores for antiferromagnetic domains. Then, depending on if the clusters are randomly (in the ZFC case) or uniformly (in the FC) aligned, it will give rise to a large hysteresis between FC and ZFC run even in the antiferromagnetic case.

For the magnetic field applied parallel to the a axis the AFM clusters, in the FC mode measurements, will point perpendicular to B, with hardly any net alignment in the field direction. Correspondingly, magnetic FC/ZFC hysteresis will be much smaller in this case, as it has been observed in the experiments.

In addition to the results of the FC/ZFC susceptibility measurements, we find a small hysteresis in a magnetization loop taken at 5 K for $B//c$ axis (Fig. 4.12). In order to better visualize the effect in the figure we included the difference ΔM of the magnetization between field sweep down, M_d, sweep up M_u and the average magnetization, defined as $\Delta M = M_{d(u)} - (M_d + M_u)/2$. Hysteresis in the magnetization M vanishes for magnetic fields above $B \sim 0.5$ T, where all domains are aligned parallel to the external magnetic field. This existence of hysteresis is in full agreement with the results of the zero-field cooled and field cooled magnetic susceptibility measurements.

In contrast to the magnetization measurements at 5 K, at 10 K no hysteresis can be observed within experimental resolution, as depicted in Fig 4.13. M shows no anomaly or saturation in the magnetic field up to 5 T. This implies a difference in the AFM domain characteristic above and below T_{irr2}.

Another unusual feature has been found in magnetic relaxation measurements. The experiments have been carried out for $T = 5$ and 10 K, for both crystallographic directions. The samples have been cooled down in ZFC modus, subsequently a magnetic field of $B = 5$ T has been applied. After 60 s the magnetic field has been turned off using the “no overshoot” mode of the SQUID Quantum Design system. According to the SQUID manual a remanent magnetic field of about 20 to 40 G is expected, with the significant relaxation towards zero over several hours [28]. For example,

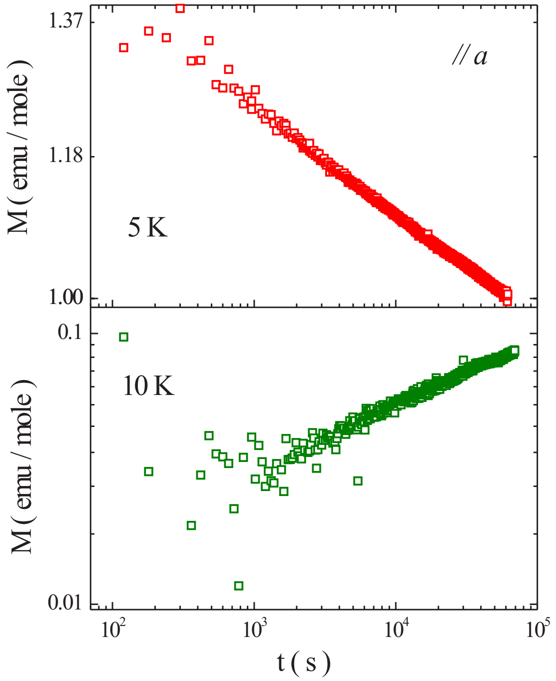

Figure 4.14: The time dependence of the remanent magnetization M of as–cast UPt$_2$Si$_2$ measured along the a axis, after lowering the field from 5 to 0 T.

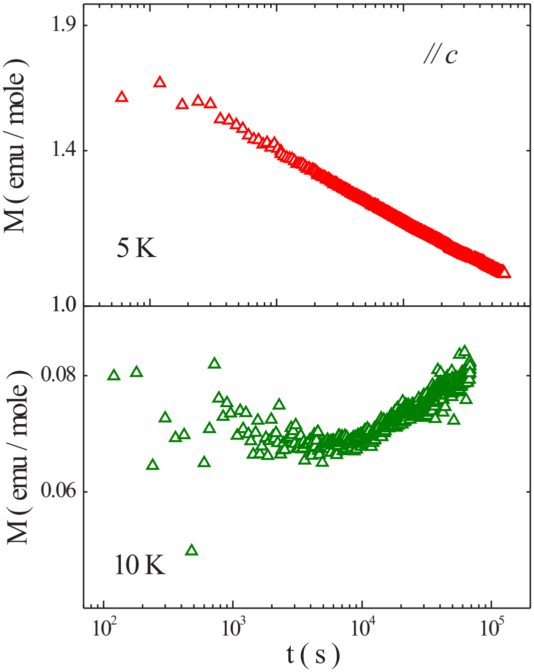

Figure 4.15: The time dependence of the remanent magnetization M of as–cast UPt_2Si_2 measured along the c axis, after lowering the field from 5 to 0 T.

after 24 hours the remanent field typically relaxes to about 20% of its value immediately after the discharge.

We observe significant differences in the magnetic relaxation measurements carried out at 5 and 10 K (Fig 4.14 and 4.15). The values of the remanent magnetization are much higher and the relaxation is much slower for the measurement at 5 K.

The relaxation behavior at 10 K for both crystallographic axes can be explained as resulting from the relaxation of the magnetic flux trapped in the superconducting magnet. Instead the data at 5 K, with the large residual magnetization, indicate that the relaxation arises from the sample itself. This difference in the relaxation behavior supports the indication that below T_{irr2} the system passes into some “modified” magnetic phase.

To better understand these low temperature properties, and particular, the nature of T_{irr2}, additional investigations of the magnetic structure by means of muon spin relaxation μSR and neutron scattering study have been performed.

4.3.2 Magnetic structure - μSR and neutron diffraction

μSR spectroscopy is based on the measurement of the time evolution of the spin polarization of a muon ensemble under the influence of local magnetic fields within the sample. It provides information about the temperature dependence of the sublattice magnetization and the magnetically ordered volume fraction. We carried out zero–field time–differential muon spin relaxation measurement at the *GPS* spectrometer of the Paul Scherrer Institute in Villingen, Switzerland, between 1.7 and 40 K, *i.e.*, in the temperature range where magnetic irreversibility has been found in the susceptibility measurements. The experiments and the data analysis have been performed in collaboration with H.-H. Klauss and A. Bosse.

The time dependence of the muon spin polarization $P_z(t)$ is determined from the count rates of two counters placed in opposite position using the corrected asymmetry method [29]. The asymmetry is described as $A(t) = A_0P_z(t)$. In Fig. 4.16 we present a set of representative zero–field μSR spectra for UPt_2Si_2, with $P_z(0)$ perpendicular to the c axis. At high temperatures ($\sim$ 40 K) we detected only a weak muon depolarization,

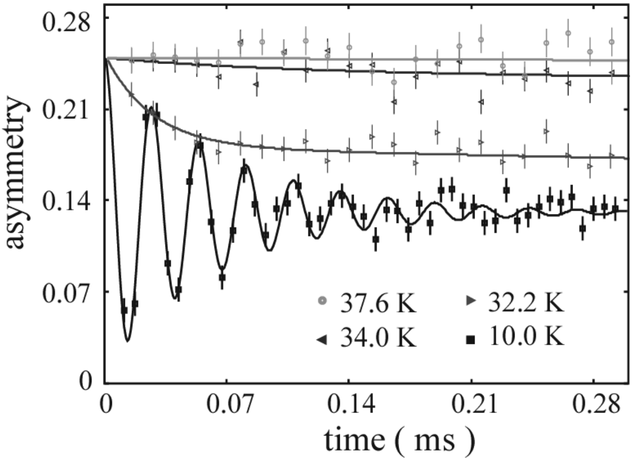

Figure 4.16: Typical zero–field μSR spectra of the as–cast UPt_2Si_2 sample, with P_z(t=0) perpendicular to the c axis.

proving the nonmagnetic state at this temperature. At the lowest temperatures, we observe a spontaneous muon spin precession, corresponding to static long range magnetic order. In the intermediate temperature range of $T_N < T < T_{irr}$ we find enhanced magnetic relaxation indicating the presence of static magnetic clusters.

The data were analyzed using:

$$A(t) = A_0(f_p cos(2\pi\nu t)e^{-\lambda_{trans}t} + (1-f_p)e^{-\lambda_{long}t}) \tag{4.5}$$

Here, f_p describes the signal fraction showing spontaneous muon spin precession with an average frequency of ν and relaxation rate λ_{trans}. λ_{long} describes the dynamic relaxation of the muon in an internal field parallel to $P_z(t=0)$.

In Fig. 4.17 we plot the temperature dependence of the spontaneous μ^+ frequency and the static relaxation rate, from which we estimate a T_N of 32 K. This value nicely corresponds to that obtained from the magnetic susceptibility measurements for the bulk transition temperature. However, even above T_N a part of the sample is magnetically ordered, as indicated in

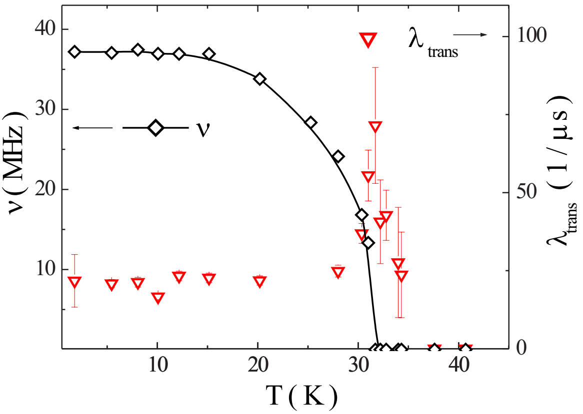

Figure 4.17: Temperature dependence of the spontaneous muon spin precession frequency ν and the static relaxation rate λ_{trans} for the as–cast UPt$_2$Si$_2$ sample, measured perpendicular to the c-axis.

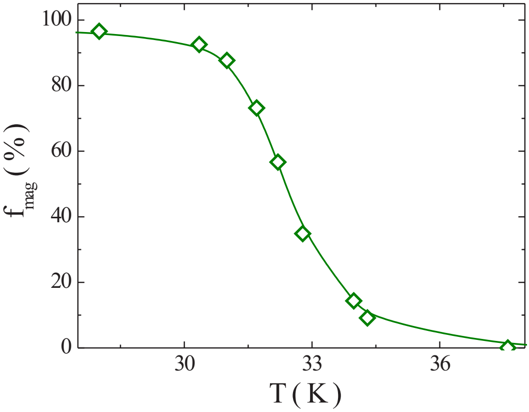

Figure 4.18: Temperature dependence of the magnetic volume fraction f_{mag} for the as–cast UPt_2Si_2 sample, measured perpendicular to the c-axis.

Fig. 4.18, where we plot the T dependence of the magnetic volume fraction f_{mag}. f_{mag} is given by:

$$f_{mag} = \frac{f_p(T)}{f_p(T = 1.7\ K)} \tag{4.6}$$

assuming a 100% ordered sample at $T = 1.7\ K$. From this figure we find the magnetic signal component to exist up to $T_{irr} \sim 36$ K, thus representing a clear indication for the presence of magnetic clusters caused by moderate frozen–in disorder in our sample. Surprisingly the μ^+ measurements do not reveal differences in the magnetic properties of the magnetic phases above and below T_{irr2}.

Furthermore we study the nature of the antiferromagnetically ordered state on a microscopic scale by means of neutron scattering experiments. The measurements have been carried out using the E1 spectrometer of the BENSC, with a neutron wave length of $\lambda = 2.42757$ Å. Fig. 4.19 depicts the temperature evolution of the q dependence of the [1 0 0] magnetic Bragg peak. We find additional Bragg intensity in the magnetically ordered phase

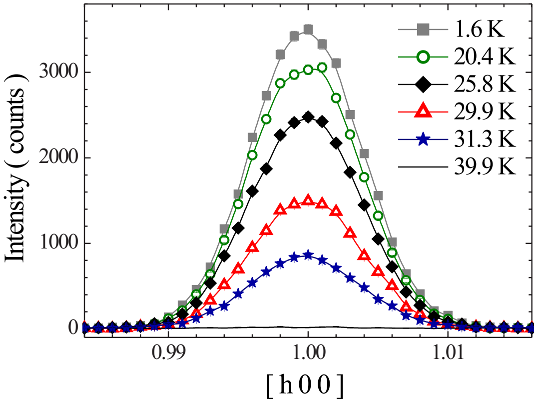

Figure 4.19: The q dependence of the [1 0 0] Bragg peak of as–cast UPt$_2$Si$_2$ for various temperatures. Lines are guides to the eye.

on the [1 0 2], [1 0 3] and [2 0 1] peaks. The appearance of magnetic Bragg intensity on these positions is fully consistent with the magnetic structure proposed in Ref. [13], consisting of magnetic moments pointing along the c direction, being ferromagnetically coupled within the $a-b$ plane, and with antiferromagnetic coupling on adjacent planes along the c axis.

In Fig. 4.20 we plot the temperature dependence of the integrated intensity of the [1 0 0] Bragg peak of UPt$_2$Si$_2$. The overall behavior is that expected for the sublattice magnetization of a common antiferromagnet, with a T_N somewhat above 30 K. By fitting the data between 28 and 31.5 K to a critical behavior $\mu_{ord} \propto (T_N - T)^{2\beta}$ we obtain a transition temperature $T_N = 32.1$ K for $\beta = 0.3$.

If we consider in more detail the transition region we find that there is substantial magnetic intensity present quite far above T_N, that is up to $\sim$ 34 K. This is illustrated in Fig. 4.21, where we enlarge the transition region from Fig. 4.20.

The magnetic intensity above T_N stems from magnetic clusters in a non-magnetic matrix. This information can be taken by considering both the

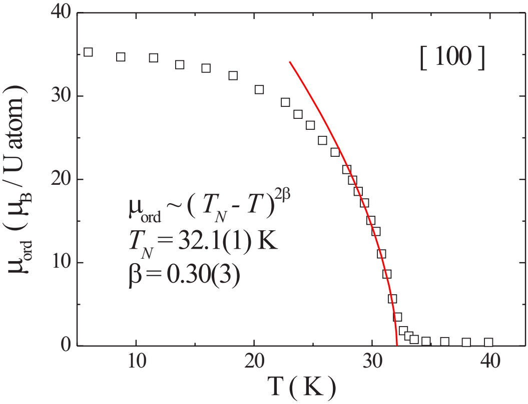

Figure 4.20: The temperature dependence of the integrated intensity of the [1 0 0] Bragg peak of as–cast UPt_2Si_2. The line indicates the result of a fit to the critical region, with parameters as indicated in the plot.

specific heat (Fig. 4.5) as well as the line width of the [1 0 0] peak. The latter, the temperature dependence of the line width of the [1 0 0] peak, fitted using an lorentzian expression:

$$I = I_0 \frac{W}{4(\Theta - \Theta_C)^2 + W^2} \tag{4.7}$$

(W: line width FWHM), we plot in Fig. 4.22. Up to T_N we observe a line width W, which is resolution limited. As soon as we exceed T_N the line width becomes broader, that is, not resolution limited anymore, corresponding to a finite magnetic correlation length. The largest line width that we observe (at ∼ 34 K) corresponds to a correlation length of about 130 Å.

Furthermore, for temperatures below T_{irr2} and all Bragg peaks we observed an intensity anomaly as depicted in Fig. 4.23. This anomaly, *viz.*, the reduction of the scattering intensity is most pronounced for the [1 0 3] peak, where most of the magnetic intensity vanishes. It is somewhat weaker for the [1 0 2] and [2 0 1] peaks, and also for the [1 0 0] reflection we see some small intensity decrease. Thus, it appears that the anomaly is more

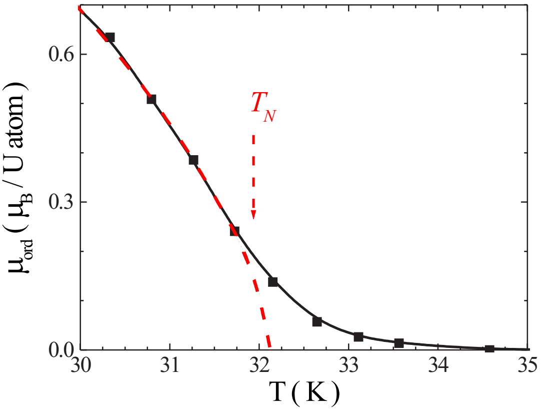

Figure 4.21: The temperature dependence of the integrated intensity of the [1 0 0] Bragg peak of as–cast UPt$_2$Si$_2$ close to T_N. The dashed line indicates the result of a fit to the critical region; for details see text.

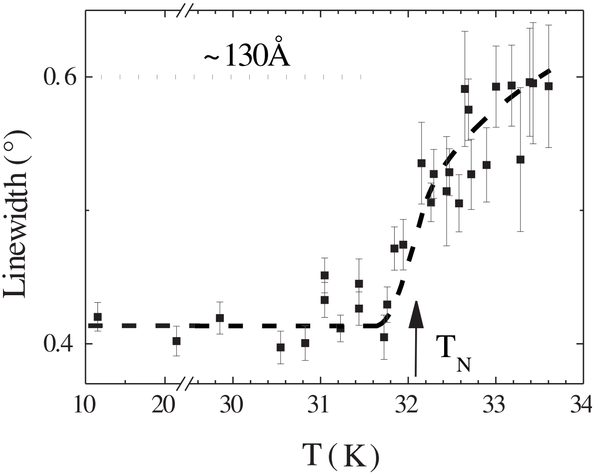

Figure 4.22: The temperature dependence of the line width for the [1 0 0] Bragg peak of as–cast UPt_2Si_2; for details see text.

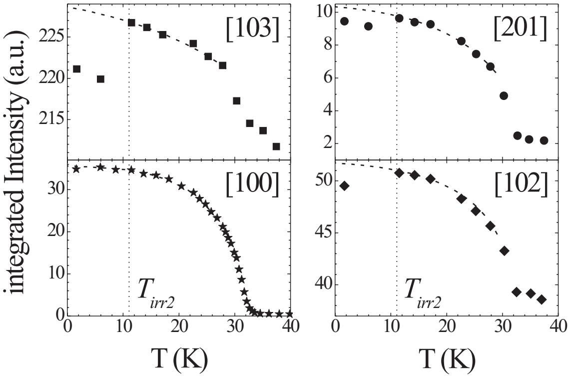

Figure 4.23: The temperature dependence of the integrated intensity of the magnetic Bragg peaks for as–cast UPt_2Si_2; for details see text.

pronounced for larger Bragg scattering angles.

At this point, we have not a full explanation for the intensity anomaly of the magnetic Bragg peaks. A first possible scenario is a reduction of the magnetic moment below T_{irr2}, which however is highly unlikely. Conversely, the apparent angular dependence indicates a change of the form factor at T_{irr2}. Such a behavior is also very unusual, and it is not clear why this should happen in UPt_2Si_2.

Instead, we tentatively attribute the anomaly to a modification of the symmetry of the magnetically ordered state. The intensity of the Bragg reflection does not completely vanish but only diminishes, which indicates that the magnetic structures above and below T_{irr2} are closely related. In this case the additional magnetic intensity for new Bragg peak positions would be expected below T_{irr2}. However, this additional intensity will be quite small and therefore hard to determine. In analogy to related compounds [30, 31], we speculate that a long–range modulation of the basic magnetic structure of UPt_2Si_2 possibly might explain the observed behavior. Certainly, the magnetic phase diagram of UPt_2Si_2 appears to be much richer than previously repotred.

4.4 Transport properties of as–cast UPt_2Si_2

The electronic transport of heavy fermions can be strongly affected even by a moderate level of structural disorder. For example, the transport properties of single crystalline URh_2Ge_2 with $\sim 5 - 10\%$ of random site exchange on nonmagnetic Rh/Ge places, closely resembles the behavior of metallic glasses. This is strong evidence for the enhancement of disorder effects in heavy fermion compounds, through from strong electronic correlations [9]. A significant influence of disorder on the transport properties has also been observed for UCu_4Pd. As it has been discussed in the previous chapter, upon annealing and an increase of crystallographic order, the residual resistivity changes drastically.

In this context, we have studied the electronic transport of as–cast UPt_2Si_2 along both crystallographic axes in the temperature range from 2 to 300 K.

The transport measurements have been carried out using a common four point ac technique. The measuring wires have been attached to the sample with silver paint, and the contact resistivity has always been keep below 1 Ω. The low power measurements have been carried out with a high sensitive resistance bridge (Linear Research LR–700). With the uncertainty about the geometry factor, absolute values of the resistivity are accurate to $\sim 5\%$.

4.4.1 Electrical resistivity

The electrical resistivity of UPt_2Si_2 is highly unusual. As depicted in Fig. 4.24, a large anisotropy is observed. The electrical resistivity measured along the a axis shows at high T a very weak temperature dependence. Initially, ρ increases with decreasing temperatures to $T \sim 150$ K. The shallow, broad maximum is attributed to the onset of coherence and crystalline electric field effects. For temperatures lower than $\sim$ 150 K, the electrical resistivity monotonically falls. Additionally, a steep drop of ρ is associated to the antiferromagnetic transition. At low temperatures the residual resistivity measured along the a axis is determined to $\rho_0 = 47\mu\Omega$cm. Overall, such metallic behavior is typical for heavy fermion antiferromagnets.

In contrast to the a axis, the resistivity measured along the c axis is much larger. After a broad minimum at $\sim$ 300 K, probably connected to the first order phase transition [14], ρ strongly increases down to T_N, where a maximum appears. Below T_N, like in the case of the a axis, the resistivity drops substantially and saturates at $\rho_0 = 345\mu\Omega$cm. This value is more than seven times larger than ρ_0 along the a axis, and even higher than the resistivity at 300 K for this crystallographic direction ($\rho_0 = 321\mu\Omega$cm), indicating a violation of Matthiesen's rule.

In order to highlight the stark difference in the transport behavior along a and c axis, we plot in Fig. 4.25 the temperature coefficient of the electrical resistivity $d\rho/dT$. For the a axis $d\rho/dT$ is positive below $\sim$ 150 K and has a maximum at T_N. For the c axis $d\rho/dT$ is negative down to $\sim$ 30 K, with a shallow minimum just at T_N, followed by a positive maximum at about 20 K. From the plots $d\rho/dT$ *vs.* T we determine T_N to 30 K for the a axis ($d\rho/dT =$ max) and 33 K for the c axis ($d\rho/dT =$ min).

The temperature dependence of $d\rho/dT$ corresponds for the a axis quite well to the predictions of Fisher and Langer for a system at a magnetic phase transition [32]. The model describes a system of magnetic ions with

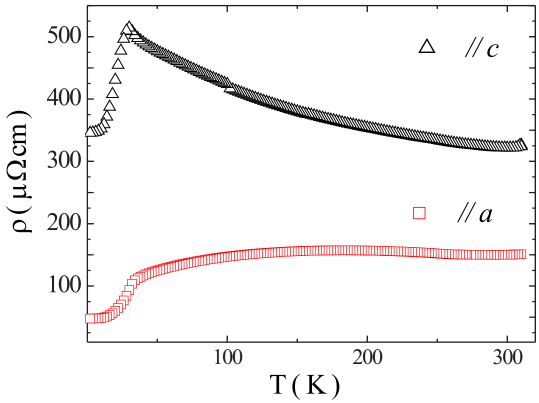

Figure 4.24: The temperature dependence of the electrical resistivity along the a and c axes for as–cast UPt$_2$Si$_2$.

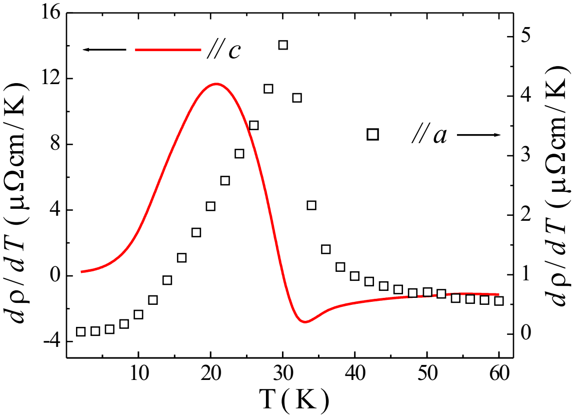

Figure 4.25: The temperature coefficient of the resistivity $d\rho/dT$ close to the magnetic phase transition for the a and c axes.

spins $\vec{S}_i$ placed at site $\vec{R}_i$ and a single band of conduction electrons. The interaction of the conduction electrons with the array of spins is given by

$$H_{elec-ion} = G\Sigma_i \delta(\vec{r} - \vec{R}_i)\vec{S}_i \bullet \vec{S}_e, \tag{4.8}$$

where $\vec{r}$ is the position of the electron and $\vec{S}_e$ the electron spin. Furthermore, it is assumed that close to the critical point spin fluctuations are sufficiently slow to neglect inelastic scattering of electrons, that is spin–flip scattering is ignored. The resistivity due to spin disorder scattering is given by

$$\rho = m/ne^2\tau \tag{4.9}$$

where n is the density of conduction electron, m represents the effective mass of the conduction electrons at the Fermi surface, and τ stands for the relaxation time associated with scattering from spin fluctuations and is connected to the static spin–spin correlation function $\Gamma(\vec{R}_i, T)$. Further, Fisher and Langer pointed out that a relation between $\vec{R}_i$ and the electronic mean free path l should be taken into account, as for $\vec{R}_i \gg l$ no coherent scattering can be expected. They proposed that $\Gamma(\vec{R})$ should be damped by a factor $p(\vec{R})$ which decreases monotonically from unity on a scale fixed by l. Assuming that τ is the relaxation time at a temperature sufficiently high so that the spin–spin correlations are negligible, they find that

$$\frac{\tau_0}{\tau} = \Sigma_{S=0}^{\infty} \nu_s f(R_S) p(R_S) \Gamma(R_S, T), \tag{4.10}$$

if R_s is the radius of the sth shell of spins surrounding the site $\vec{R}_i = 0$, ν_s represents the number of the spins in the shell, and $f(R_S)$ the decay oscillatory function.

Additionally, for any fixed R_S, $\Gamma(\vec{R}_s)$ has the same dominant singularity at T_c, as the magnetic energy, which for $T > T_c$ is given by

$$U(T) = -\Sigma_J J(R_j)\langle \vec{S}_0 \bullet \vec{S}_j \rangle = -\Sigma_{S=1} \nu_s J(R_S)\Gamma(R_S, T) \tag{4.11}$$

where $J(R)$ is the Heisenberg exchange energy.

The relations 4.10 and 4.11 posses the same temperature dependent factor $\Gamma(R_S, T)$. Therefore, ρ and $U(T)$ should have the same kind of singularity above T_c. In consequence, $d\rho/dT$ will behave as the magnetic specific heat c_p.

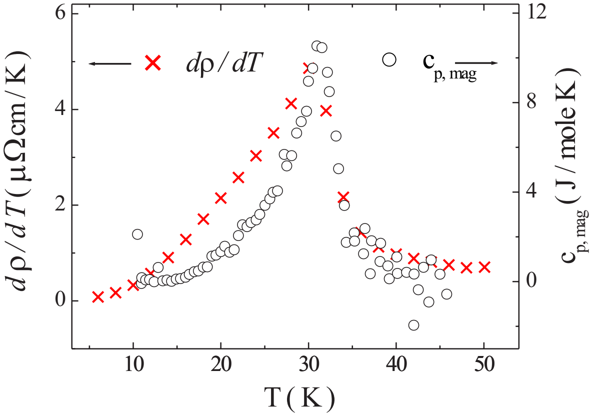

Figure 4.26: The temperature coefficient of the resistivity close to the antiferromagnetic phase transition for the a axis, compared to the magnetic specific heat.

Hence, we scaled the temperature coefficient of the resistivity for the a axis to the magnetic specific heat at low temperatures (Fig. 4.26). Close to and above T_N both quantities indeed follow the same temperature dependence. This implies that the dominant contribution to the magnetic resistivity near T_N along the a axis is due to short–range spin fluctuations.

Obviously, for the c axis data (see Fig. 4.25), for which at T_N the shallow minimum is observed, such a scaling does not apply. This illustrates that the resistivity for those two crystallographic directions is inherently different.

We have compared the resistivity measured for the a axis with calculations of the simplified Hessel Andersen model [33] carried out by Nieuwenhuys. Here, as a starting point serves the Born approximation, which allows to formulate the resistivity in terms of the imaginary part of the ion–ion susceptibility function. In contrast to the Hessel Andersen model, spin–spin correlations have not been considered. Hence the calculations account only for influence of the crystal fields effects on the electrical resistivity. The crystal field Hamiltonian for UPt$_2$Si$_2$ is written as (under the assumption

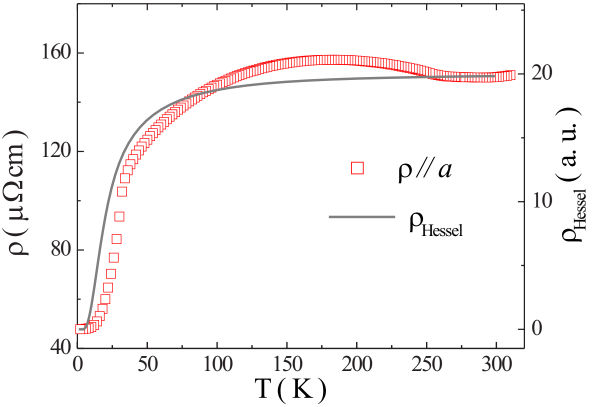

Figure 4.27: The temperature dependence of electrical resistivity for the a axis, compared to the electrical resistivity calculated using the Hessel Andersen model.

that the U ion is in a 4^+ state and has a $^3H_4$ spin ground state) [18, 20]

$$H_{CF} = B_2^0\hat{O}_2^0 + B_4^0\hat{O}_4^0 + B_4^4\hat{O}_4^4 + B_6^0\hat{O}_6^0 + B_6^4\hat{O}_6^4 \tag{4.12}$$

where $\hat{O}_i^k$ are the Stevens operators. For the determination of the eigenvalues of the Hamiltonian and the application of this crystal field model for the magnetization description of UPt_2Si_2 see Refs. [18, 20, 21].

The results of the calculations are presented at Fig. 4.27. In spite of the simplicity of the model, the calculated values describe the temperature dependence of the electrical resistivity for the a axis surprisingly well. The overall agreement regarding the essential energy scales illustrates the significant influence of the crystal fields on the electrical resistivity for the a axis. Conversely, the qualitatively different resistive behavior along the c axis does not arise from crystal field effects, thus emphasizing the inherent difference of ρ along the two crystallographic axes.

As has been previously mentioned, along both axes ρ drastically decreases below T_N. A closer inspection of the low temperature resistivity data (Fig. 4.28) reveals that this drop cannot be explained as a reduction of the resistivity in the coherent Fermi liquid ground state ($\rho = \rho_0 + AT^2$). Furthermore, ρ along the c axis exhibits a slight overshoot just below T_N. These features resemble the behavior of antiferromagnets with a gap in the spin–wave spectrum such as UNi_2Si_2 [34] or UNi_2Ge_2 [31]. For those systems the low temperature resistivity has been well described by a formula containing a term due to the spin-wave scattering:

$$\rho = \rho_0 + bT(1 + 2\frac{T}{\Delta})\exp(-\frac{\Delta}{T}) \tag{4.13}$$

where Δ is an energy gap in the spin–wave spectrum. In Fig. 4.28 the best fits to the data for $T < 20$ K are shown with $\rho = 48$ $\mu\Omega$cm (348 $\mu\Omega$cm), $b = 2.16$ $\mu\Omega$cm/K ($b = 5.88$ $\mu\Omega$cm/K), $\Delta = 39$ K (26 K) for $a(c)$ axis. The spin–wave scattering term well describes the data, which implies that this process mainly contributes to the low temperature resistivity of UPt_2Si_2.

4.4.2 Magnetoresistivity

In the next step of our study, we have investigated the magnetoresistivity of UPt_2Si_2 along the a and c axis, in order to assess the magnetic scattering contributions to the electrical resistivity. The magnetic field applied perpendicular to the current direction was swept from -5.5 to 5.5 T at constant temperature. Subsequently, we average the values of the magnetoresistivity measured at negative and positive magnetic fields.

Figs. 4.29 and 4.30 display representative data of the normalized magnetoresistivity defined as

$$\Delta\rho = \frac{\rho_B - \rho}{\rho} \tag{4.14}$$

for the a and c, axes respectively. Along both crystallographic axes $\Delta\rho$ is small and a monotonically varying function of the magnetic field. Further, from the data taken at 4 and 5.5 T we derive the temperature dependence (up to 50 K) of the normalized magnetoresistivity as depicted in in Fig. 4.31. Above 50 K $\Delta\rho$ is very low and tends to zero.

From high temperatures down to ~ 34 K along the a axis and to ~ 24 K for the c axis the magnetoresistance is negative. For these temperatures the field dependence of the magnetoresistivity is described by

$$\Delta\rho = \alpha B^2 \tag{4.15}$$

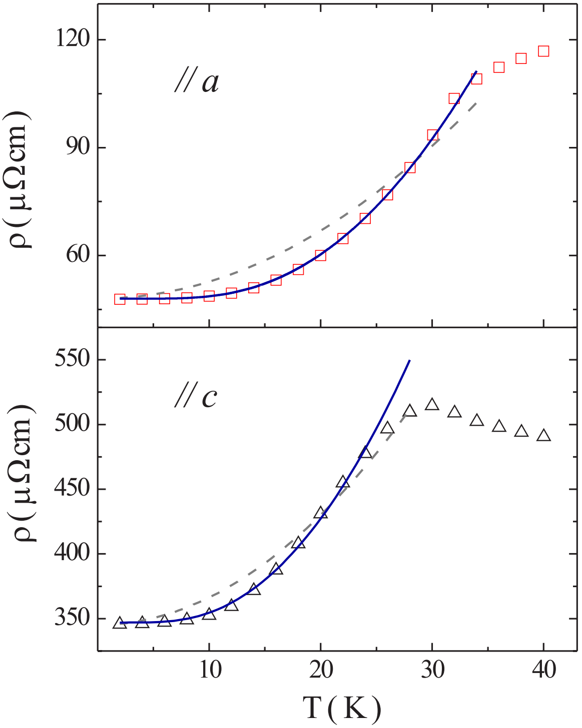

Figure 4.28: The temperature dependence of the electrical resistivity along the a and c axes for as–cast UPt_2Si_2. The dashed lines represent a T^2 dependence of ρ, solid lines are fits to the data using $\rho = \rho_0 + bT(1 + 2\frac{T}{\Delta})\exp(-\frac{\Delta}{T})$; for details see text.

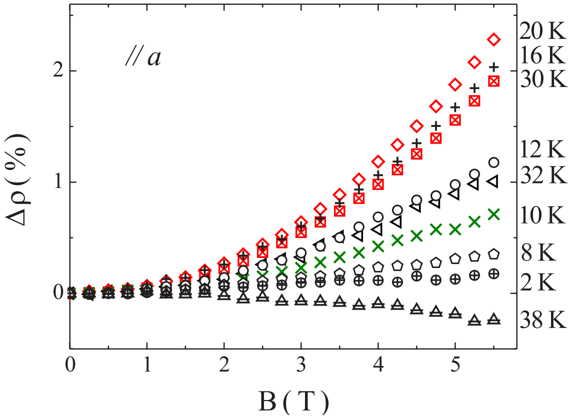

Figure 4.29: The field dependence of the normalized magnetoresistivity $\Delta\rho$ for selected temperatures measured along the a axis.

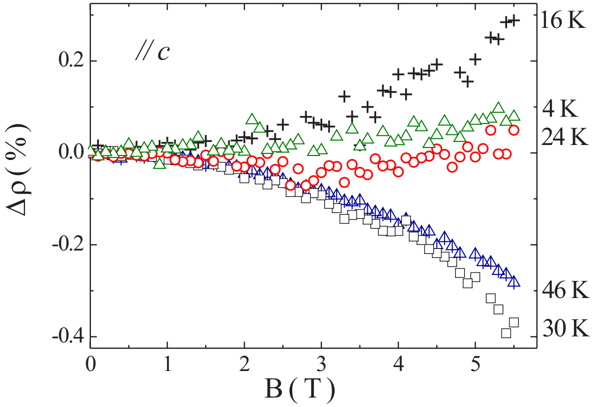

Figure 4.30: The field dependence of the normalized magnetoresistivity $\Delta\rho$ for selected temperatures measured along the c axis.

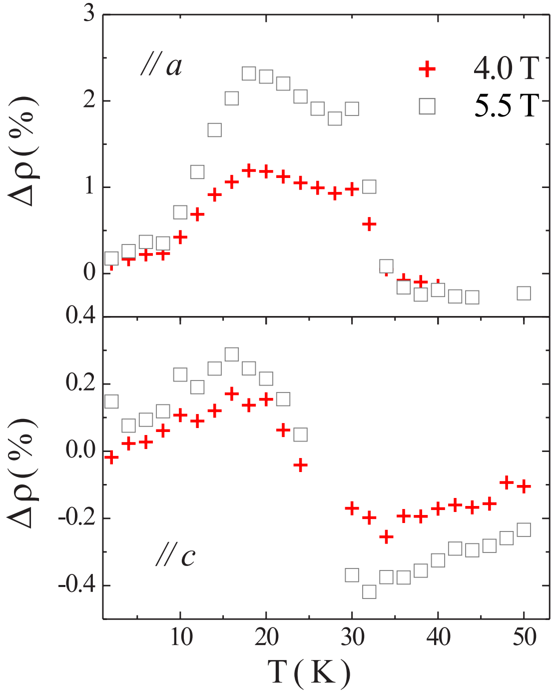

Figure 4.31: The temperature dependence of the normalized magnetoresistivity $\Delta\rho$ at 4 and 5.5 T measured for both principal crystallographic axes.

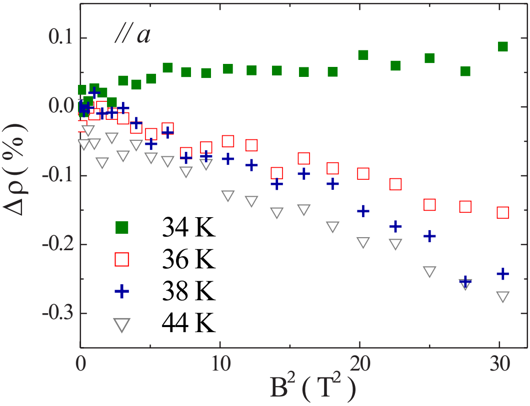

Figure 4.32: The normalized magnetoresistivity $\Delta\rho$ *vs.* the square of the magnetic field B^2 for the a axis and selected temperatures.

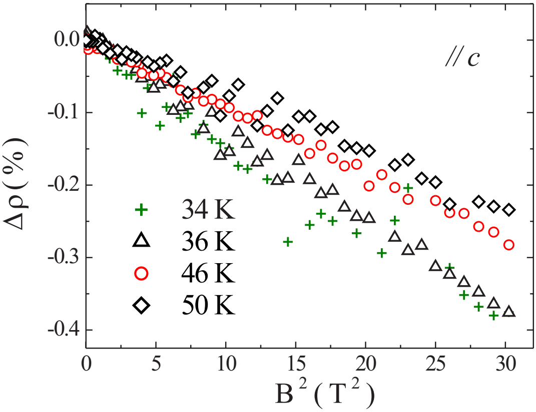

Figure 4.33: The normalized magnetoresistivity $\Delta\rho$ *vs.* the square of the magnetic field B^2 measured parallel to the c axis for selected temperatures.

with α as the magnetoresistive field coefficient.

Along the a axis for $T > 34$ K the very small values $\Delta\rho$ approach the experimental resolution limit for magnetic fields lower that 3 T (Fig. 4.32), which increases the error of the α parameter.

In the temperature range of negative magnetoresistivity $\alpha(T)$ does not follow $\chi(T)$. As has been depicted in Fig. 4.31, $|\alpha(T)|$ values decreases upon lowering the temperature unlike the magnetic susceptibility. It implies that scattering processes additional to spin disorder scattering affect the $\Delta\rho$.

The magnetoresistivity along the c axis in the temperature range from $\sim$ 30 to 50 K take a higher values and increases the resolution of α. As depicted in Fig. 4.33, $\Delta\rho$ is very well described by a square function of the magnetic field. The magnetoresistive coefficient α is closely correlated to the magnetic susceptibility, with (α - α_0) $\sim \chi$ (Fig. 4.34). This indicates spin disorder scattering as a dominant process which controls $\Delta\rho$ in this temperature range. A deviation from this behavior is observed below 35 K, where χ appears to decreased much faster than α. This correspond to the temperature of the antiferromagnetic cluster formation T_{irr} as derived from the magnetic susceptibility.

Furthermore, for the temperature range of a positive magnetoresistivity (*i.e.* in the antiferromagnetic state) the $\Delta\rho$ values for the c axis are up to a factor ten smaller than along the a axis (Fig. 4.31). This indicates that for the c axis there is a scattering component underlying the magnetic resistive part with almost no magnetoresistivity, and which we attribute to disorder induced localization, effects similar to the cases $\mathrm{URh_2Ge_2}$ or $\mathrm{UCu_4Pd}$.

Altogether, the rather complicated behavior of the magnetoresistivity for a and c axis with the change of sign from negative to positive for decreasing temperatures reflects the influence of additional effects such as the crystal fields, the field dependence of the antiferromagnetic state or a common metallic magnetoresistive component.

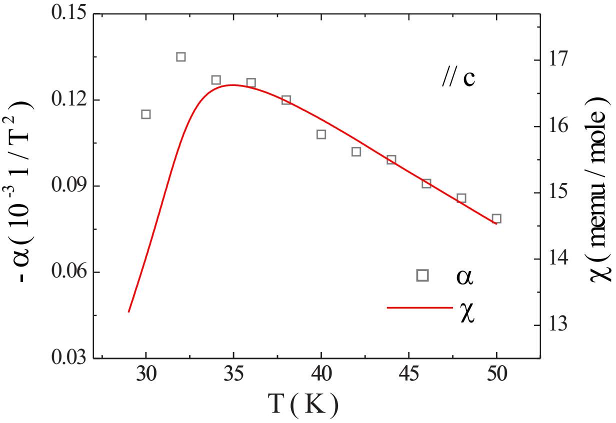

Figure 4.34: The temperature dependence of the fit coefficient α, from $\Delta\rho = \alpha B^2$, compared to the temperature dependence of magnetic susceptibility χ measured parallel to the c axis.

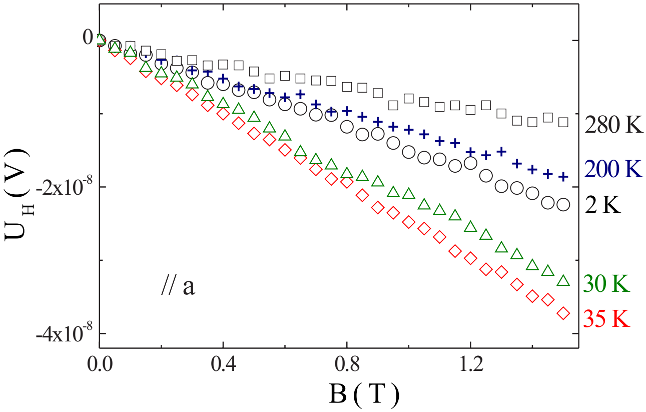

Figure 4.35: The magnetic field dependence of the Hall voltage $U_H = U_H(B)$ for as–cast UPt$_2$Si$_2$ measured along the a axis at selected temperatures.

4.4.3 Hall effect

The measurements of the Hall constant have been carried out to establish the carrier density of UPt$_2$Si$_2$, and in this way to determine if the inherently different resistive behavior along a and c axis can be traced back to a (pseudo) gap in the density of states on part of the Fermi surface.

We measured the Hall resistance U_H/I by sweeping the magnetic field from -1.5 to 1.5 T at constant temperature between 2 and 300 K. The Hall voltage U_H is a linear function of the magnetic field as shown in Figs. 4.35 and 4.36 (the depicted points represent an average of values measured for positive and negative magnetic fields),

$$\frac{U_H}{I} = \frac{R_H B}{d}, \tag{4.16}$$

where R_H is the Hall coefficient, and d–thickness of the sample. The electrical current I was kept constant at 10 mA. U_H is derived after substraction of the magnetoresistive component.

For both crystallographic directions R_H is strongly temperature depen-

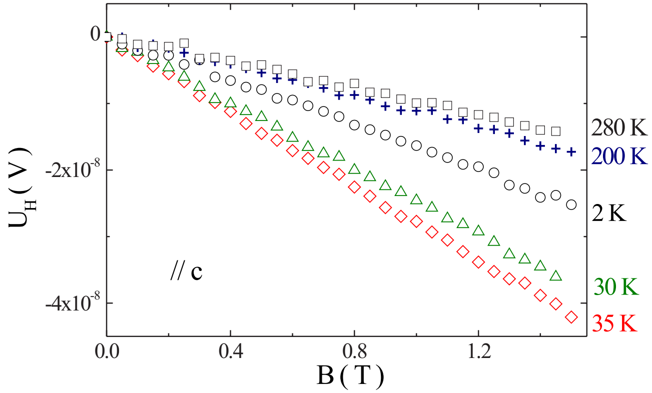

Figure 4.36: The magnetic field dependence of the Hall voltage $U_H = U_H(B)$, for as–cast UPt$_2$Si$_2$ measured along the c axis at selected temperatures.

dent and can be described as a sum of an ordinary Hall contribution R_0 and an anomalous temperature dependent term $R_A(T)$. As discussed in the previous chapter, there are three approaches to model $R_A(T)$ in heavy fermions:

- $R_A \sim \chi$ for $T > T_{coh}$ and $R_A \sim \rho^2$ for $T \ll T_{coh}$, where T_{coh} denotes the coherence temperature (model of Kontani and Yamada) [35],
- $R_A \sim \chi\rho_{mag}$, $T \gg T_{coh}$, with ρ_{mag} as magnetic scattering component. Below the coherence temperature the skew scattering is expected to vanish progressively, and $R_A(T)$ should drop to zero (model of Fert and Levy) [36]. We use for the scaling the total resistivity ρ, thus assuming that it approximates ρ_{mag}.
- $R_A \sim \chi\rho^2$ for disordered materials in which the side jump effect is a dominant contribution to $R_A(T)$ [37].

In Fig. 4.37 and 4.38 we depict the temperature dependence of the Hall constant $R_H(T)$ and the scaling of R_H data according to this three models.

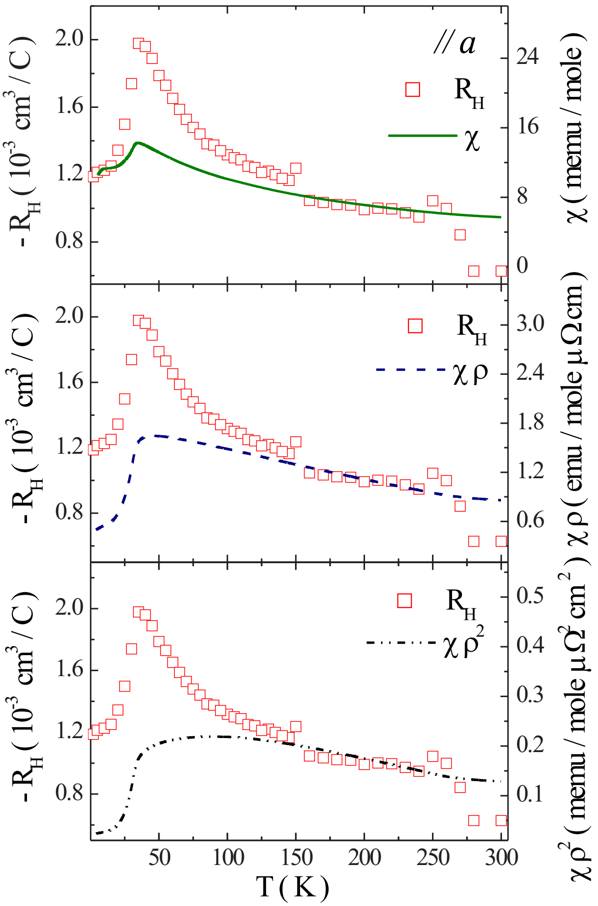

Figure 4.37: Temperature dependence of the Hall constant R_H of UPt$_2$Si$_2$ measured along the a axis. The temperature dependence of χ and products of $\chi\rho$ and $\chi\rho^2$ are included, for details see text.

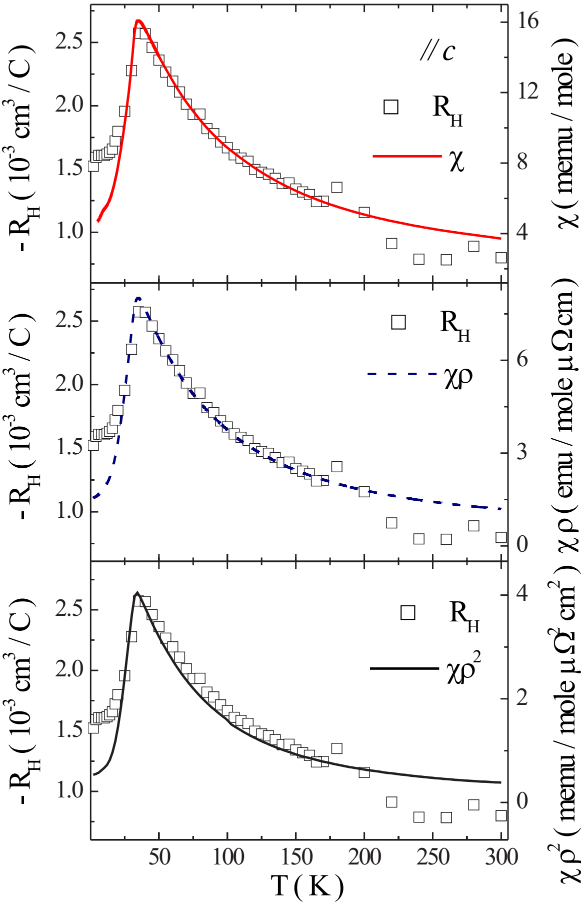

Figure 4.38: Temperature dependence of the Hall constant R_H of UPt$_2$Si$_2$ measured along the c axis. The temperature dependence of χ and products of $\chi\rho$ and $\chi\rho^2$ are included, for details see text.

For the a axis, starting from high temperatures, a large jump has been observed between 260 and 280 K, which might be connected to the first order phase transition reported at about 300 K [14]. Below this temperatures the Hall constant increases down to $\sim$ 40–35 K, where it reaches its maximum. Subsequently, $R_H(T)$ values fall quickly and approach -1.2$\times 10^{-3}$ cm^3/C. Non of the scaling models can fully account for $R_H(T)$. The closest correspondence can be observed between $R_H(T)$ and $\chi(T)$, although in a reduced temperature range from 260 to 160 K. The ordinary Hall contribution constant, derived from this scaling, is estimated to $R_0 \sim$ -0.6$\times 10^{-3}$ cm^3/C. According to this model we would also expect $R_H(T) \sim \rho^2$ for $T < T_{coh}$, in contrast to the experimental data. The coherence temperature of UPt_2Si_2, according to the resistivity measurement for the a axis, is placed in the temperature interval of 150–100 K.

The scaling according to model of Fert and Levy, which also could be applied to the $R_H(T)$ data in the temperature range from 260 to 160 K, leads to slightly worse agreement than for $\chi(T)$ scaling. Finally, the interpretation of the data within the framework of the side jump effect seems to be fully inadequate (Fig. 4.37).

In contrast to the a axis, for the c axis all proposed model can be applied for the description of $R_H(T)$ between 25–200 K. The scaling at high temperatures is disturbed by a jump in the $R_H(T)$ data, probably connected to the first order phase transition. With respect to the a axis it is shifted towards lower T to 240–200 K. Depending on the scaling model, the ordinary Hall contribution is found to be of the order of -0.5 and -0.8 $\times 10^{-3}$ cm^3/C, which leads to the carrier densities of the order of 1 to 2 electrons per unit cell.

In conclusion, although the simple analysis of $R_H(T)$ in scope of models proposed for heavy fermion compound does not allow for the exact estimation of $R_A(T)$ and with it R_0 for the whole temperature range and both crystallographic directions, it allow to state negative R_0 and disproves the possibility for a gap in the density of states.

4.5 Conclusions

We carried out an the extensive study on the structural, magnetic and transport properties of as–cast single crystalline UPt_2Si_2. The neutron diffraction study on this compound reveals the presence of crystallographic disorder on the non–magnetic Si(2) and Pt(2) sites.

With respect to previous investigations [13] we observe a suppression of the antiferromagnetic phase transition temperature T_N to $\sim 31\ K$. Furthermore, two irreversibility temperatures T_{irr} and T_{irr2} appear in the magnetic susceptibility, magnetization and neutron diffraction study. With respect to disorder, the two irreversibility temperatures reflect quite different aspects. The upper temperature, T_{irr}, is the result of the very strong dependence of the relevant energy scales on the local magnetic coupling strength J. For instance, in a Doniach like picture magnetic ordering results out of a competition between Kondo effect (energy scale Kondo temperature $T_K \propto \exp(-1/\mid JN(E_F)\mid))$ and RKKY exchange (energy scale $T_{RKKY} \propto J^2 N(E_F)$). UPt_2Si_2 is in the localized limit of comparatively small J values, as the RKKY-exchange wins and the system undergoes a magnetic transition at T_N. However, with the local variation of T_K and T_{RKKY} resulting from a distribution of J values, locally there are magnetically stronger coupled regions. This gives rise to the inhomogeneous cluster state between T_N and T_{irr}. Therefore, T_{irr} directly reflects the disorder induced variation of J.

In contrast, T_{irr2} rather marks the temperature below which a modulation of the magnetically ordered structure occurs, which become visible in the susceptibility/ magnetization study only because of the presence of the pinning centers affecting the antiferromagnetic domain behavior.

Furthermore, in the study of the electrical resistivity we observe quantitatively a similar behavior as reported previously [13]. However, below T_N ρ decreases slower, leading to a much higher residual resistivity for the present studied samples. This implies stronger disorder effects, corresponding to a lower crystal quality of the samples investigated in this work. The low temperature resistivity measured along both crystallographic axes strongly resembles the behavior of the antiferromagnets with a gap in the spin wave spectrum. We observed an anomalous, strongly temperature dependent Hall resistance, which cannot be fully explained within models usually applied for heavy fermions. Altogether, our study indicates that the resistive behavior is qualitatively different along the both principal crystallographic axes. While along the a axis it corresponds to typical heavy fermion behavior, along the c axis it is disorder dominated.

Bibliography

[1] L. Chelmicki, J. Leciejewicz, and A. Zygmunt, J. Phys. Chem. Solids **46**, 529 (1985).

[2] T. Endstra, G.J. Nieuwenhuys, A.A. Menovsky, and J.A. Mydosh, J. Appl. Phys. **69**, 4816 (1991).

[3] T.T.M. Palstra, A.A. Menovsky, G.J. Nieuwenhuys, and J.A. Mydosh, J. Magn. Magn. Mater. **54-57**, 435 (1986).

[4] T.T.M. Palstra, A.A. Menovsky, J. van den Berg, A.J. Dirkmaat, P.H. Kes, G.J. Niewenhuys, and J.A. Mydosh, Phys. Rev. Lett. **55**, 2727 (1985).

[5] T.T.M. Palstra, Ph.D. Thesis, (1986), unpublished.

[6] C. Broholm, J.K. Kjems, W.J.L. Buyers, P. Matthews, T.T.M. Palstra, A.A. Menovsky, and J.A. Mydosh, Phys. Rev. Lett. **58**, 1467 (1987).

[7] C.H. Booth, S.-W. Han, S. Süllow, and J.A. Mydosh J. Magn. Magn. Mater. **272**, 941 (2004).

[8] C.H. Booth, R. Feyerherm, and S. Süllow, to be published.

[9] S. Süllow, I. Maksimov, A. Otop, F.J. Litterst, A. Perucchi, L. Degiorgi, and J.A. Mydosh, Phys. Rev. Lett. **93**, 266602 (2004).

[10] K.I. Wysokinski, Phys. Rev. B **60**, 16376 (1999).

[11] H. Ptasiewicz-Bak, J. Leciejewicz, and A. Zygmunt, Solid State Comun. **55**, 601 (1985).

[12] K. Hiebl, and P. Rogl, J. Magn. Magn. Mater. **50**, 39 (1985).

[13] R.A. Steeman, E. Frikkee, S.A.M. Mentink, A.A. Menovsky, G.J. Nieuwenhuys, and J.A. Mydosh, J. Phys.: Condens. Matter **2**, 4059 (1990).

[14] H. Amitsuka, private communication (2002).

[15] G. Venturini, B. Malaman, and B. Roques, J. Less Common Metals **146**, 271 (1989).

[16] T. Takabatake, T. Tanaka, Y. Bando, H. Fujii, N. Takeda, M. Ishikawa and I. Oguro, Physica B **230-232**, 223 (1997).

[17] A.A. Menovsky, and J.J.M. Franse, J. Cryst. Growth **65**, 286 (1983).

[18] G.J. Nieuwenhuys, Phys. Rev. B **35**, 5260 (1987).

[19] Y.-L. Wang, and B.L. Cooper, Phys. Rev. **185**, 696 (1969).

[20] G. Amoretti, A. Blaise, and J. Mulak, J. Magn. Magn. Mater. **42**, 65 (1984).

[21] G. Amoretti, A. Blaise, R.O.A. Hall, M.J. Mortimer, and R. Troc, J. Magn. Magn. Mater. **53**, 299 (1986).

[22] R.A. Steeman, E. Frikkee, C. van Dijk, G.J. Nieuwenhuys, and A.A. Menovksy, J. Magn. Magn. Mat. **76-77**, 435 (1988).

[23] M. Kuznietz, H. Pinto, H. Ettedgui, and M. Melamud, Phys. Rev. B **40**, 7328 (1989).

[24] A.J. Dirkmaat, T. Endstra, E.A. Knetsch, A.A. Menovsky, G.J. Nieuwenhuys, and J.A. Mydosh, J. Magn. Magn. Mater. **84**, 143 (1990).

[25] V.S. Zapf, R.P. Dickey, E.J. Freeman, C. Sirvent, and M.B. Maple, Phys. Rev. B **65**, 024437 (2001).

[26] N.W. Ashcroft, and N.D. Mermin, *Solid State Physics*, Saunders College Publishing, New York (1976).

[27] H. Amitsuka, T. Sakakibara, K. Sugiyama, T. Ikeda, Y. Miyako, M. Date, and A. Yamagishi, Physica B **177**, 173 (1992).

[28] Quantum Design, MPMS Application Note 1014-208, http://www.qdusa.com/ resources/ techdocs.html.

[29] D. Baabe, M. Hillberg, F.J. Litterst, P. Adelmann, and H.-H. Klauss, Phys. Rev. B **69** 134512 (2004).

[30] H. Lin, L. Rebelsky, M.F. Collins, J.D. Garrett, and W.J.L. Buyers, Phys. Rev. B **43**, 13232 (1991).

[31] Y.B. Ning, J.D. Garret, C.V. Stager, and W.R. Datars, Phys. Rev. B **46**, 8201 (1992).

[32] M.E. Fisher, and J.S. Langer, Phys. Rev. Lett. **20**, 665 (1968).

[33] N. Hessel Andersen, J. Jensen, H. Smith, and O. Splittorff, Phys. Rev. B **21**, 189 (1980).

[34] Y.B. Ning, J.D. Garret, and W.R. Datars, Phys. Rev. B **42**, 8780 (1990).

[35] H. Kontani, and K. Yamada, J. Phys. Soc. Jpn. **63**, 2627 (1994).

[36] A. Fert, and P.M. Levy, Phys. Rev. B **36**, 1907 (1987).

[37] L. Berger, Phys. Rev. B **2**, 4559 (1970).

Chapter 5

Physical properties of annealed UPt_2Si_2

5.1 Introduction

The study on as–cast UPt_2Si_2 presented in the previous chapter reveals the presence of a moderate level of crystallographic disorder even in single crystalline material, which has a significant influence on the magnetic and transport properties of this compound. In this context, a very interesting issue is if or to which degree a small change of the disorder level will be mirrored in the physical properties of this material. The commonly applied method to improve crystalline quality is by means of annealing, and which we therefore used in this investigation.

Hence, the samples previously studied in the as–cast state, have been annealed for one week at a temperature of $T = 900$°C. Subsequently, a basic characterization of the physical properties by means of measurements of the structural, magnetic and transport properties, as previously carried out for the as–cast samples, has been repeated for the annealed samples along both crystallographic axes. Single crystal neutron diffraction studies have been performed at the Berlin Neutron Scattering Center (BENSC) of the Hahn-Meitner Institute. The magnetization and the dc susceptibility measurements have been carried out in a commercial SQUID magnetometer. The resistivity has been measured using a common four point ac technique. The measuring wires have been attached to the sample with silver paint, and the contact resistivity has always been kept below 1 Ω. For the low power resistivity measurements we used a high sensitive Linear Research LR-700 resistance bridge. With the uncertainty about the geometry factor of the samples, absolute values of the resistivity are accurate to within $\sim 5\%$. All these results we discuss in comparison to the findings for the samples prior the heat treatment.

	x	y	z	U_{11}	U_{22}	U_{33}
U	1/4	1/4	0.7480(2)	0.66(5)	0.66(5)	0.26(7)
Pt(1)	1/4	1/4	0.3787(2)	0.25(5)	0.25(5)	0.39(6)
Pt(2)	3/4	1/4	0	1.98(6)	1.98(6)	0.30(5)
Si(1)	3/4	1/4	1/2	0.16(7)	0.16(7)	0.38(9)
Si(2)	1/4	1/4	0.1340(4)	1.27(10)	1.27(10)	0.42(1)
lattice parameters: $a = 4.1857$ Å; $c = 9.6301$ Å						
						$R_{Bragg} = 6.6\%$

Table 5.1: The result of a refinement for the single crystal neutron diffraction data on annealed UPt_2Si_2, with the $CaBe_2Ge_2$ lattice (space group $P4/nmm$). The experiments have been carried out at 50 K.

5.2 Crystallographic properties of annealed UPt_2Si_2

Analogously to the experiments on the as–cast sample, and using the same BENSC spectrometer E5, single crystal neutron diffraction studies have been performed at 50 K, to reduce the influence of thermally induced atomic oscillations on the structural parameters. We summarize the result of a full refinement of our data in Tab. 5.1. The values of the lattice parameters fully correspond to the results obtained for the as–cast sample and in previous studies [1,2]. Furthermore, these measurements reveal that with respect to the strain disorder, as detected for the as–cast sample in the displacement parameters of the Pt(2)/Si(2) sites, annealing does not significantly change these values. Hence, with respect to the level of crystallographic disorder, our structural probe is not sensitive enough to quantify the improvement of crystalline quality.

5.3 Magnetic properties of annealed UPt_2Si_2

Furthermore, we have studied the magnetic properties in annealed UPt_2Si_2 by neutron scattering experiments. The measurements have been carried out using the BENSC E1 spectrometer. Here, for the annealed sample magnetic scattering intensity is already observed below $T = 36$ K. The temperature dependence of the integrated intensity of the [1 0 0] Bragg peak is presented in Fig. 5.1. It corresponds to the behavior expected for

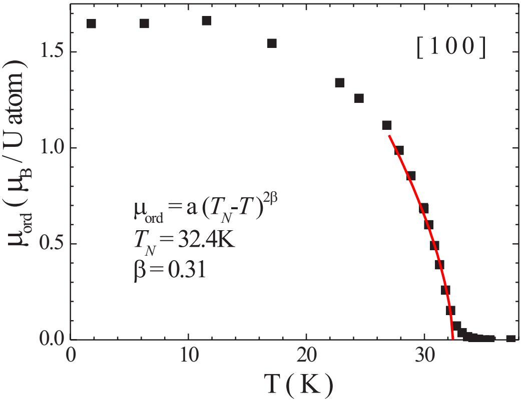

Figure 5.1: The temperature dependence of the integrated intensity of the [1 0 0] Bragg peak of annealed UPt$_2$Si$_2$. The line indicates the result of a fit to the critical region, with parameters as indicated in the plot.

the sublattice magnetization of a common antiferromagnet, with a T_N above 30 K. By fitting the data between 28 and 31.5 K to a critical behavior $\mu_{ord} \propto (T_N - T)^{2\beta}$ we obtain a transition temperature $T_N = 32.4$ K for $\beta = 0.3$ (Fig. 5.2).

In the Fig. 5.3 we depict the temperature evolution of the [1 0 0] magnetic Bragg peak width. As for the as–cast sample, above the bulk antiferromagnetic transition there is a temperature range with magnetic scattering intensity stemming from short range correlated regions. From the plot it is seen that magnetic clusters as down to 250 Å are observable. As temperature is lowered from 36 K to 32 K, an increase of the intensity is accompanied by a decrease of the peak width from 0.8° to 0.35° (resolution limit of the spectrometer).

Altogether, the analysis of the magnetic Bragg peak [1 0 0] shows only small changes of the magnetic state of the annealed UPt$_2$Si$_2$ compared to the sample in as–cast state. The antiferromagnetic transition temperature T_N is only 0.3 K higher, suggesting a slightly better crystal quality of the annealed

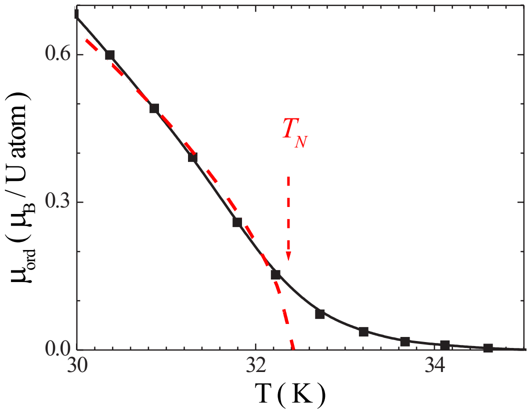

Figure 5.2: The temperature dependence of the integrated intensity of the [1 0 0] Bragg peak of annealed UPt$_2$Si$_2$ close to T_N. The dashed line indicates the result of a fit to the critical region; for details see text.

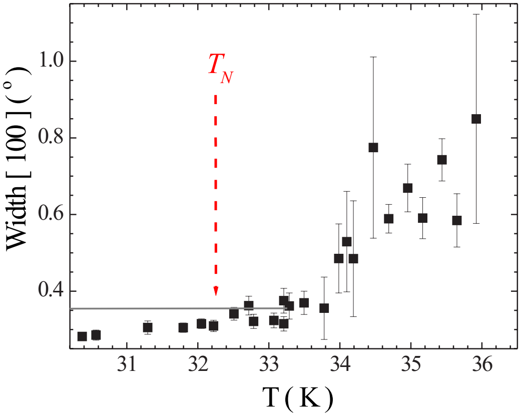

Figure 5.3: The temperature dependence of the line width for the [1 0 0] Bragg peak of annealed UPt$_2$Si$_2$; for details see text.

sample. Moreover, magnetic clusters are observable to higher temperatures, and the clusters are somewhat larger for the annealed crystal, which as well is consistent with an improved quality of the sample. Still, crystalline quality is not improved to a degree that transition temperatures of the order 35 K as previously reported are reached.

In the temperature range from 300 to 20 K the magnetic susceptibility of annealed UPt$_2$Si$_2$ qualitatively shows a similar behavior as the as–cast sample. $\chi(T)$ is anisotropic and possesses a maximum at low temperatures associated to the antiferromagnetic phase transition (see Fig. 5.4). Again, the transition temperature is determined from the condition $d(\chi T)/dT = max$ to $T_N = 31$ K, *viz.*, the same value as for the as–cast sample. However, we observe a substantial change of the magnetic susceptibility upon annealing at low temperatures and in overall χ values. To quantify these, we depict in Fig. 5.5 the normalized differences between the magnetic susceptibility of the as–cast χ_{as} and annealed χ_{ann} sample. Here, at high temperatures χ_{ann} is about 20% lower than χ_{as}. Below 20 K, however, this changes, and for measurements along the c axis, χ_{ann} is up to $\sim$ 40% higher.

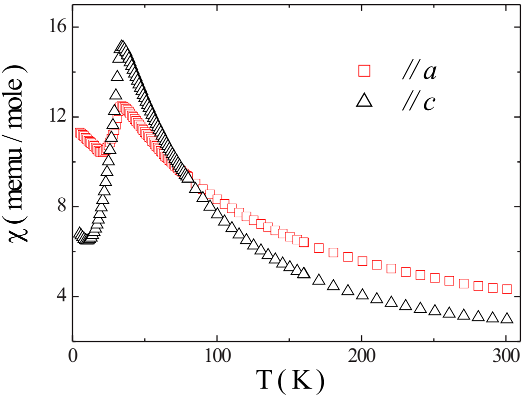

Figure 5.4: Temperature dependence of the magnetic susceptibility of annealed single crystalline UPt_2Si_2 along the two principal crystallographic directions in a magnetic field of $B = 0.1$ T.

At high temperatures χ follows a Curie–Weiss behavior (Fig. 5.6). The effective magnetic moment determined from a fit for both crystallographic directions are approximately 10% lower than for the as–cast samples (see Tab. 5.2). For the c axis the value of the effective magnetic moment corresponds to the highest possible values for uranium states ($5f^3$: $\mu_{eff} = 3.62\mu_B$, $5f^4$: $\mu_{eff} = 3.68\mu_B$). As well, the Curie–Weiss temperatures are also lower. For temperatures above $\sim$ 250 - 280 K again we observe a deviation from Curie–Weiss behavior, which we attribute to the previously mentioned first order phase transition at 305 K [3].

The most distinct changes in the magnetic properties upon annealing occur at low temperatures, where now for both crystallographic directions an upturn in the magnetic susceptibility appears. To further investigate this feature we carried out zero field and field cooled susceptibility measurements for temperatures 5 to 50 K in external magnetic fields between 100 and 10 000 G. In comparison to the measurements for the as–cast sample an enhancement of the ZFC/FC magnetothermal hysteresis is observed, while

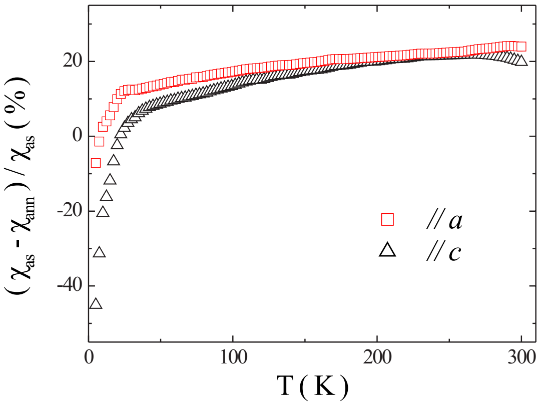

Figure 5.5: The normalized difference between the magnetic susceptibility of the as–cast and annealed samples UPt$_2$Si$_2$ measured along the a and c axis, as function of temperature.

the irreversibility and antiferromagnetic transition temperatures T_{irr}, T_N and T_{irr2} remain almost the same. The irreversibility itself (depicted as $\Delta\chi$ in Figs. 5.9 and 5.10) below T_{irr} is 1.5 and 3 times higher for the c and a axis, respectively, than for the as–cast samples.

Finally, we measured the magnetization along the c axis for the annealed sample with $B//c$ at 5 K in magnetic fields from 5 to -5 T. The results are presented in Fig. 5.11. The magnetization smoothly increases with B, while exhibiting a slight curvature for magnetic fields below 2 T, where weak hysteresis occurs. In order to better resolve the hysteretic behavior we plot the average magnetization $\Delta M = M_{d(u)} - (M_d + M_u)/2$ as function of magnetic field. Here, M_d and M_u represent the magnetization measured while sweeping down or up the field. The maximum values of ΔM are up to a factor five higher than measured for the as–cast sample.

Altogether, these results imply that while a thermal treatment of UPt$_2$Si$_2$ does not significantly influence the structural properties or the long range magnetically ordered state, the features connected to the magnetic clusters

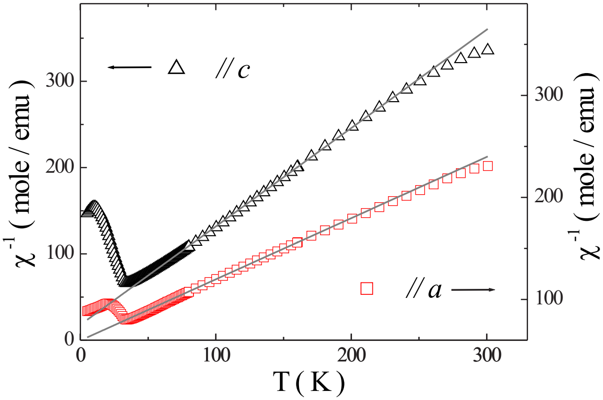

Figure 5.6: Temperature dependence of the inverse magnetic susceptibility χ of the annealed single-crystal UPt$_2$Si$_2$, measured for B // a and // c axis. The solid lines indicate Curie-Weiss fits, with the fit parameters summarized in Tab. 5.2.

Sample	fit range (K)	μ_{eff} (μ_B)	Q$_{CW}$ (K)
as–cast $B//a$	40-280	4.17	-116
as–cast $B//c$	40-250	3.09	-55
annealed $B//a$	40-280	3.65	-100
annealed $B//c$	60-250	2.65	-15

Table 5.2: High temperature magnetic properties of UPt$_2$Si$_2$; the values of the effective moment μ_{eff} and the Curie-Weiss temperature are extracted from fits of the high-temperature magnetic susceptibility to a Curie-Weiss law (see Figs. 4.7 and 5.6).

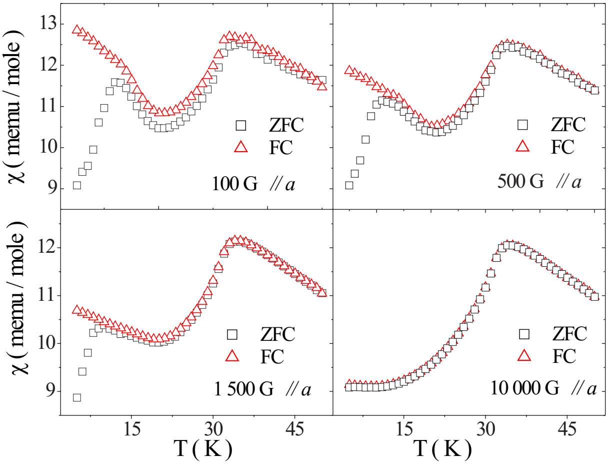

Figure 5.7: Magnetic susceptibility in various fields of annealed UPt_2Si_2 measured in a zero-field cooled and a field cooled experiments, with the magnetic field applied along the *a* axis.

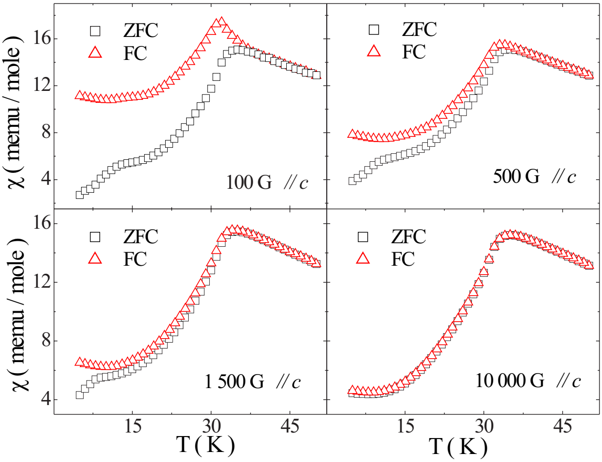

Figure 5.8: Magnetic susceptibility of annealed UPt$_2$Si$_2$ in various fields measured in a zero-field cooled and a field cooled experiments, with the magnetic field applied along the *c* axis.

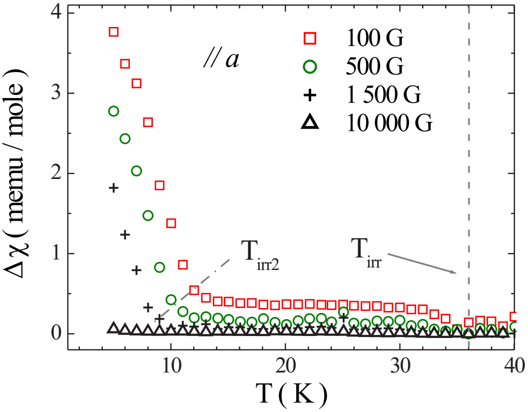

Figure 5.9: The difference in the magnetic susceptibility measured in field cooled and zero field cooled mode along the a axis for the annealed single crystal UPt$_2$Si$_2$.

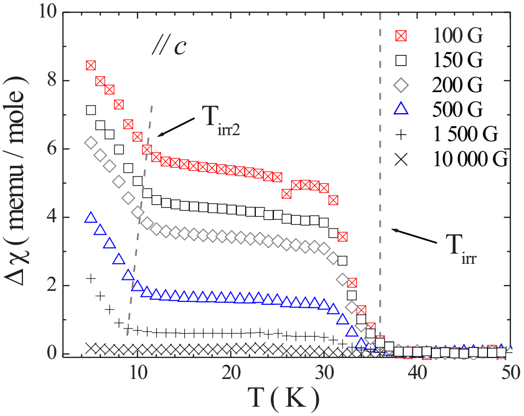

Figure 5.10: The difference in the magnetic susceptibility measured in field cooled and zero field cooled mode along the c axis for the annealed single crystal UPt$_2$Si$_2$.

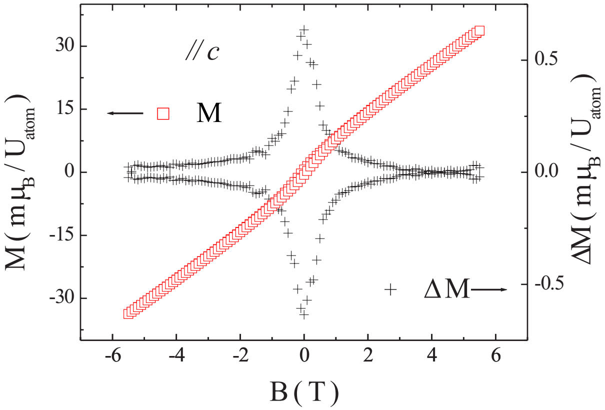

Figure 5.11: The magnetization loop M and the difference ΔM between measurements for the field swept up or down for annealed UPt$_2$Si$_2$ at $T = 5$ K with the field $B//c$.

are strongly affected. It indicates that annealing mostly affects the pinning properties of local structural inhomogeneities resulting from the crystallographic disorder.

5.4 Resistivity of annealed UPt_2Si_2

Finally, we measured the electrical resistivity for the annealed samples in the temperature range from 2 to 300 K. The data for a and c axis are presented in Figs. 5.12 and 5.13, where we include the data $\rho(T)$ for the as–cast samples. Along the a axis we observe for the as–cast and annealed sample a very similar temperature dependence of the electrical resistivity. Annealing results in the slight increase of ρ in the temperature range 50 to 280 K. In contrast, below 30 K the resistivity drops faster and saturates at a much lower value of the residual resistivity of 33 $\mu\Omega cm$. Further, for the annealed sample the resistivity measured along the c axis between 300 K and its maximum at 31 K is about 8% higher. However, again below T_N the resistivity decreases faster. Furthermore, for the annealed sample and $//c$, ρ at 2 K is only slightly higher than at 300 K, in contrast to the as–cast state, where the low temperature values are about 7% higher, clearly disvalidating Matthiesen's rule.

As for the as–cast samples, at low temperatures the resistivity closely resembles the behavior of systems with a gap in the spin-wave spectrum [4, 5]. Therefore, we fit the low temperature resistivity ($T < 22$ K) with

$$\rho = \rho_0 + bT(1 + 2\frac{T}{\Delta})exp(-\frac{\Delta}{T}), \tag{5.1}$$

with Δ as energy gap in the spin-wave spectrum. The data for both directions are very well described by the fit (Figs. 5.14), with the fit parameters presented in Tab. 5.3. Overall, the fit parameters for the as–cast and annealed samples along the a axis are similar. As pointed out, ρ_0 for the annealed compound is about 17% lower, while b is slightly higher, but the energy gap does not change. In contrast, the modification of the crystallographic disorder level influences more strongly Δ and b derived from the measurements along the c axis. Δ increases to 31 K, while b is two times larger than for as–cast sample.

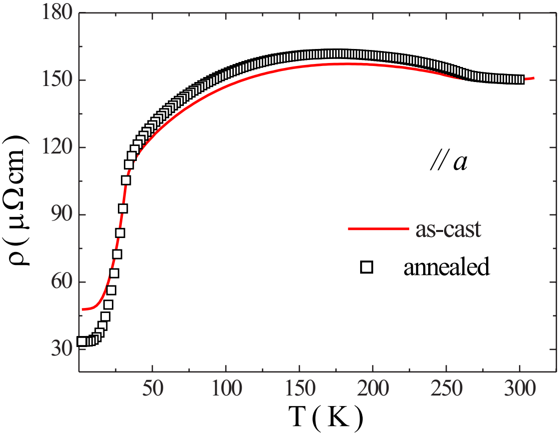

Figure 5.12: The temperature dependence of the electrical resistivity ρ for as–cast and annealed UPt_2Si_2 measured along the a axis.

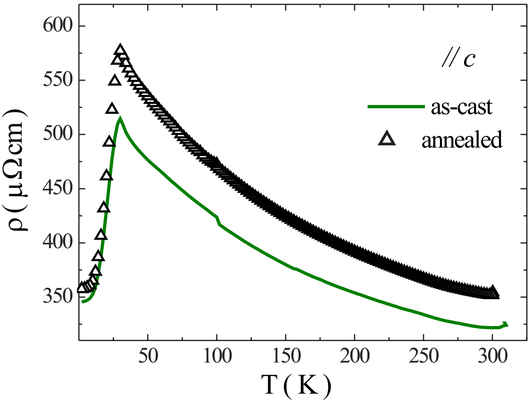

Figure 5.13: The temperature dependence of the electrical resistivity ρ for as–cast and annealed UPt_2Si_2 measured along the c axis.

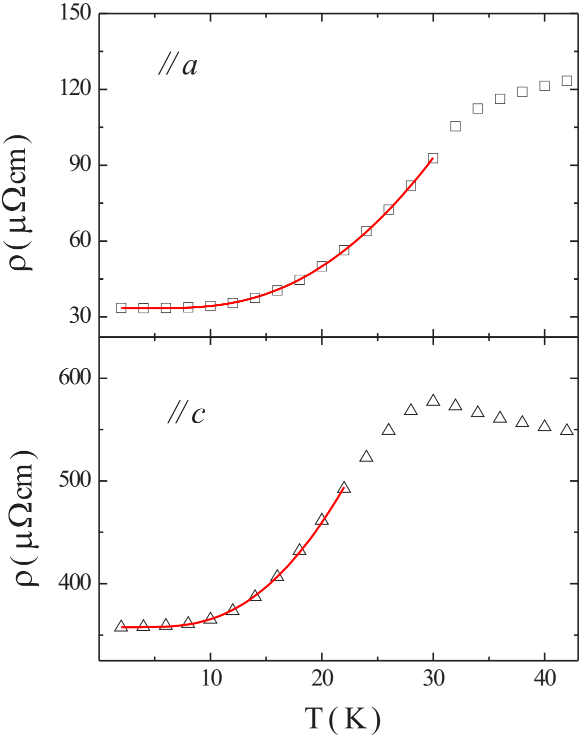

Figure 5.14: The temperature dependence of the electrical resistivity along the *a* and *c* axes for annealed UPt$_2$Si$_2$. The solid lines are fits to the data using Eq. 5.1; for details see text.

Sample	ρ_0 ($\mu\Omega$cm)	b ($\mu\Omega$cm/K)	Δ (K)
as–cast //*a*	40	2.2	39
as–cast //*c*	348	5.88	26
annealed //*a*	33	2.9	39
annealed //*c*	358	10.5	31

Table 5.3: The fit parameters for both principal crystallographic axes of as–cast and annealed UPt_2Si_2 using Eq. 5.1, with Δ as the gap in the spin wave spectrum; for details see text.

5.5 Conclusions

We have performed a detailed investigation of the structural and physical properties of annealed UPt_2Si_2. From a comparison to the corresponding as–cast data we assess the effect of the heat treatment on the structural and physical (ground state) properties. The structural study of UPt_2Si_2 shows that the heat treatment does not result in a detectable increase of the crystallographic order.

The investigation of the magnetic properties reveal that the long range magnetically ordered state is hardly influenced by the heat treatment. Only, the properties which mirror the character of the magnetic clusters at low temperatures appear much more pronounced. Furthermore, the quotient of the low temperature resistivity and its room temperature value ρ_{2K}/ρ_{300K} is much lower for both crystallographic axes. This indicates that the annealed sample contains a lower level of crystallographic disorder. In this sense, the resistivity turns out to be a much more sensitive probe to detect changes of the disorder level than direct techniques like (high resolution) neutron scattering.

We speculate that the more pronounced magnetothermal hysteresis reflects a growing cluster size, as detected in neutron scattering.

Bibliography

[1] H. Ptasiewicz-Bak, J. Leciejewicz, and A. Zygmunt, Solid State Comun. **55**, 601 (1985).

[2] R.A. Steeman, E. Frikkee, S.A.M. Mentink, A.A. Menovsky, G.J. Nieuwenhuys, and J.A. Mydosh, J. Phys.: Condens. Matter **2**, 4059 (1990).

[3] H. Amitsuka, private communication (2002).

[4] Y.B Ning, J.D. Garret, and W.R. Datars, Phys. Rev. B **42**, 8780 (1990).

[5] Y.B Ning, J.D. Garret, C.V. Stager, and W.R. Datars, Phys. Rev. B **46**, 8201 (1992).

Chapter 6

Proximity Effect in $CeCu_6$/Nb bilayers

6.1 Introduction

The proximity effect in superconductor / non-superconducting material (S/N) systems has been intensively studied throughout the last decades. Commonly, for N a normal metal (M) or a ferromagnet (F) is chosen. For sufficiently thin layers the proximity effect is very pronounced and can lead to unusual phenomena like for example π coupling in S/F/S junctions [1]. One of the basic parameters which determines the physical properties of such thin film structures is the electronic ground state of the N material. Therefore, a very intriguing issue is a study of the proximity effect on S/N interfaces with N being strongly correlated material such a heavy fermion metal (HF). In this case it is expected that:

- presumably there is small diffusion constant due to the low Fermi velocity v_F in HF ($v_F \sim m^*$),
- pair breaking may be strong because of the strong electron–electron interactions or residual magnetic moments,
- a low interface transparency may result from the Fermi velocity mismatch, which can shield the superconductor from the HF metal, suppresses the proximity effect.

For such a study the heavy fermion material has to be available in thin film form. These materials, however, are intermetallic compounds which consist of up to four chemical elements. In this case, it is essential to keep the control over the precise stoichiometry, as even small changes may affect the electronic ground state. Furthermore, many heavy fermions contain uranium, which is hard to handle in thin film preparation. For these reasons only few heavy fermions system have been obtained in thin layer form. As one of the first heavy fermion compounds, $\mathrm{CeCu_6}$ has been prepared as a thin film by D. Groten *et al.* [2–4]. Based on these results, we carried out the first study of the proximity effect in a system consisting of thin films of the HF material $\mathrm{CeCu_6}$ combined with a thin superconductor layer S, in this case Nb.

$\mathrm{CeCu_6}$ is of particular interest for such a study as it represents an archetypal heavy fermion system:

- at low temperatures the specific heat is dominated by the electronic contribution, with a Sommerfeld coefficient $\gamma(T = 0) = 1.6$ J/mole K^2 [5]. This very high value of γ is directly related to the high density of states at Fermi surface and hence to the heavy mass of the quasiparticles (in comparison with the alkali metal Na, $\gamma_{Na} \sim 1$ mJ/mole K^2).

- at high temperatures the magnetic susceptibility shows Curie–Weiss behavior. The effective moment of 2.5 μ_B is in agreement with a Ce^{+3} state (2.54 μ_B). At low temperatures Pauli paramagnetism has been observed with strongly enhanced χ_p values [6].

- the electrical resistivity ρ shows weak anisotropy. For the principal crystallographic directions ρ displays a maximum for temperatures $\sim$ 5–15 K. At very low temperatures Fermi-liquid behavior has been observed [7–10].

For thin film preparation a variety of sample characterization techniques has to be used in order to determine stoichiometry and morphology of the systems. In the following section the techniques mainly applied in this study are briefly introduced. We extensively discuss the preparation conditions and the quality of the $\mathrm{CeCu_6}$ and Nb layers as a key point of our investigations. Further, we present the data of the critical temperature T_c as a function of the Nb thickness d_S and the temperature dependence of the upper parallel critical field $H_{c2}^{||}$ of bilayers of Nb/$\mathrm{CeCu_6}$. These thermodynamic properties have been modelled by Ciuhu and Lodder [11] based on the Takahashi–Tachiki theory and values of the interface resistance R_B has been obtained. We compare the results to those of Nb/Cu triple and double layers.

6.2 Sample characterization methods

To determine the thickness and the composition of the prepared thin films X–ray reflectometry, Rutherford back scattering and electron probe microanalysis have been applied. Further, X–ray diffraction has been employed for crystallographic analysis of the polycrystalline $CeCu_6$ layers. The sample surface has been studied by scanning electron microscopy and atomic force microscopy, which provide information about the surface roughness.

Here, a short overview of these methods is given, especially with respect to resolution limits and applicability.

6.2.1 Rutherford Back Scattering

Rutherford back scattering (RBS) is a powerful technique which allows to precisely determine the thickness profile and chemical composition of thin film samples. In this method, a beam of highly energetic helium ions (typically several MeV, in our experiments 2 MeV) is directed at the sample. A fraction of the incident ion beam is elastically backscattered from the target. The energy of the backscattered particles is related to the mass of the target element. The higher the mass of the nuclei, the higher the energy of the backscattered ions. The number of the backscattered particles is proportional to the square of the atomic number of the target elements. This allows for a mass discrimination. Additionally, helium ions lose energy along their path in the sample through interaction with the electron clouds. This means that the ions scattered inside the sample from element X will have lower energy than the ions scattered on the sample surface from the same element. The energy reduction depends on the distance the ions have to travel to the surface through the target and the chemical composition along their path. The energy of the backscattered ions undergoes multichannel analysis. The basic information obtained through integration of the measured energy spectrum, is the number of the atoms of an chemical element per certain unit area. These data are compared with calculations for a model specifying amount of different chemical elements and their distribution in the sample. The method provides depth information up to 2 μm and depth resolution down to 1 nm [12].

The measurements were carried out at the Institute for Atomic and

Molecular Physics AMOLF in Amsterdam. The energy of the backscattered He^+ ion, is converted into 512 channels ranging from 0 to 2 MeV. For the simulation of the sample profile we applied the widely used RUMP program, which allows to simulate multi–layers and interface reactions such as in–diffusion for complicated multiple layer structures [13].

6.2.2 X–ray diffraction and reflectivity

The X–ray diffraction measurements in the standard geometry $\Theta/2\Theta$ are mainly applied by the characterization for crystallographic structure for a given sample.

The reflectivity measurements are a special case of small angle X–ray scattering measurements and allow for this films to estimate the layer thickness and the roughness of the interface.

The (000) Bragg reflection, which is used in this characterization technique, provides information of the average electron density. For the introduction to the reflectivity let us discuss a simple model system with a monolayer deposited on top of the substrate. If a monolayer and a substrate have the same lattice structure, the system can be described as a product of a infinite lattice function and a electron density function. The Fourier transformation of the model gives in the scattered intensity the Bragg reflection (for the infinite lattice), and some oscillatory term (representing the density function), with the period dependent of the film thickness.

By the measurements of the (000)–reflection at small angles all Bragg reflections are neglected and only information of the electronic density function itself is left. In the Born approximation the reflected intensity as a function of q_z is given by [14]:

$$I(q_z) \propto \frac{1}{q_z^4} \left| \int \frac{d\rho(z)}{dz} \exp(iq_z z) dz \right|^2 \tag{6.1}$$

where $q_z = (4\pi/\lambda) sin(\alpha_i)$, α_i – scattering angle, z – the direction perpendicular to the surface, ρ – electron density. The reflectivity is therefore sensitive to the change of the electronic density profile. This allows to precisely estimate the thickness of the layer and even the roughness of the interface.

6.2.3 Electron Probe Microanalysis and Scanning Electron Microscopy

In this technique an electron beam is focused on the sample surface. In case of electron probe microanalysis (EPMA), the typical beam energy is on the of order 20 keV. In scanning electron microscopy (SEM) electrons with energies between 1 keV and 20 keV are used. As a result, some electrons are backscattered without changing their initial energy. Part of the beam is inelastically backscattered with energy loss up to 50 eV [14]. Additionally, secondary electrons are produced. They undergo multiple scattering processes on their way to the surface, and therefore their energy spectrum is broad, with a maximum below 50 eV. Finally, the electron beam can ionize atoms by removing the shell electrons. If the electron comes from an inner shell, an electron from a higher level will fill this free state. The energy, which is set free in this process will either cause an emission of a X–ray quantum, or of an additional electron from high lying levels (Auger electrons). The probability that one there processes occurs is a function of atomic mumber. The emission of Auger electrons prevail for light elements. For heavy atoms X–ray emission is much more probable. The X–ray and Auger electron spectra are characteristic for any given element, and can be used to determine the chemical composition.

In EPMA the characteristic X–ray emission spectra of a sample are analyzed applying a numerical algorithm which accounts for the intensity of the characteristic X–ray emission. The intensity is connected to the excitation volume (for details see Ref. [2]). For thin films the relatively large excitation volume of EPMA of the order of 1 μm^3 causes a problem in the exact analysis of the stoichiometry. Different energies of the incoming electron beam have to be used to improve the sensitivity regarding profile analysis of the sample. Furthermore, it has been shown that with respect to compositional analysis of thin films the relative accuracy of the method may be substantially reduced (up to ~ 3 at%) [2].

SEM is a microscopic method, which in contrast to X–ray scattering methods provides a real space image of the sample. The images are very useful in a qualitative study of a surface. The spatial resolution is achieved by scanning the sample with the beam. By application of a different detectors several types of contrast can be achieved. For example, the edge contrast by examination the secondary electron or material contrast by analysis of inelastic scattered or Auger electrons. In our case a lateral resolution up to 100 nm has been obtained.

6.2.4 Atomic Force Microscopy

Atomic force microscopy (AFM) allows to image 3D surface profiles with a very high resolution, even up to the atomic level. The central element of an AFM microscope is a fine scanning tip connected to a cantilever. The images are taken by scanning the surface relative to the tip, which is brought in very close proximity. The cantilever will deflect due to the force between the tip and the surface. The force can arise from van der Waals, electrostatic, magnetic (in non-contac AFM mode where the distance is greater than 1 nm) or repulsive atomic interactions (contact mode). The deflection of the cantilever is measured using a laser or piezoelectric devices. Piezoelectric devices also very precisely control the lateral and the vertical sample position, which allows for very precise measurements.

AFM can be further applied in a qualitative roughness analysis. Therefore, SEM and AFM are used in this project as complementary techniques.

6.3 Preparation and characteristization of thin film structures

The thin film samples were prepared in ultra–high vacuum system (UHV) using a DC–magnetron sputtering technique. The background pressure was reduced to a low level of $\sim 5 \times 10^{-10}$ mbar. In our experiments, we found the background pressure to be a crucial parameter to obtain high quality $CeCu_6$ and Nb layers. The UHV preparation chamber (CEFF) contains four sources, which allows sputtering of different materials in the same chamber. The sputtering process was carried out in inert argon gas. The argon pressure, one of the defining parameters for the sputter rate, could be very finely adjusted using a needle valve. For all experiments the pressure was set to 2.5×10^{-3} mbar.

The substrate was clamped onto the sample holder, which consists of a copper tube, fixed to the top flange of the load lock and to a long bellow.

This equipment allows to move the sample over a distance of 30 cm. The sample holder can be lowered from the load lock into the chamber. Inside the copper tube, the sample heater and the thermocouple (K type) are placed in close vicinity to the substrate. Additionally, the tube can be cooled with nitrogen gas. This permits film preparation at variable temperatures range. The present system allows to place only one substrate at a time in the preparation chamber. Furthermore, the load lock stays open during the sputtering process, considerably increasing the preparation time. Hence, before the load lock can be opened, it has to be pumped and heated up externally to about 120°C over 12 hours in order to reach the pressure of $\sim 1 \times 10^{-9}$ mbar. (For further details concerning the sputtering system see Ref [2]). Primary aim of this work were transport measurements on Nb/$CeCu_6$ bilayers, which require knowledge of the exact sample geometry. Therefore, we used optical lithography and ion etching to create geometrical structures suitable for transport measurements. In this process, the sample surface after being cleaned in acetone and isopropanol is covered with a photoresist and subsequently dried at high temperatures. Then, a glass mask is lowed upon the sample surface. Over the mask covering the required geometry, the sample is exposed to UV. In the developing process, after removing the glass mask the solvent removes all photoresist, apart from the places which were previously covered by the mask. Further temperature treatment is used to fix the structure. In the next step, with ion etching the material which is not hidden with the resist is sputtered away and the desired structure appears (the remaining photoresist can be removed in acetone). The etching time depends, besides of the sputtering condition, on the sample material and has to be determined experimentally.

6.3.1 Thin films of $CeCu_6$

The preparation of $CeCu_6$ films is based on the results reported in Refs. [2,4]. The high temperatures, 450 and 350 °C, are chosen to achieve polycrystalline growth of the film. To prevent Cu diffusion we use Si-substrates with amorphous SiO_2 buffer layers of $\sim$ 270 nm thickness.

$CeCu_6$ is sputtered from two different sources, *i.e.*, pure Ce and Cu targets. The deposition from one source was found to be unsuccessful in

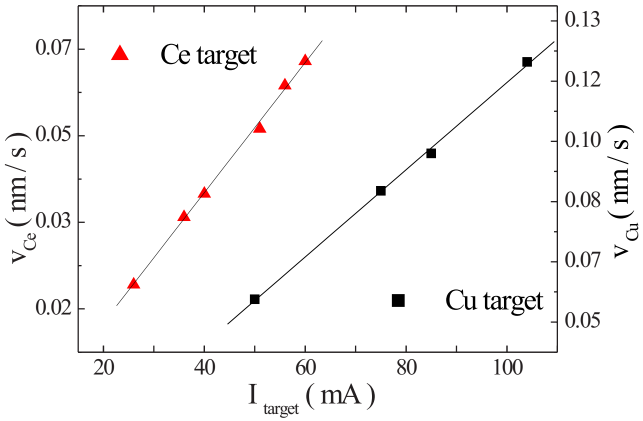

Figure 6.1: The sputtering rate of Cu and Ce targets in dependence of the sputtering current. The lines represent the linear fits to the data, for detail see text.

Sample	I_{Ce} (mA)	U_{Ce} (V)	I_{Cu} (mA)	U_{Cu} (V)	chemical element	EPMA Spot1	EPMA Spot2	EPMA Spot3
S1 (12202)	31	268	54	325	Ce Cu	14.4% 85.6%	13.8% 86.2%	14.6% 85.7%
S2 (13202)	38	278	71	331	Ce Cu	12.6% 87.4%	12.6% 87.4%	12.3% 87.7%
S3 (14-2)	40	280	71	328	Ce Cu	13.3% 86.7%	13.0% 87.0%	12.9% 87.1%

Table 6.1: Sputtering conditions and results of the EPMA stoichiometry analysis for chosen samples, I and U are current and voltage values of the sputtering target during the preparation, for further details see text.

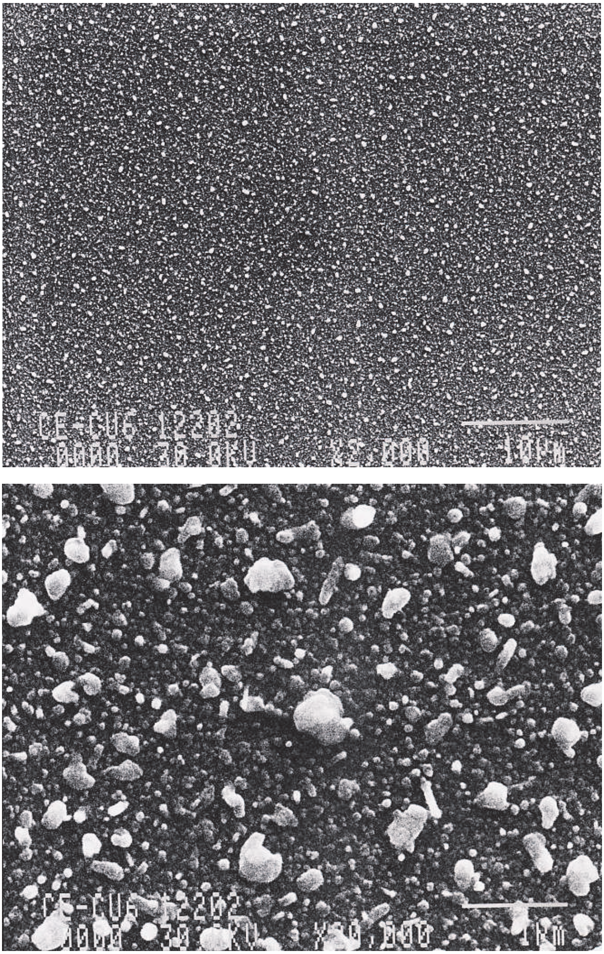

Figure 6.2: SEM pictures of S1 samples for a different resolution. Note the scale of 10 μm and 1 μm given at the lower right corner of each picture.

a previous study. Because Ce and Cu have different sputter rates, in case of one source deposition, a preferential sputtering occurs. The alternative sputtering from two sources requires very exact calibration. In a first step, we separately measure the sputtering rate v for Ce and Cu in dependence of the source current at a constant Ar pressure of 2.5×10^{-3} mbar (Fig. 6.1). For this purpose, the deposition time and film thickness on a quatrz crystal thin film monitor (QTM) are registered. As the QTM has been calibrated for Cu, the measured sputtering velocity value for Ce is only an approximation. Still, the obtained values allow us to choose starting values for the Ce and Cu source current.

Immediately before the deposition, the target were presputtered for about 5 minutes, at low sputtering rate to remove possible oxygen contaminations and reach a high purity of $CeCu_6$ layers. After codeposition of Ce and Cu, the sample is cooled down to room temperature and an amorphus Si cap layer is deposited on top of it. This way we reduce oxidation of the Ce–compound.

Representative results are presented in Tab. 6.1. For characterization, we initially employed EPMA, in order to determine the appropriate preparation conditions to produce thin films of the desired stoichiometry 14.3 at% Ce and 85.7 at% Cu. Furthermore, the surfaces of the samples are investigated by SEM. Sample S1 (code for the SEM picture: 12202) is sputtered at a substrate temperature of $T = 450$ °C. The EPMA measurements on three different spots of the sample seem to suggest an almost perfect chemical composition. However, the SEM images (Fig. 6.2) reveal a very rough surface. Actually, the initial roughness of the Ce–compound interface must be even higher as the Si cap layer “flattens” the surface. The grains appearing bright in the SEM pictures have a lateral dimension of up to 0.5 μm. Such grainy films were connected in the previous investigations [2] to an excess of Cu in the compound. The grains could be a copper rich second phase. EPMA, however is not a sensitive method to measure the composition of the grains, as the excitation volume is to large ($\sim$1 μm^3), additionally the depth resolution is not sufficient to estimate a depth profile. Therefore, the stoichiometry obtained by EPMA is an average value for the large grains and the smooth background. Because the spots are randomly chosen, the grain and the background contribute in different amount to average stoichiometry. This probably causes higher spot to spot variation of the composition for this sample. In the further analysis we performed RBS measurements which reveal a strong vertical inhomogeneity for the Ce-compound layer. Fig. 6.3 shows the RBS spectrum in comparison to the calculated spectrum for a model of Si/SiO_2/layer 4/layer 3/layer 2/layer 1, where layer 4 (50 nm) consists of 20% of Cu and SiO_2, layer 3 (15 nm): Ce 13.9% and Cu 86.1%, layer 2 (25 nm): Si 26.9% Cu 52.2%, Ce 20.9% and layer 1 (14 nm) Si. Within this model we can calculate the high energy signal of Ce and Cu which are described to the top layers. According to these calculation, the Ce concentration exceeds the desired value. However, we observe the signal from Ce and Cu even at much lower energy than expected within the model. This strongly suggest that for the full analysis we have rather to consider a diffusion into a substrate, which is much stronger for Cu than for Ce. The simple model of the homogeneous mixed layer of Cu, Si and SiO_2 does not apply. The strong diffusion can be described to the high substrate temperature during the deposition. The RBS spectra suggest rather a surplus of Ce, although the analysis for such highly inhomogeneous layers is difficult, and without a diffusion model (for the sample region close to the substrate) no exact determination of the Ce to Cu ration for the whole sample can be made.

As a consequence of these results, the preparation conditions were changed. Sample S2 (code on SEM pictures: 13202) is sputtered at a much lower substrate temperature of $T = 350$ °C. Furthermore, the sputtering rate ratio (v_{cu}/v_{ce}) is increased. In the case of sample S1, we carry out EPMA (Tab. 6.1), SEM and RBS measurements. According to EPMA, the average stoichiometry of the produced layer corresponds to $Ce_{0.875}Cu_{6.125}$ (Ce 12.5%, Cu 87.5%). RBS analysis (Fig. 6.4) suggests rather a structure with a 54 nm layer of $Ce_{0.98}Cu_{6.02}$ (Ce 14.0%, Cu 86.0%) and with a copper rich, 8 nm thick $Ce_{0.63}Cu_{6.37}$ (Ce 9.0%, Cu 91.0%) bottom interface. No diffusion is observed, neither from Cu/Ce into the substrate nor from SiO_2 into the sputtered layer. This implies that the substrate temperature is adequately low. The SEM pictures show (Fig. 6.5) a smooth surface with a few grains (the bright spots, better to be recognized on the upper, higher resolution picture). These probably correspond to a copper rich phase, which in some spots could appear on the surface.

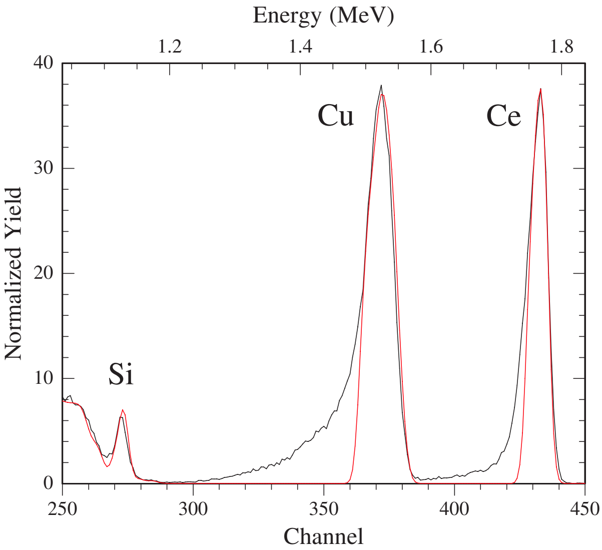

Figure 6.3: RBS spectrum taken with ^{4}He-ions of 2 MeV of the sample S1. The different elements are indicated. The thin smooth line is a fit to the measured curve. For details see text.

To slightly lower the relative Cu concentration in the produced layer, v_{ce} is increased (Tab. 6.1 - sample S3 - SEM pictures code: 14-02), at a constant substrate temperature T = 350 °C. With EPMA the chemical composition of this sample is determined at Ce$_{0.92}$Cu$_{6.08}$ (Ce 13.1%, Cu 86.9%). According to RBS (Fig. 6.6), however, sample S3 consists of three well separated layers, SiO$_2$ (300 nm)/Ce$_{0.99}$Cu$_{6.01}$ (62 nm) (Ce 14.1%, Cu 85.9%)/ Si (16 nm), with no diffusion on the interfaces. Considering the much lower resolution of EPMA compared to RBS for thin films, these results confirm the correct stoichiometry of the CeCu$_6$ layer. Further, the sample surface is very flat, as indicated by SEM images (Fig. 6.7). The white spot is a dust particle, which was used to focus on. No other grains are recognizable.

According to the X–ray diffraction measurements, the S3 sample is polycrystalline, with a preferential random-orientation. We have observed sharp

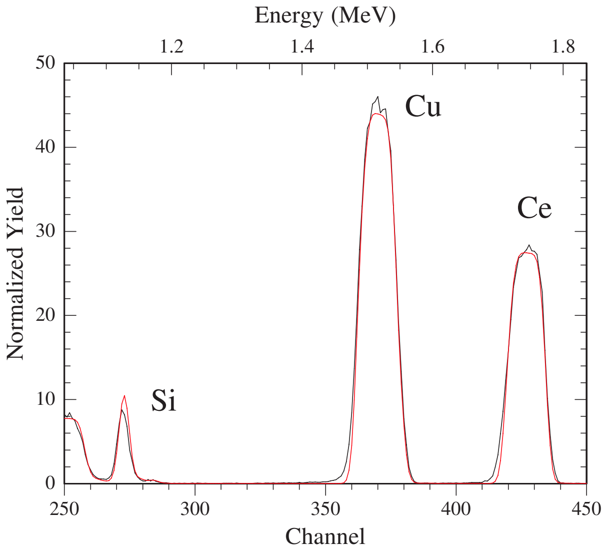

Figure 6.4: RBS spectrum taken with ^{4}He-ions of 2 MeV of the sample S2. The different elements are indicated. The thin smooth line is a fit to the measured curve. For details see text.

Bragg peaks of the orthorhombic CeCu$_6$ structure. The results are in good agreement with earlier reports [2,3].

Additionally, two more samples were prepared under the same conditions as S3 (with a CeCu$_6$ layer thickness of 75 and 188 nm) and the low temperature transport properties of these samples have been studied. For these systems an additional lithography step was required to remove the Si film and to sputter the gold contacts. The resistivity measurements were carried out in a conventional Quantum Design Physical Properties Measurements system (PPMS). As depicted in Fig. 6.8 below 30 K, ρ shows a negative slope for all samples. At low temperatures a maximum in the resistivity is observed for the 75 nm and 188 nm CeCu$_6$ layers at $T_{max} \sim 5$ K and $T_{max} \sim 4$ K respectively. This temperature dependence of the resistivity and its values are very similar to reported in Ref. [2,4] (see Fig. 6.9)

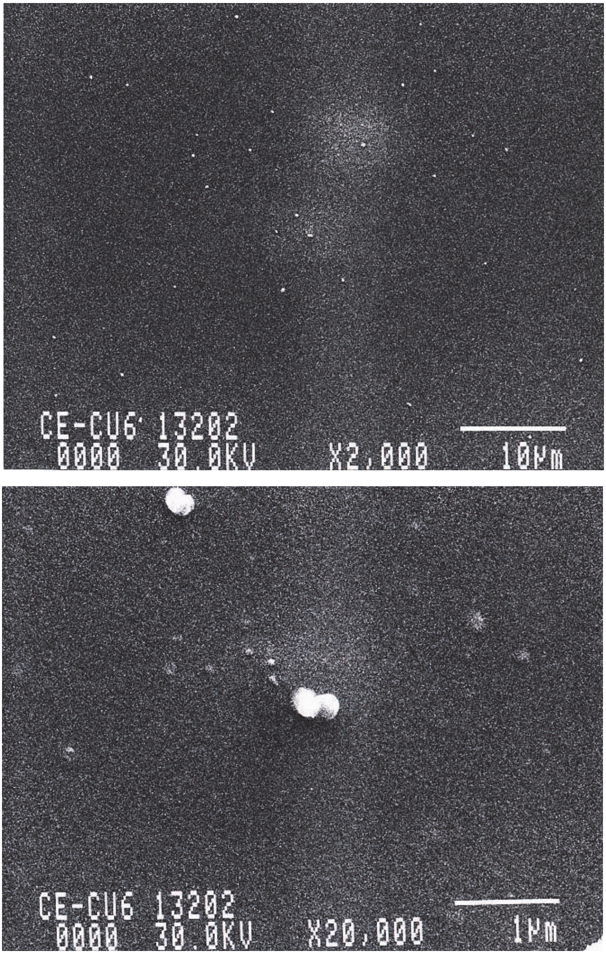

Figure 6.5: SEM pictures of S2 samples for different resolution. Note the scale of 10 μm and 1 μm given at the lower right corner of each picture.

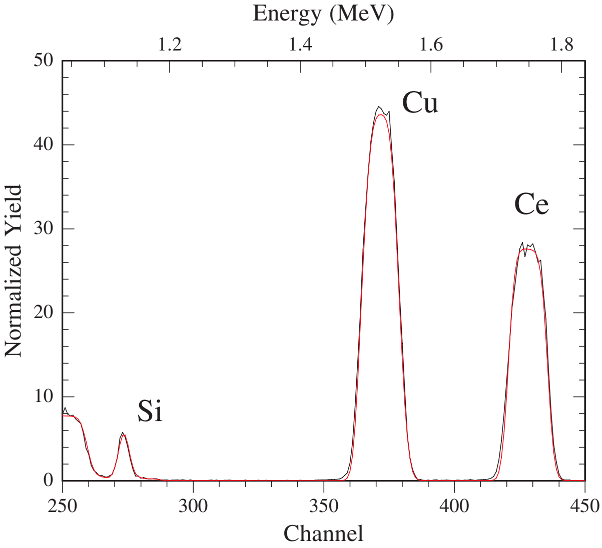

Figure 6.6: RBS spectrum taken with ^{4}He-ions of 2 MeV of the sample S3. The different elements are indicated. The thin smooth line is a fit to the measured curve. For details see text.

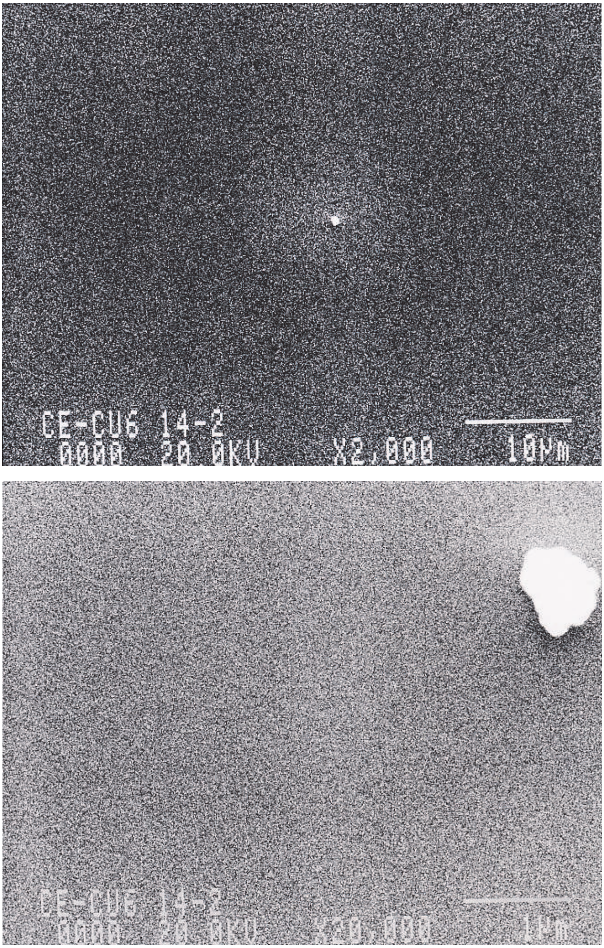

Figure 6.7: SEM pictures of S3 samples for different resolution. Note the scale of 10 μm and 1 μm given at the lower right corner of each picture.

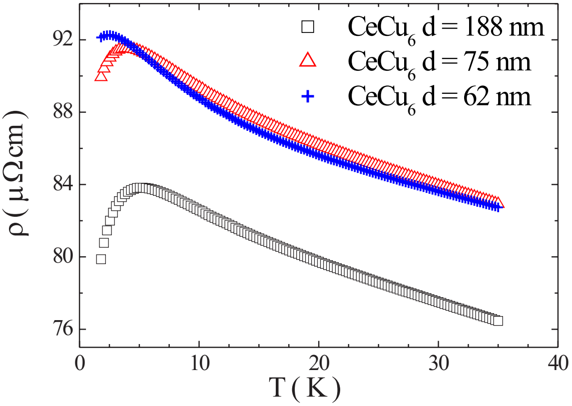

Figure 6.8: Electrical resistivity as a function of temperature for $CeCu_6$ films of 188 nm, 75 nm and 62 nm.

and observed for the bulk behavior [7, 9]. The 62 nm thick $CeCu_6$ layer $T_{max} \sim 2$ K is shifted much stronger to lower values, which is probably due to an intrinsic effect caused by the size reduction [2, 4]. In the further study the 75 nm $CeCu_6$ films have been used as representative for the bulk material.

6.3.2 Nb films

Our study of the proximity effect requires Nb layers for which the effect of T_c suppression from a reduction of the film thickness is comparatively small. The lowering of the superconducting transition temperature in thin Nb films is caused by the mixture of different effects such as oxidation through an unprotected top layer, a weak proximity effect with the substrate and lifetime broadening due to growth disorder [15, 16]. Homogeneous layers with small grain size (smooth surface) will therefore be characterized by a small suppression of T_c. To obtain such high quality Nb films, we have systematically searched for the suitable preparation conditions with respect

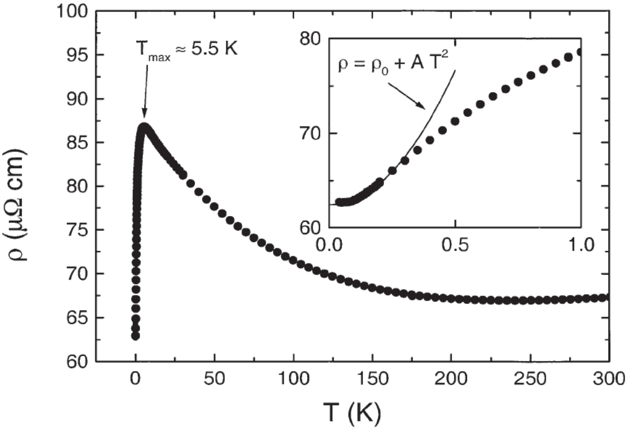

Figure 6.9: Electrical resistivity as a function of temperature for CeCu$_6$ films of 190 nm. The insert shows the low–temperature region. The solid line is fit to a T^2 law, characterizing a Fermi liquid behavior after Ref [3].

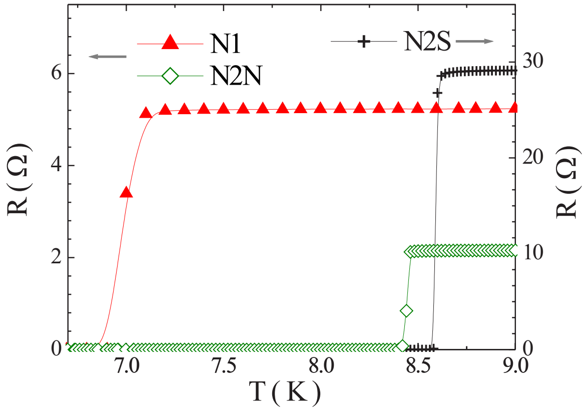

Figure 6.10: Electrical resistivity as a function of temperature for 50 nm Nb films prepared in at the different background pressure. For details see text.

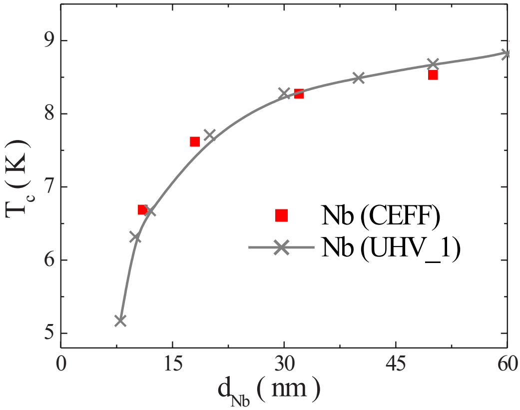

Figure 6.11: Critical temperature T_c versus superconducting layer thickness d_{Nb} for the sample prepared in the CEFF and in the UHV$_1$ system as reported in Ref [17].

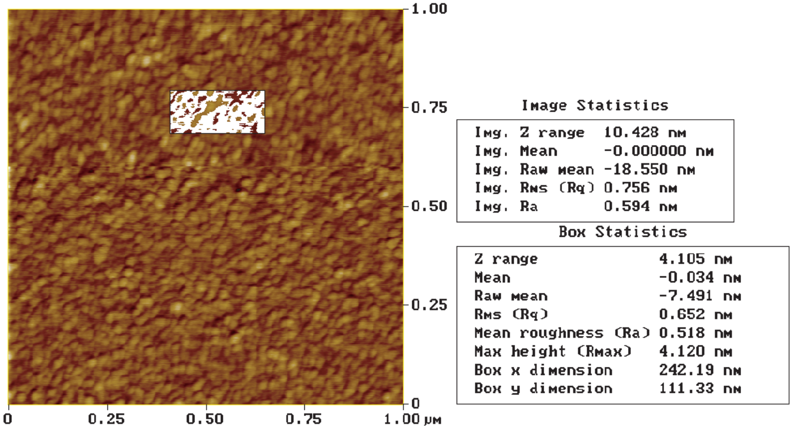

```
Image Statistics
Img. Z range    10.428 nm
Img. Mean       -0.000000 nm
Img. Raw mean   -18.550 nm
Img. Rms (Rq)   0.756 nm
Img. Ra         0.594 nm
```

```
Box Statistics
Z range                 4.105 nm
Mean                    -0.034 nm
Raw mean                -7.491 nm
Rms (Rq)                0.652 nm
Mean roughness (Ra)     0.518 nm
Max height (Rmax)       4.120 nm
Box x dimension         242.19 nm
Box y dimension         111.33 nm
```

Figure 6.12: AFM image and roughness analysis of 32 nm thick Nb sample. Additionally, statistics of the chosen part of sample surface (marked as a white box) is presented.

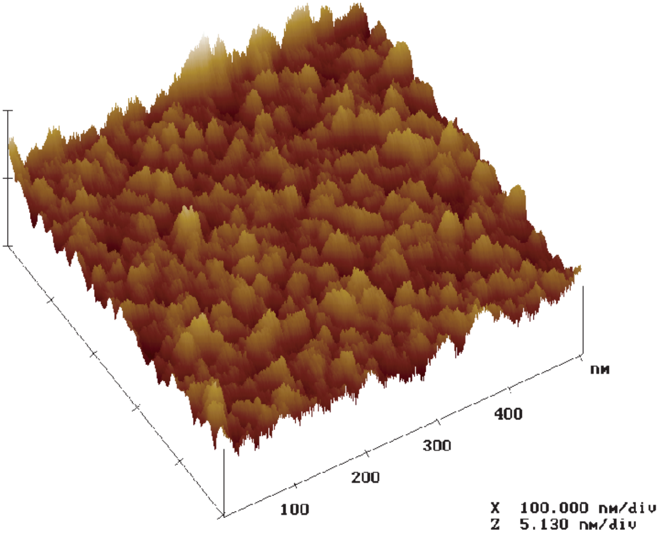

Figure 6.13: The 3D AFM image of 32 nm thick Nb sample. Note the scale given at the lower right. X denote the scale in the sample surface plane, Z is the scale in the direction perpendicular to the surface.

to background pressure, substrate temperature and sputtering rate. The high quality of our films is verified by electrical resistivity measurements and AFM analysis. The thicknesses of the samples was established by X–ray reflectivity and RBS measurements.

To reduce contamination of the Nb films with impurities the presputtering of the Nb source is required (at low sputtering rates for ~ 5 minutes). Furthermore, the background pressure has to be lower than $1{\times}10^{-8}$ mbar. Fig. 6.10 shows the resistivity of two 50 nm samples deposited at equal sputtering conditions but at different background pressures of $1.2{\times}10^{-8}$ mbar (N1) and $7{\times}10^{-9}$ mbar (N2). The higher background pressure leads to a considerable reduction of the T_c and the broader superconducting transition. One part of sample N2 has been measured in unstructured form (as N1 sample) and labelled as N2N. At the other part, a standard 4-point geometry structure has been created with the bridge widths of 200 μm and the voltage contact distance of 1.2 mm. The structured sample N2S shows a slightly (~ 0.1 K) higher T_c than the unstructured.

The best films are obtained with a sputtering rates of ~ 0.1 nm/s and a substrate temperature of $T = 20$ °C. To improve the sample quality the background pressure has further been lowered to about $5{\times}10^{-10}$ mbar. To confirm that under these conditions high quality Nb films are produced, we have measured various films with a thickness ranging from 11 nm to 50 nm. In Fig. 6.11 we present the results in comparison with an earlier study of Nb–layers prepared via DC–magnetron sputtering in a different deposition system (UHV1) [17]. Both studies show very similar results, for the full range of film thickness. According to X–ray reflectivity measurements, for all samples the roughness of surface is of the order of 1 nm, which corresponds to the resolution limit of the method. Also the AFM roughness analysis reveals a very smooth surface. For example for the 32 nm thick Nb film we observe an average roughness of ~ 0.5 nm (Fig. 6.12 and Fig. 6.13). For additional images on the different sample spots see the Appendix.

6.3.3 Nb/$CeCu_6$ bilayers

We prepared a set of $CeCu_6$(75 nm)/Nb(d_{Nb}) layers with variable Nb thickness d_{Nb} in the range 10 nm to 50 nm. To prevent Cu diffusion we use

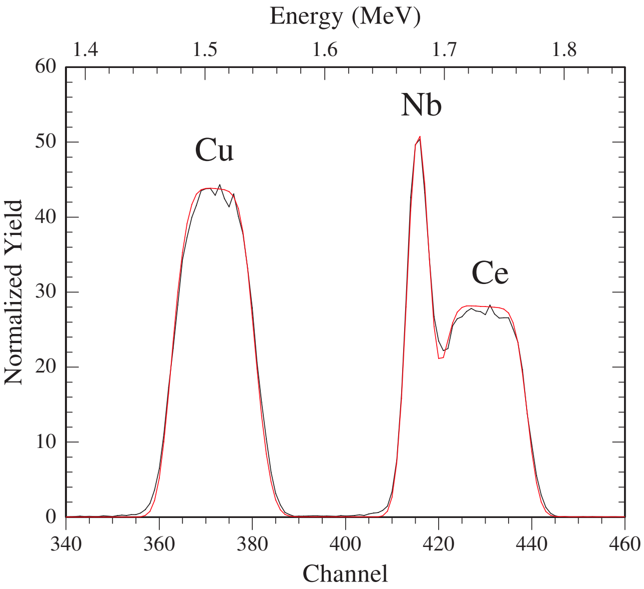

Figure 6.14: RBS measurement using ^{4}He–ions of 2 MeV on a sample Si/Si_3N_4/$CeCu_6$(75 nm)/Nb(15 nm). The different elements are indicated. The thin smooth line is a fit to the measured curve. For the clarity reasons, only part of the spectrum is shown. The signal from the substrate and the Si_3N_4 layer are observed at much lower energies.

Si–substrates with amorphous Si_3N_4 buffer layers of $\sim$ 450 nm thickness. Nb was deposited on top of $CeCu_6$ after cooling the substrate holder with cold nitrogen gas to room temperature. Preparation conditions were chosen as previously determined for the single layer systems. Additionally, composition and thickness of the films were monitored for all samples using RBS. Overall, the RBS analysis shows a very good agreement with the expected stoichiometry for $CeCu_6$. Further, we find no indication for a diffusion, either of Ce or Cu into the substrate or of Nb into $CeCu_6$. As an example, Fig. 6.14 shows the RBS spectrum of the nominal $CeCu_6$(75 nm)/ Nb(15 nm) sample and its perfect agreement with model calculation for $CeCu_6$(75 nm)/ Nb(15 nm), without taking any diffusion into account.

The mean roughness of the $CeCu_6$/Nb system is due to the polycrystalline structure of the $CeCu_6$ higher than for the singe Nb films. For example, the AFM roughness analysis for $CeCu_6$/Nb(30 nm) reveals the average roughness of $\sim$ 1.3 nm (Fig. 6.15 and Fig. 6.16).

The RBS analysis for other samples, and representative AFM surface images for some of the prepared bilayers are presented in the Appendix.

6.4 Results and discussion

In the following section we will present a brief discussion of the physical properties of bilayers $CeCu_6$/Nb. In particular, we compare the data to the results obtained for bi- and trilayers Cu/Nb. From a self–consistent description of our data within the extended Takahashi–Tachiki theory we establish the values for the boundary resistances and diffusion constants in the N and S layers. A full account of this type of analysis is given by Ciuhu [18].

We measured the thermodynamic properties, that is the superconducting transition temperature T_c and upper critical field $H_{c2}^{||}$, of Nb films in the $CeCu_6$/Nb structures. Both quantities are determined from electrical resistivity measurements in a standard 4–point geometry on the structured bilayers with the bridge widths of 200 μm and the voltage contact distance of 1.2 mm. The measurements have been performed in a conventional PPMS system. A sharp superconducting transition observed in these measurements confirms the high quality of the Nb layer in our structures. For

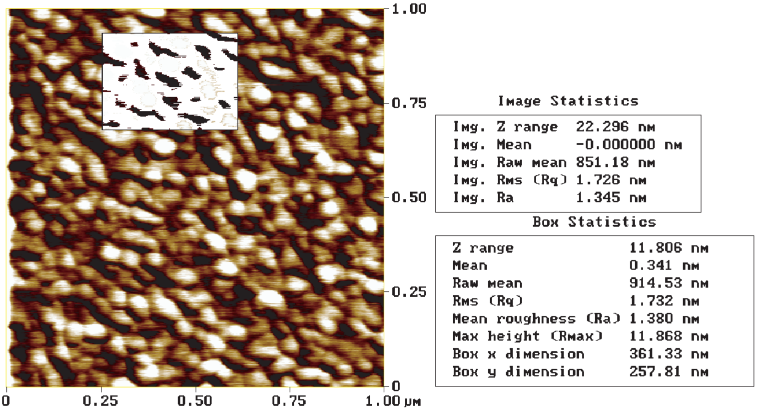

```
          Image Statistics
Img. Z range   22.296 nm
Img. Mean      -0.000000 nm
Img. Raw mean 851.18 nm
Img. Rms (Rq) 1.726 nm
Img. Ra        1.345 nm
              Box Statistics
Z range                 11.806 nm
Mean                    0.341 nm
Raw mean                914.53 nm
Rms (Rq)                1.732 nm
Mean roughness (Ra)     1.380 nm
Max height (Rmax)       11.868 nm
Box x dimension         361.33 nm
Box y dimension         257.81 nm
```

Figure 6.15: AFM image and roughness analysis of a $CeCu_6$(75 nm)/Nb(30 nm) sample. Additionally, statistics of the chosen part of sample surface (marked as a white box) is presented.

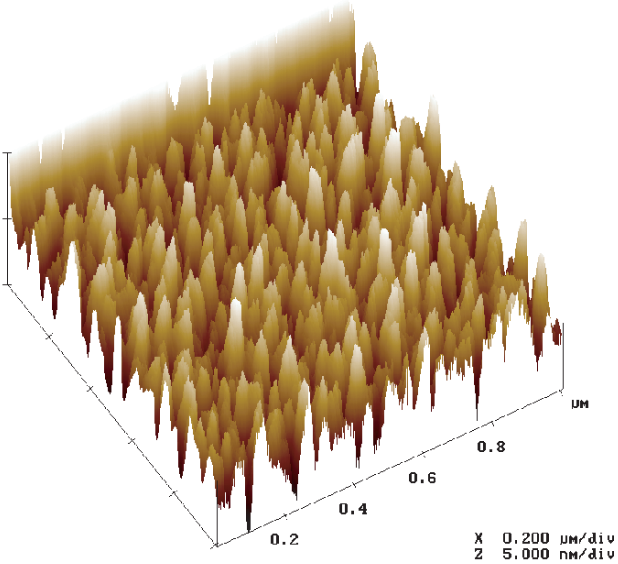

Figure 6.16: The 3D AFM image of $CeCu_6$(75 nm)/Nb(30 nm) sample. Note the scale given at the lower right. X denoted the scale in the sample surface plane, Z is the scale in the direction perpendicular to the surface.

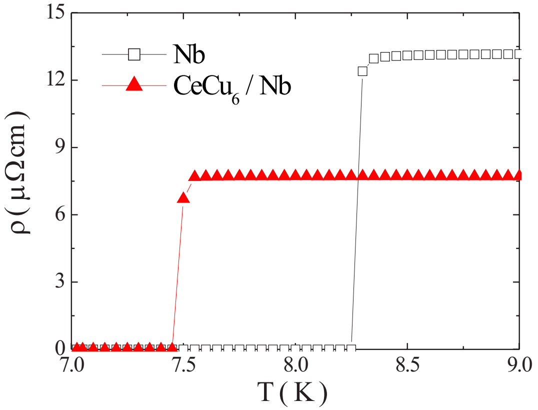

Figure 6.17: The electrical resistivity for a single Nb film and a $CeCu_6$(75 nm)/Nb bilayer, for both samples the Nb film thickness $d_{Nb} = 30$ nm.

comparison, Fig. 6.17 shows the electrical resistivity at the superconducting transition for a single 30 nm thick Nb film and a $CeCu_6$(75 nm)/Nb(30 nm) bilayer. The transition width for both systems is identical, but the T_c for $CeCu_6$(75 nm)/Nb(30 nm) is much smaller. A similar behavior has been observed for all $CeCu_6$(75 nm)/Nb(d_{Nb}) samples, where $d_{Nb} < 50$ nm. As depicted in Fig. 6.18, T_c exhibits a strong suppression upon lowering the Nb layer thickness. For $CeCu_6$/Nb with d_{Nb} of 10 nm no superconducting phase transition has been observed down to 1.8 K. Therefore, the critical thickness d_{cr} for this system, defined as Nb film thickness below which the superconductivity is fully suppressed, is expected to be reached at about 10 nm. Also single Nb layers show a decrease of T_c at small film thickness, as presented in the same figure, which however is much weaker than the suppression observed for $CeCu_6$(75 nm)/Nb(d_{Nb}). Additionally, the T_c reduction is stronger than for superconductor/normal metal layers, for example in Cu/Nb/Cu. Results achieved for trilayers and bilayers can be compared under the assumption that trilayers are equivalent to bilayer systems with the half as thick superconducting layer. This approximation has

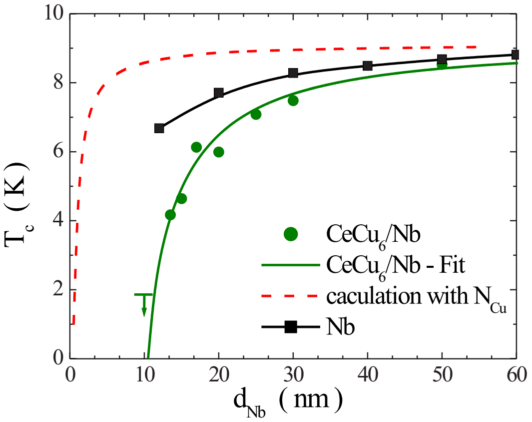

Figure 6.18: Critical temperature (T_c) as a function of Nb thickness d_{Nb} for: bilayers CeCu$_6$(75 nm)/Nb(d_{Nb}), the line is a fit to the data; single Nb films, the line is a guide to the eye; model calculations with $N_{CeCu6} = N_{Cu}$ and D_{Nb} used for a fit of the CeCu$_6$(75 nm)/Nb data - dashed line, details in text.

been found to apply reasonably well for the Cu/Nb system [18, 19]. The critical thickness $d_{cr} < 10$ nm [18–20] for Cu/Nb/Cu corresponds therefore to $d_{cr} < 5$ nm Cu/Nb bilayers. Thus, the superconductivity in CeCu$_6$/Nb bilayers is already suppressed at twice as large Nb thickness. In magnitude this resembles rather in magnitude the values found for Fe/Nb samples [21]. For the trilayers of this ferromagnet/superconductor system the superconductivity is fully suppressed for about 24 nm thick Nb film, which is equivalent to 12 nm for the bilayer structure.

The results directly show that the interface does allow particle exchange, opposite to what might be expected from the huge Fermi velocity mismatch in the system of the order 10^3. Furthermore, the strong suppression of T_c indicates a small coherence length in the heavy fermion compound.

More information about the proximity coupling can be obtained from $H_{c2}^{||}$. In conventional superconductor / normal metal systems such as Nb/Cu, the large (Ginzburg–Landau) coherence length at temperatures T close to

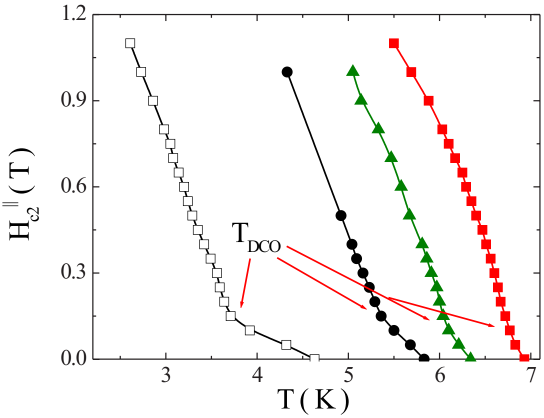

Figure 6.19: Upper parallel critical field as a function of temperature for trilayers Cu(75 nm)/Nb/Cu(75 nm), d_{Nb}; squares – 35 nm, triangle – 30 nm, circle – 25 nm open squares – 20 nm.

Multilayer	d_{Nb} *(nm)*	D_N 10^{-4} m^2/s	D_{Nb} 10^{-4} m^2/s	R_B $10^{-8}\mu\Omega$ cm^2
Cu/Nb	15	240	1.4	177
Cu/Nb/Cu	30	220	2.9	252
$CeCu_6$/Nb	13.5	0.15	1.2	324
$CeCu_6$/Nb	15	0.15	1.4	338
$CeCu_6$/Nb	17	0.19	1.2	350
$CeCu_6$/Nb	25	0.11	1.8	352
$CeCu_6$/Nb	30	0.11	2.0	352
$CeCu_6$/Nb	50	0.11	2.2	324

Table 6.2: The diffusion constants D_N (for $CeCu_6$/Nb or Cu respectively) and the interface resistance R_B values calculated for the different multilayers system; for details see text.

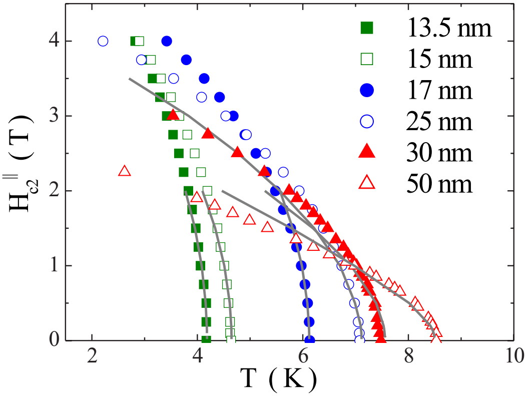

Figure 6.20: Upper parallel critical field as a function of temperature for CeCu$_6$(75 nm)/Nb bilayers, d_{Nb} as indicated. The lines are fit to the data applying the extended Takahashi–Tachiki theory.

T_c leads to a coupled system which can be described as thee–dimensional (3D), meaning that the slope of $H_{c2}^{||}$ is linear in temperature, according to

$$H_{c2}^{||}(T) = \frac{\Phi_0}{2\pi\xi(0)^2} \times (1-t), \tag{6.2}$$

with Φ_0: flux quantum, $\xi(0)$: the Ginzburg–Landau coherence length at $T = 0$, t the reduced temperature ($t = \frac{T}{T_c}$). Upon decreasing T, the system can become decoupled in the sense that the order parameter now only resides in the superconductor. If then the superconducting thickness d_s is smaller than $\xi(T)$, the system will behave as a two–dimensional (2D) superconductor and $H_{c2}^{||}$ is now given by

$$H_{c2}^{||}(T) = \sqrt{12}\Phi_0/(2\pi d_s\xi(0)) \times \sqrt{1-t}. \tag{6.3}$$

The crossover between the 3D and 2D behavior is called a dimensional crossover, and occurs at some temperature T_{DCO}.

This phenomenon can very clearly observed for example in Cu/Nb/Cu trilayers with d_{Nb} = 35, 30, 25, or 20 nm, as shown in Fig. 6.19 [20]. The effect is most pronounced for thin layers of 25 and 20 nm, which become superconducting at much lower T.

In contrast, for the CeCu$_6$/Nb bilayers, the upper parallel critical field $H_{c2}^{||}$ dependence on temperature T is very similar to the behavior observed for two–dimensional superconductors. No dimensional crossover is found at any Nb thickness (Fig. 6.20). The absence of the DCO means that no appreciable amount of superconductivity leaks into the HF metal, which together with the finite transparency implies either appreciable pair breaking by the HF metal, or a very small diffusivity due to the low Fermi velocity v_F.

These central qualitative results have been further analyzed by Ciuhu in the framework of Takahashi–Tachiki theory. First, the $H_{c2}^{||}(T)$ dependence has been calculated, assuming:

- $T_{c,Nb}$, defined as the critical temperature of a single Nb layer, is set to 9.2 K, except for the bilayers of d_{Nb} = 15 nm. In this case, the intrinsic decrease of T_c with the film thickness is taken into account and $T_{c,Nb}$ is set to 8.2 K.

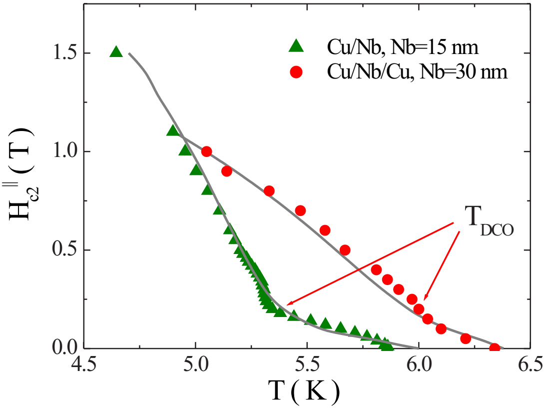

Figure 6.21: Upper parallel critical field as a function of temperature for bilayers Cu(75 nm)/Nb and trilayers Cu(75 nm)/Nb/Cu(75 nm), d_{Nb} as indicated. The lines are fit to the data applying the extended Takahashi–Tachiki theory.

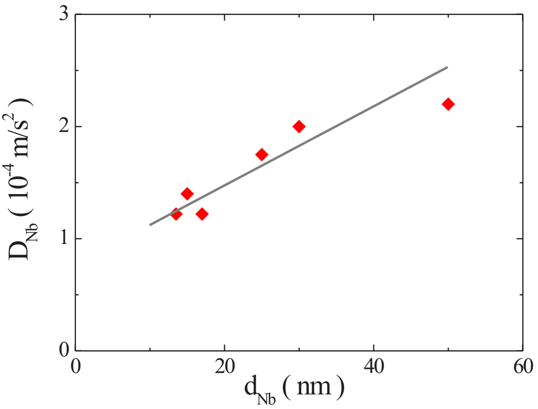

Figure 6.22: The diffusions constant of the Nb layer (D_{Nb}) in dependence of its thickness (d_{Nb}).

- the ratio of density of states $N_{CeCu6}/N_{Nb} = 320$, as derived in Ref. [11].

Free fit parameters of the model are:

- the boundary resistance R_B.
- the diffusion constant of Cu (D_{Cu}) and CeCu$_6$ (D_{CeCu6}).

The best matching with the data fits are presented in Fig. 6.20, with the fit parameters listed in Tab. 6.2.

For comparison, we include the result for normal metal/superconductor multilayers, with Cu/Nb(15 nm) and Cu/Nb(30 nm)/Cu, which were also successfully calculated within the model [18, 20] (Fig. 6.21). The diffusion constant of Nb increases with a growing Nb film thickness and can be described by a linear function (Fig. 6.22). The values of D_{Nb} for the Cu/Nb bi- and trilayers are very similar to those from the CeCu$_6$/Nb systems, which confirm the reliability of our model.

As can be expected for the heavy fermions the values of the diffusion constant of CeCu$_6$ (D_{CeCu6}) are much lower than those of Cu. Yet, such low values of the diffusion constant defined as $D_N = \frac{k_F l_e}{m^*}$ cannot automatically be attributed to the high values of effective mass m^* characteristic for the heavy fermion compound. The low diffusion constants can also result from a low mean free path value, like for example in disordered or very grainy systems. To judge if the heavy effective mass influences the proximity effect in $CeCu_6$/Nb, $T_c(d_{Nb})$ has been calculated with $D_{CeCu6} = 0.1 \times 10^{-4}$ m^2/s, $R_B = 324 \times 10^{-4}$ $\mu\Omega$cm^2 and the appropriate density of states ratio for $CeCu_6$/Nb and Cu/Nb (Fig. 6.18). The fit matches the experimental results only if a high DOS, as it is typical for heavy fermion material, is considered (smooth line). Otherwise, T_c would drop at a much lower d_{Nb}, as depicted by the dashed line. These calculations confirm that a low value of D_{CeCu6} caused by other factor than m^* is not sufficient to fully describe the measurements.

The full description then is that, the low diffusion constant of the non–superconducting material makes the proximity effect less effective and leads to a weaker T_c suppression while, on the other hand, the large number of the available electron states (high DOS) acts as a sink for the Cooper pair and counteracts the low diffusion constant. Both ingredients, a low D_{CeCu6} and high N_{CeCu6} are equivalently necessary to explain the data.

6.5 Summary

In the framework of this project we succeeded in preparation of thin, high quality HF/S bilayers $CeCu_6$/Nb. The chemical composition, depth profile and the surface roughness of the materials prepared by cosputtering were extensively studied by EPMA, RBS and AFM techniques. Additionally, we verified that the electrical resistivity of single layers Nb or $CeCu_6$, deposited under the same conditions as later in the bilayer case, corresponds to the behavior discussed in literature.

In the proximity effect study of the $CeCu_6$(75 nm)/Nb system, with a varying thickness d_{Nb}, we find a strong suppression of T_c for the bilayers with the Nb film thickness below 30 nm, which indicates a finite interface transparency. The critical thickness reaches $\sim$ 10 nm and is similar in magnitude to the values reported for Fe/Nb systems.

Further, in stark contrast to metal/superconductor systems (e.g. Cu/Nb), the dimensional crossover is completely absent and the 2D behavior in $H_{c2}^{||}$ is observed. Analysis of the data within the model based on the Takahash–Tachiki theory shows that the experimental results are explained by considering the low diffusion constant and the large density of states. However, the $T_c(d_{Nb})$ dependence is very similar to the behavior observed for ferromagnet/superconductor multilayers, the study reveals that different mechanisms are responsible for the strong T_c suppression. For the ferromagnet, a large pair breaking potential has to be taken into account to explain the experiments. In contrast, for the heavy fermion material $CeCu_6$, no extra pair breaking mechanism need to be invoked.

6.6 Appendix

In this appendix we show additional AFM images of

1. 32 nm thick Nb thin film,
2. CeCu$_6$(75 nm)/Nb(20 nm) bilayer, and
3. CeCu$_6$(75 nm)/Nb(50 nm) bilayer.

Furthermore, we present RBS spectra of CeCu$_6$(75 nm)/Nb(d_{Nb}) systems with $d_{Nb} = 10$, 20 and 32 nm. All this data confirm the results discussed in the previous chapter.

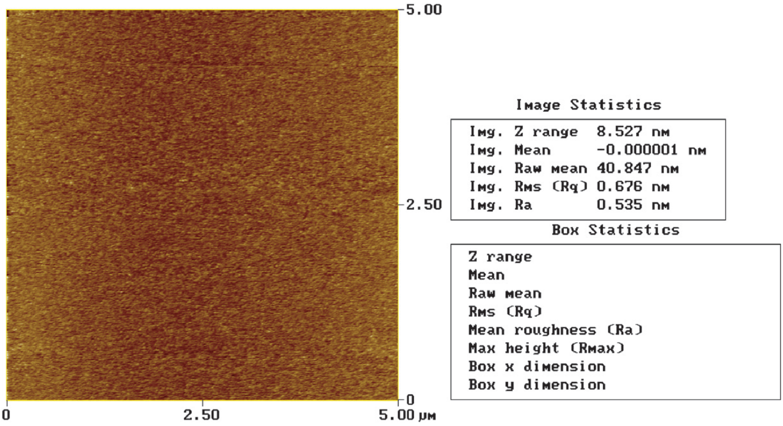

Image Statistics

Img. Z range 8.527 nm
Img. Mean -0.000001 nm
Img. Raw mean 40.847 nm
Img. Rms (Rq) 0.676 nm
Img. Ra 0.535 nm

Box Statistics

Z range
Mean
Raw mean
Rms (Rq)
Mean roughness (Ra)
Max height (Rmax)
Box x dimension
Box y dimension

Figure 6.23: AFM roughness analysis of 32 nm thick Nb sample, with the plane surface image and AFM image statistics.

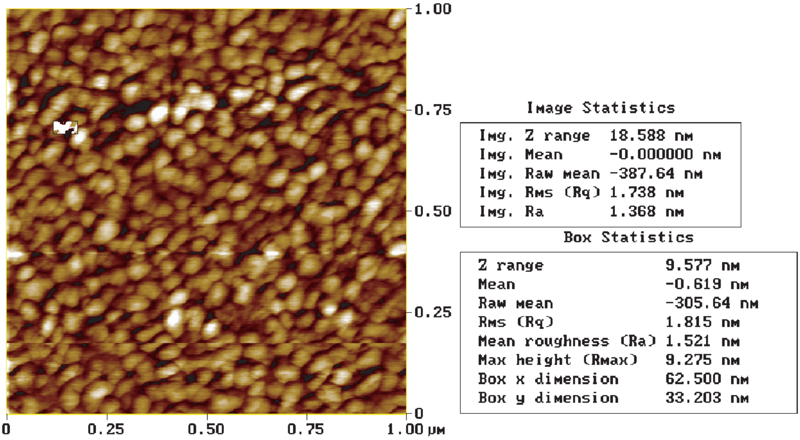

```
          Image Statistics
  Img. Z range    18.588 nm
  Img. Mean       -0.000000 nm
  Img. Raw mean -387.64 nm
  Img. Rms (Rq)  1.738 nm
  Img. Ra         1.368 nm
              Box Statistics
  Z range                  9.577 nm
  Mean                     -0.619 nm
  Raw mean                 -305.64 nm
  Rms (Rq)                 1.815 nm
  Mean roughness (Ra)  1.521 nm
  Max height (Rmax)     9.275 nm
  Box x dimension        62.500 nm
  Box y dimension        33.203 nm
```

Figure 6.24: AFM image and roughness analysis of CeCu$_6$(75 nm)/Nb(20 nm). Additionally, statistics of the chosen small part of sample surface (marked as a white box) is shown.

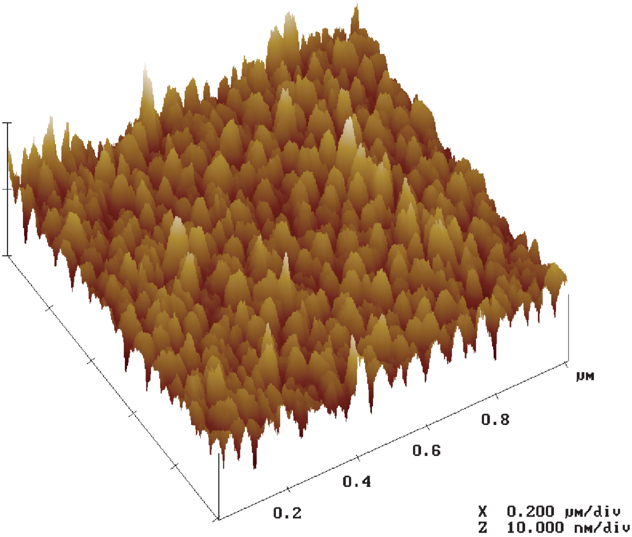

Figure 6.25: The 3D AFM image of $CeCu_6$(75 nm)/Nb(20 nm). Note the scale given at the lower right. X denoted the scale in the sample surface plane, Z is the scale in the direction perpendicular to the surface.

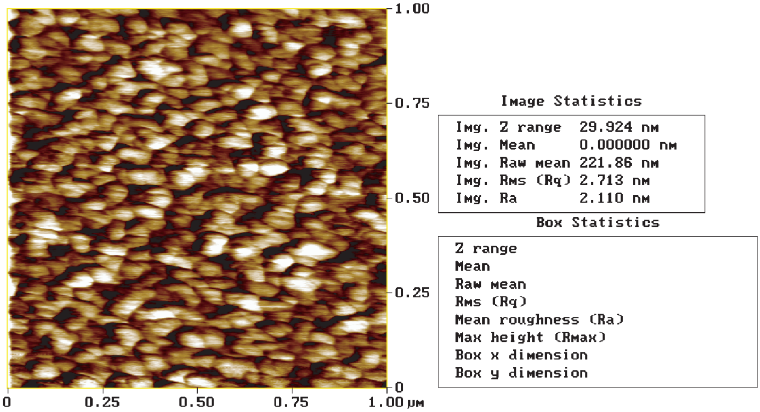

```
Image Statistics
Img. Z range   29.924 nm
Img. Mean      0.000000 nm
Img. Raw mean 221.86 nm
Img. Rms (Rq) 2.713 nm
Img. Ra        2.110 nm

Box Statistics
Z range
Mean
Raw mean
Rms (Rq)
Mean roughness (Ra)
Max height (Rmax)
Box x dimension
Box y dimension
```

Figure 6.26: AFM image and roughness analysis of $CeCu_6$(75 nm)/Nb(50 nm).

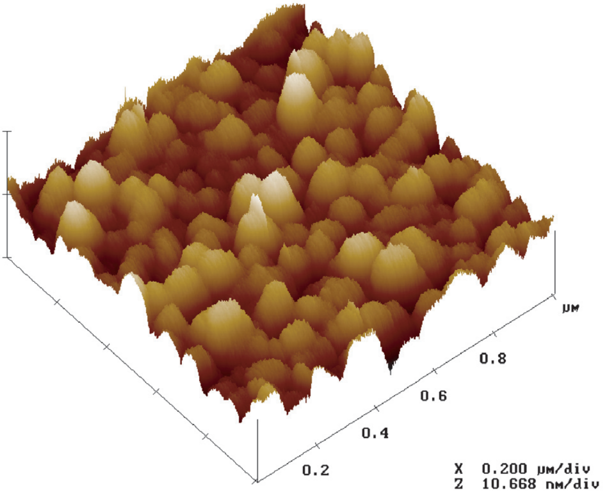

Figure 6.27: The 3D AFM image of CeCu$_6$(75 nm)/Nb(50 nm). Note the scale given at the lower right. X denoted the scale in the sample surface plane, Z is the scale in the direction perpendicular to the surface.

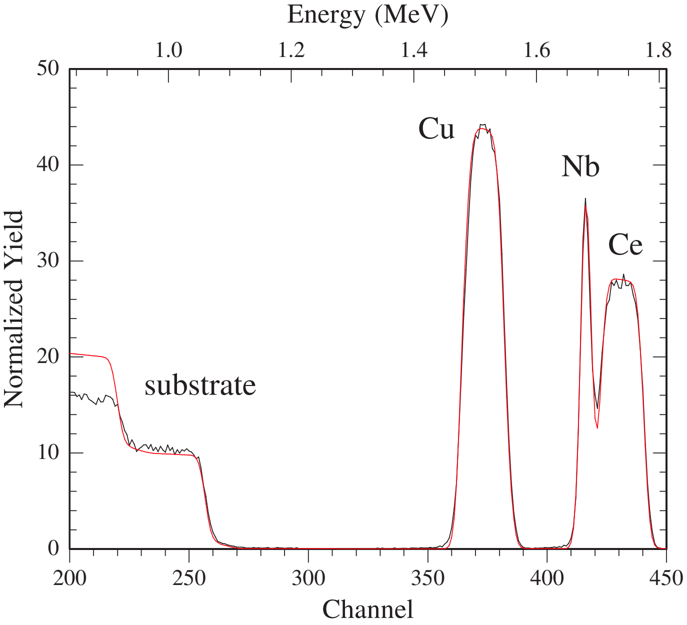

Figure 6.28: RBS measurement using ^{4}He-ions of 2 MeV on a sample Si/Si_3N_4/$CeCu_6$(75 nm)/Nb(10 nm). The different elements are indicated. The thin smooth line is a fit to the measured curve. For the clarity reasons, only the part of the of the signal from the substrate and the Si_3N_4 layer is shown. The mismatch between the RBS substrate signal and the calculations results from the channelling effect.

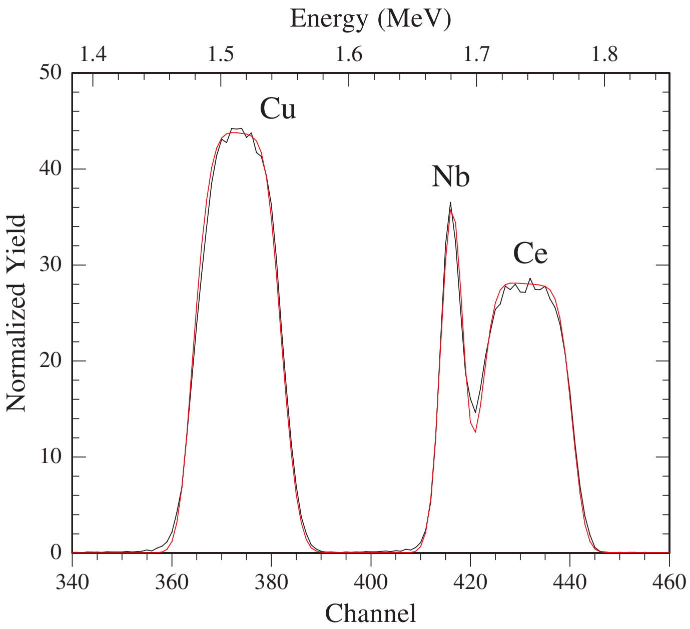

Figure 6.29: RBS measurement using ^{4}He-ions of 2 MeV on a sample Si/Si_3N_4/$CeCu_6$(75 nm)/Nb(10 nm). The different elements are indicated. The thin smooth line is a fit to the measured curve. For the clarity reasons, only the part of the spectrum is shown. The signal from the substrate are observed at much lower energies.

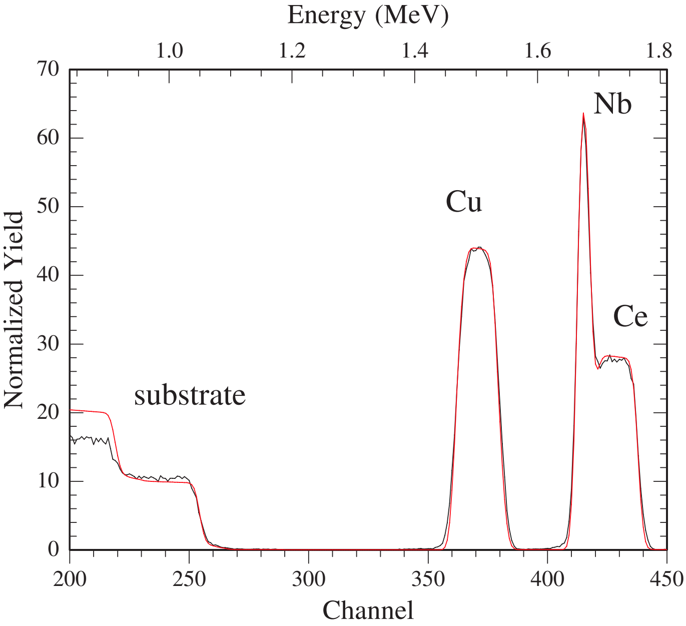

Figure 6.30: RBS measurement using ^{4}He-ions of 2 MeV on a sample Si/Si_3N_4/$CeCu_6$(75 nm)/Nb(20 nm). The different elements are indicated. The thin smooth line is a fit to the measured curve. For the clarity reasons, only the part of the of the signal from the substrate and the Si_3N_4 layer is shown. The mismatch between the RBS substrate signal and the calculations results from the channelling effect.

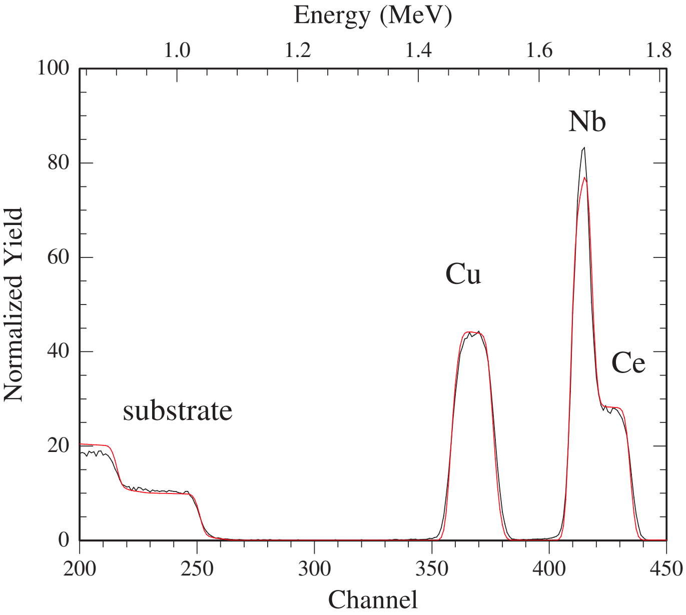

Figure 6.31: RBS measurement using ^{4}He-ions of 2 MeV on a sample Si/Si_3N_4 /$CeCu_6$(75 nm)/Nb(32 nm). The different elements are indicated. The thin smooth line is a fit to the measured curve. For the clarity reasons, only the part of the of the signal from the substrate and the Si_3N_4 layer is shown. The mismatch between the RBS substrate signal and the calculations results from the channelling effect.

Bibliography

[1] V.V. Ryazanov, V.A. Oboznov, A.Yu. Rusanov, A.V. Veretennikov, A.A. Golubov, and J. Aarts, Phys. Rev. Lett. **86**, 2427 (2001).

[2] D. Groten, Ph.D. Thesis, (1999), unpublished.

[3] D. Groten, G.J.C. van Baarle, R.W.A. Hendrikx, J. Aarts, G.J. Nieuwenhuys, and J.A. Mydosh, Physica B **259-261**, 31 (1999).

[4] D. Groten, G.J.C. van Baarle, J. Aarts, G.J. Nieuwenhuys, and J.A. Mydosh, Phys. Rev. B **64**, 144425 (2001).

[5] G.R. Stewart, Z. Fisk, and M.S. Wire, Phys. Rev. B **30**, 482 (1984).

[6] A. Amato, D. Jaccard, J. Flouquet, F. Lapierre, J.L. Tholence, R.A. Fisher, S.E. Lacy, J.A. Olsen, and N.E. Phillips, J. Low Temp. Phys. **68**, 371 (1987).

[7] A. Amato, D. Jaccard, E. Walker and J. Flouquet, Solid State Commun. **55**, 1131 (1985).

[8] H. v. Löhneysen, J. Phys. Condens. Matter **8**, 9689 (1996).

[9] A. Sumiyama, Y. Oda, H. Nagano, Y. Onuki, and T. Komatsubara, J. Phys. Soc. Jpn. **54**, 877 (1985).

[10] A. Sumiyama, Y. Oda, H. Nagano, Y. Onuki, K. Shibutani, and T. Komatsubara, J. Phys. Soc. Jpn. **55**, 1294 (1986).

[11] A. Otop, G.R. Boogaard, R.W.A. Hendrikx, M.B.S. Hesselberth, C. Ciuhu, A. Lodder, and J. Aarts, Euro. Phys. Lett. **64**, 91 (2003).

[12] www.research.philips.com/ technologies/ misc/ matanalysis/ publications.html

[13] www.amolf.nl

[14] O.H. Seeck, in *Nanoelectronics and Information Technology*, edited by R. Waser,(WILEY-VCH, Weinheim 2003), p. 273.

[15] S.I. Park, and T.H. Geballe, Physica B **135**, 108 (1985).

[16] J. Graybeal, and M. Beasley, Phys. Rev. B **29**, 14167 (1984).

[17] H. Sellier, private communication (2001).

[18] C. Ciuhu, Ph.D. Thesis, (2003), unpublished.

[19] G.R Boogaard, Diploma Thesis, (2001), unpublished.

[20] A. Otop, and J. Aarts, (2002), unpublished.

[21] J.M.E. Geers, M.B.S. Hesselberth, J. Aarts, and A.A. Golubov, Phys. Rev. B **64**, 094506 (2001).

Curriculum Vitae

Anna Otop born on the 16 September 1976 in Wrocław (Poland)

1982–1995	primary and secondary school in Wrocław
May 25th 1995	Abitur
1995–2000	Study of Physics at the Wrocław University of Technology and at the Technical University of Braunschweig
October 26th 2000	M.Sc. in Physics, Master thesis: *Set–up of a LEED/Auger–Spectrometer and Growth of Thin Ferromagnetic Films in a UHV Conversion Electron Mössbauer Spectrometer* at the Institute of Metal Physics and Nuclear Solid State Physics (Technical University of Braunschweig) Supervisor: Prof. Dr. F.J. Litterst
2001–2005	Ph.D. student at the Institute for Physics of Condensed Matter Technical University of Braunschweig Supervisor: Jun.-Prof. Dr. S. Süllow
2001–2002	Research stay at the Kamerlingh Onnes Laboratory Leiden University, The Netherlands, in the group of Prof. Dr. J. Aarts

WEITERE VERÖFFENTLICHUNGEN

PUBLIKATIONEN:

- A. Otop, I. Maksimov, F.J. Litterst, J.A. Mydosh, and S. Süllow, *Hall effect in* $URh_2Ge_{2-x}Sn_x$, J. Magn. Magn. Mat. **272-276**, E1019 (2004).
- S. Süllow, I. Maksimov, A. Otop, F.J. Litterst, A. Perucchi, L. Degiorgi, and J.A. Mydosh, *Metallic ground state and glassy transport in single crystalline* URh_2Ge_2*: Enhancement of disorder effects in a strongly correlated electron system*, Phys. Rev. Lett. **93**, 266602 (2004).
- P. Giudicelli, U. Killer, J.W. Taylor, S.J. Levett, A. Otop, E.-W. Scheidt, A. Stunault, and N. Bernhoeft, *Disorder tuning of non-Fermi-liquid behaviour in* UCu_4Pd, Europhys. Lett. **69**, 577 (2005).
- A. Otop, I. Maksimov, E.-W. Scheidt, J.A. Mydosh, and S. Süllow, *High temperature resistivity of* URh_2Ge_2, Physica B, in print (2006).

TAGUNGSBEITRÄGE:

- A. Otop, I. Maksimov, F.J. Litterst, J.A. Mydosh, and S. Süllow, *Hall effect in* $URh_2Ge_{2-x}Sn_x$, International Conference on Magnetism (ICM 2003), Rom, Italy, July 27 – August 1, 2003.

THANKS

Looking back on last four years, I would like to express my grateful thanks to the following people:

- my supervisor, Prof. Stefan Süllow, for his support during my Ph.D. study and for long scientific discussions and scientific training,
- Prof. Jan Aarts for providing a motivating work atmosphere and an introduction to the fascinating topic of proximity effects,
- Prof. Jochen Litterst and Dr. Ernst–Wilhelm Scheidt for the helpful discussions,
- Dr. Gerard Nieuwenhuys for the scientific discussions and calculations on UPt_2Si_2 and for being the contact person during the first weeks of my stay in Leiden,
- Marcel Hesselberth for help with the initial steps in thin film techniques – it was great fun, for interesting talks over coffee and to experience his very refreshing view of the world,
- Dr. Hanns–Henning Klauss for the μSR measurements and all those posters we print out from his account,
- Anja Wolter for sharing an office with me for the last three years, as well as the ups and downs of Ph.D. life – it was never boring!
- Federica Galli, whom I have come to know as a very humorous and positive person, for a really great time at the Kamerlingh Onnes Laboratory,
- my colleges from the Kamerlingh Onnes Laboratory (Alexei, Achille, Gerrit, Gert-Jan, Nobu, Sasha, Yang), and especially to R.W.A. Hendrix, T.J. Gortenmulder, for the experimental support and very friendly work atmosphere,

- my Braunschweig colleges at the Institute for Physics of Condensed Matter: Anika, Christopher, Hannes, Igor, Jan, Marc, Matthias and Sascha nice talks over the lunch breaks,
- Ole and Hanno for their proofreading efforts,
- Heiko Ahlerst and Joachim Lüdke from PTB for giving me sufficient measurement time at the SQUID magnetometer,
- my English teacher, Ryan Dorr, for a long and interesting discussion about film and politics,
- Robert and Arno for technical support, and for being very motivating running partners,
- Renia, Jan and Thomas for our fascinating outdoor adventures,
- my parents for interest on my research work and their support.